



Master Thesis



Numerical simulation of debris flows with the 2D - SPH depth integrated model

Submitted by

THOMAS BLANC

In

The Institute for Mountain Risk Engineering

University of Natural Resources and Applied Life Sciences - Vienna

A Thesis submitted in partial fulfillment of the requirements for
the degree of Master of Science

Supervisors:

Hübl Johannes, Ao.Univ.Prof. Dipl.-Ing. Dr.nat.techn.

Pastor Manuel, Univ.Prof. Dipl.-Ing.

Vienna, 2008

In cooperation with:

**Centro de Estudios y Experimentación
de Obras Públicas**

Section:

Centro de Estudios de Técnicas Aplicadas

Department:

Ingeniera computacional run by M. Pastor

www.cedex.es



Carried out at:

**Centro de Estudios y Experimentación
de Obras Públicas**

Section:

Centro de Estudios de Técnicas Aplicadas

Department:

Ingeniera computacional run by M. Pastor

www.cedex.es



ABSTRACT

Debris flow analysis is important to assess the risk and to delimitate vulnerable areas where mitigation measures are required. Numerical model is the most accurate and efficient tool for debris flow analysis. The SPH depth integrated model is one of the available models. It has been created by Pastor in 2005. The SPH depth integrated model is a 2D model able to predict runout distance, flow velocity, deposition pattern and final volume of debris flows. It is based on a mathematical model, on rheological models and on a numerical model. The basis of the mathematical model is a coupled depth integrated model coming from a velocity-pressure version of Biot-Zienkiewicz equations. The rheological models correspond to constitutive equations. In this work, the frictional and the Voellmy model has been used to simulate debris flows. The numerical model used is the SPH (Smooth Particles Hydrodynamics) methods. The SPH depth integrated model has been validated using analytical and back analysis. Actually not valuable database for input parameters are available. In this study, three case studies have demonstrated that the SPH depth integrated model is useful for debris flow risk analysis. A work on erosion law has been proposed in order to improve the model. After this thesis, the model gives to the user the opportunity to choose between the Hungr and the Egashira erosion law to model erosion processes. The study has shown that the Egashira erosion law is more efficient to predict some characteristics of debris flows, as flow velocity and deposition pattern.

RESUME

L'analyse de laves torrentielles est importante afin d'évaluer le risque dans certaines zones et permet de savoir où des mesures de protections sont nécessaires. Les modèles numériques sont les outils les plus précis et les plus efficaces pour analyser les écoulements de laves torrentielles. Le modèle « SPH depth integrated » est l'un des modèles actuellement disponibles. Il a été créé par Manuel Pastor en 2005. Ce modèle en deux dimensions est capable de prédire la distance, la vitesse de l'écoulement et aussi l'emplacement et le volume final des dépôts. Ce modèle est basé sur un modèle mathématique, des modèles rhéologiques and sur un modèle numérique. La base du modèle mathématique est le modèle intégré en profondeur venant d'une version vitesse-pression des équations de Biot-Zienkiewicz. Dans cette étude, les modèles rhéologiques (équations constitutives) utilisés pour simuler les laves torrentielles sont le modèle frictionnel et le modèle de Voellmy. Enfin la méthode SPH (Smooth Particles Hydrodynamics) constitue le modèle numérique. Le modèle « SPH depth integrated » a été validé en simulant des problèmes ayant une solution analytique et en simulant des cas réels d'écoulement de lave torrentielle. Cependant, actuellement, aucune base de donnée concernant les paramètres d'entrée est disponible. Dans la première partie de l'étude, trois études de cas réels ont montré que le modèle écrit par Pastor est utile pour analyser le risque d'écoulement de laves torrentielles. La deuxième partie de l'étude se consacre aux phénomènes d'érosion et a permis d'intégrer au modèle la loi d'érosion proposée par Egashira. L'utilisateur du modèle peut alors choisir de simuler l'érosion soit en utilisant la loi d'Egashira soit celle d'Hungr. Enfin cette étude a montré que la loi d'Egashira prédit de manière plus efficace la vitesse d'écoulement et la disposition des dépôts.

ACKNOWLEDGEMENTS

First I have to thank Manuel Pastor for having organized and led my work in the CEDEX. Thanks also for letting me use the SPH depth integrated model. I am very happy to have had the opportunity to work with him. His advices were useful and his explanations help me to get ahead with my thesis.

I would like to thank also my supervisors in BOKU, Prof. Hübl and Prof. Schneider, who were a support although being in Vienna.

Thanks also to my supervisor in AgroParisTech-ENGREF, who follows the development of my thesis. He counseled me about the structure of the thesis.

I would like to specially thank Roland Kaitna, who was present always to answer to my several questions. He helped me to solve my administration problems. He gave directions to my work before I started working in Spain. The discussions, that we have had, have strongly improved my thesis.

I thank also to Dieter Rickenmann for having provided articles when I asked him.

Finally thanks to all the research team of the CEDEX (Bouchra, Cristina, Ester, Maribel, Mila, Valentina, Diego, Jose and Pablo) for helping me when I need it and also for the good atmosphere at the work place.

TABLE OF CONTENTS

Abstract	i
Acknowledgements	ii
Table of contents	iii
List of appendixes	vi
List of figures	vii
List of tables	x
List of symbols	xi
1 Introduction	1
1.1 Introduction	1
1.2 Objectives and structure of the thesis	1
1.3 Debris flow: description of the processes	2
1.3.1 Definition of the term “debris flow”	2
1.3.2 Initiation of the debris flow	3
1.3.3 Propagation of the debris flow	4
1.3.4 Deposition on the debris fan	9
1.3.5 Parameters describing debris flows	10
1.4 Discussion	11
2 Methodology: the SPH depth integrated model	12
2.1 Introduction	12
2.2 Mathematical model	12
2.2.1 Introduction	12
2.2.2 Physical properties of geomaterials	12
2.2.3 General model	15
2.2.4 The V-p _w model	16
2.2.5 Propagation-consolidation approximation	17
2.2.6 Depth integrated model	18

2.3	Rheological models of a fluidized material	20
2.3.1	Introduction	20
2.3.2	The frictional model and the Voellmy model	21
2.4	Numerical model: SPH approximation	22
2.4.1	Introduction	22
2.4.2	Integral approximation of functions and derivatives: General aspects	23
2.4.3	SPH discretization of integral approximation of functions and derivatives	23
2.4.4	Numerical solution of an ODE using Runge Kutta 4 th (RK4) order method	24
2.5	Erosion law.....	24
2.5.1	Introduction	24
2.5.2	Description of the Hungr erosion law (Hungr 1995)	24
2.5.3	Description of the Egashira erosion law (Egashira1993).....	25
2.5.4	Adaptation of the Egashira erosion law to the SPH depth integrated model	27
2.6	SPH code	28
2.6.1	Introduction	28
2.6.2	Overview of the SPH code structure	28
2.6.3	Implementation of the Egashira erosion law	30
2.7	Discussion of the parameters used in the model.....	31
3	Results –Part 1: Calibration of the model	34
3.1	Introduction to the calibration.....	34
3.2	The Sham Tseng San Tsuen Debris Flow, Hong Kong.....	34
3.2.1	Description of the event	34
3.2.2	Parameters of the calibration.....	36
3.2.3	Results	37
3.3	The 1990 Tsing Shan Debris Flow, Hong Kong.....	39
3.3.1	Description of the event	39
3.3.2	Parameter of the calibration	41
3.3.3	Results	41

3.4	The 2000 Tsing Shan Debris Flow, Hong Kong.....	44
3.4.1	Description of the event	44
3.4.2	Parameters of the calibration.....	45
3.4.3	Results and discussion.....	46
3.5	Conclusion.....	48
4	Results – Part 2: Comparison between two erosion laws.....	49
4.1	Application of the Egashira law to the case studies	49
4.1.1	The 1990 Tsing Shan Debris Flow, Hong Kong.....	49
4.1.2	The 2000 Tsing Shan Debris Flow, Hong Kong.....	51
4.2	Comparison of results after Hungr and Egashira law.....	53
4.2.1	The 1990 Tsing Shan debris flow	53
4.2.2	The 2000 Tsing Shan debris flow	55
4.3	Conclusion.....	58
5	Discussions	62
5.1	Discussion on the results of part 1	62
5.2	Discussion on the results of part 2	63
6	Conclusion	65
References	66
Contacts	69
Appendixes	70

LIST OF APPENDIXES

Appendix 1. Composition of a debris flow (ternary phase diagram).....	ii
Appendix 2. Slope angles measures at sites of debris flow initiation from landslides in localities where numerous debris flows resulted from one or more hydrologic event	iii
Appendix 3. Critical rainfall to initiate a debris flow.....	iv
Appendix 4. Schematic longitudinal profile of a debris flow	v
Appendix 5. Landslide velocity scale after Cruden and Varnes (1996).....	vi
Appendix 6. Details on the “propagation – consolidation” approximations done in the 2D SPH depth integrated model	vii
Appendix 7. Details on the depth integration estimations done in the 2D SPH depth integrated model	x
Appendix 8. Details on the integral approximation of functions and derivatives in the SPH method	xiv
Appendix 9. Details on the SPH discretization of integral approximation of functions and derivatives	xix
Appendix 10. Description of the Runge Kutta 4 th (RK4)	xxviii

LIST OF FIGURES

Figure 1.	Debris flow of Val Varuna (1987)	3
Figure 2.	Illustration of the initiation of debris flow	3
Figure 3.	Natural dam composed of organic and soil debris	4
Figure 4.	Sketch of a debris flow surge.....	5
Figure 5.	Channel cross section during the passage of a debris flow.....	5
Figure 6.	Sketch of superelevation	6
Figure 7.	Schematic cross section defining H and L for debris flow paths	7
Figure 8.	Debris flow deposit in lobate shape	10
Figure 9.	Sketch of representative sample of soil	13
Figure 10.	Representation of the different type of soils	14
Figure 11.	Reference system and notation used in the analysis.....	19
Figure 12.	SPH mesh to model a debris flow in Hong Kong	23
Figure 13.	Nodes and numerical integration in a SPH mesh.....	24
Figure 14.	Definition sketch of the erosion rate.....	26
Figure 15.	Overview of the SPH code structure.....	29
Figure 16.	Parameters of the subroutine “Erosion_SW”	30
Figure 17.	Structure of the subroutine “Erosion_SW”	31
Figure 18.	General view of the Sham Tseng San Tsuen debris flow.....	35
Figure 19.	Topography of the terrain	35
Figure 20.	Oblique Aerial View of the Landslide Sites (Photograph Taken on 26 August 1999)	35
Figure 21.	Sham Tseng San Tsuen debris flow: Model predictions versus Field observations	37
Figure 22.	Sham Tseng San Tsuen debris flow: Model predictions - evolution of the debris flow.....	38
Figure 23.	Sham Tseng San Tsuen debris flow: Debris deposition after the event	39
Figure 24.	General view of the 1990 Tsing Shan debris flow	39
Figure 25.	The 1990 Tsing Shan debris flow: Erosion and deposition processes	41
Figure 26.	The 1990 Tsing Shan debris flow: Model predictions versus Field observations	41
Figure 27.	The 1990 Tsing Shan debris flow: Model predictions - evolution of the debris flow	42

Figure 28.	The 1990 Tsing Shan debris flow: Deposition after Model predictions versus real deposition.....	43
Figure 29.	The 2000 Tsing Shan debris flow: Genera view	44
Figure 30.	The 2000 Tsing Shan debris flow: Bifurcation of the flow in two drainage lines	45
Figure 31.	The 2000 Tsing Shan debris flow: Model predictions versus Field observations	46
Figure 32.	The 2000 Tsing Shan debris flow: Model predictions - evolution of the debris flow.....	47
Figure 33.	The 1990 Tsing Shan debris flow: Model predictions versus Field observations	49
Figure 34.	The 1990 Tsing Shan debris flow: Model predictions – evolution of the event.....	50
Figure 35.	The 1990 Tsing Shan debris flow: Deposition after Model predictions versus real deposition.....	51
Figure 36.	The 2000 Tsing Shan debris flow: Model predictions versus field observations	51
Figure 37.	The 2000 Tsing Shan debris flow Model predictions - evolution of the event.....	52
Figure 38.	Comparison of the linear erosion rate obtained during the 1990 Tsing Shan debris flow and those calculated by the simulations.....	54
Figure 39.	Comparison of the volume increase rate of the 1990 Tsing Shan debris flow and those calculated by the simulations	55
Figure 40.	Comparison of the linear erosion rate obtained during the 2000 Tsing Shan debris flow (upper part) and those calculated by the simulations	56
Figure 41.	Comparison of the volume increase rate of the 2000 Tsing Shan debris flow (northern branch) and those calculated by the simulations	57
Figure 42.	Comparison of the volume increase rate of the 2000 Tsing Shan debris flow (southern branch) and those calculated by the simulations	57
Figure 43.	Comparison of the linear erosion rate obtained during the 2000 Tsing Shan debris flow (southern part) and those calculated by the simulations	58
Figure 44.	Comparison of the volume increase rate of the 1990 Tsing Shan debris flow and those calculated by the simulations (with the proposed erosion law)	59

Figure 45.	Comparison of the volume increase rate of the 2000 Tsing Shan debris flow (northern branch) and those calculated by the simulations (with the proposed erosion law)	60
Figure 46.	Comparison of the volume increase rate of the 2000 Tsing Shan debris flow (southern branch) and those calculated by the simulations (with the proposed erosion law)	60
Figure 47.	Parameter used by McDougall in various case studies	63

LIST OF TABLES

Table 1.	Comparison of the parameters describing debris flow processes from the SPH model and those from the literature	32
Table 2.	Flow velocities predicted by the simulation for the 2000 Tsing Shan debris flow	47
Table 3.	Flow velocities predicted by the simulation for the 2000 Tsing Shan debris flow	53

LIST OF SYMBOLS

a_0	empirical factor (Rickenmann 2003)	[–]
A_e	erosion yield per unit channel length	$[m^3 / m]$
b	term for the external forces	$[m / s^{-2}]$
c	sediment concentration of the debris flow by volume (solid volume fraction)	[%]
c_f	fluid solid fraction	[%]
c'	compressibility of the material	$[Pa^{-1}]$
c_*	sediment concentration by volume of bed sediment	[%]
C_v	consolidation coefficient	$[m^2 / s]$
D	rate of deformation tensor	[–]
D^*	rainfall duration	[hours]
$\frac{D}{Dt}$	material derivative operator	[–]
e_r	erosion rate	$[m / s]$
E_l	linear erosion rate	$[m^3 / m]$
E_p	total potential energy	$[kg \times m^2 / s^{-2}]$
E_s	growth rate	$[m^{-1}]$
g	magnitude of the gravitational acceleration	$[m / s^{-2}]$
h	flow depth	[m]
H	vertical elevation of the debris flow source	[m]
I	average rainfall intensity	[mm]
\mathbf{I}	tensor identity of second order	[–]
k	hydraulic permeability	$[m / s]$
k_α	permeability of the phase α	$[m^2]$
k_1	correction coefficient for calculating the flow velocity	[–]
K	empirical factor integrated in the Egashira erosion law	[–]
K_T	volumetric rigidity of the solid skeleton	[Pa]
M	mass of the debris flow	$[m^3]$
n	porosity	[–]
N	number of grain above the layer of interest (quasi-static stress)	[–]
P	pressure of the impact forces	[–]
\bar{p}	averaged pressure of the fluid phases	[Pa]
p_α	pressure of the fluid phase α	[Pa]
p_w	pore pressure	[Pa]
r_c	radius of curvature of the bend	[m]

R	dimensionless net resistance coefficient	$[-]$
s	strength of Mohr-Coulomb	$[N / m^2]$
s_α	deviatoric component of the Cauchy stress tensor	$[N / m^2]$
S	channel gradient	$[-]$
S_α	degree of saturation for the phase α	$[-]$
v'	flow velocity head	$[m / s]$
V	mean velocity of the flow	$[m / s]$
\bar{v}_i	depth averaged velocity	$[m / s]$
v_0	velocity field corresponding to propagation	$[m / s]$
v_1	velocity field corresponding to consolidation	$[m / s]$
v^α	velocity of the fluid phase α	$[m / s]$
v^s	velocity of the solid phase s	$[m / s]$
V_a	volume occupied by air	$[m^3]$
V_{dep}	volume of the deposited debris	$[m^3]$
V_{ent}	volume of the entrained debris	$[m^3]$
V_{ini}	volume of the initial failures	$[m^3]$
V_m	mixture volume which enters the reach from upstream	$[m^3]$
V_s	volume of the solid phase	$[m^3]$
V_t	volume total of the mixture	$[m^3]$
V_{tot}	total volume of the flow	$[m^3]$
V_v	volume of voids	$[m^3]$
V_w	volume occupied by water	$[m^3]$
x_1 and x_2	axes on a horizontal plane	$[-]$
x_3	axes perpendicular to the plane formed by x_1 and x_2	$[-]$
w	width	$[m]$
W	work	$[J]$
Z	elevation	$[m]$
α	velocity head coefficient	$[-]$
β	channel slope	$[-]$
β_1	exponent of the slope channel	$[-]$
γ	unit weight of the debris flow material	$[kg / m^3]$
$\dot{\gamma}$	shear rate	$[s^{-1}]$
γ_w	specific weight of the fluid	$[kg / m^3]$
δ	mean diameter	$[m]$
Δh	elevation difference between the inside and outside of the bend	$[m]$
Δ_l	relative travelled distance	$[\%]$

ΔV	volume increase rate	[%]
θ	slope	[°]
θ_e	equilibrium bed slope	[°]
ρ_α	density of the fluid of the phase α	[kg / m ³]
$\rho^{(\alpha)}$	density of the fluid phase α	[kg / m ³]
ρ_s	density of the solid particle of the solid phase	[kg / m ³]
$\rho^{(s)}$	density of the solid phase s	[kg / m ³]
ρ'_d	submerged density of particle	[kg / m ³]
ρ_m	density of the mixture entering	[kg / m ³]
ρ_w	water density	[kg / m ³]
ζ	turbulence coefficient	[m / s ²]
σ	total Cauchy stress	[N / m ²]
$\sigma^{(\alpha)}$	partial stress of the pore fluid phases	[N / m ²]
$\sigma^{(s)}$	partial stress of the solid phase	[N / m ²]
τ	shear stress	[N / m ²]
τ_B	stress at the bottom	[N / m ²]
ϕ	internal friction angle of the bed	[°]
ϕ_b	friction angle	[°]
μ	viscosity	[Pa × s]
ω^α	relative velocity of Darcy	[m / s]

1 INTRODUCTION

1.1 Introduction

Debris flows travel at extremely rapid velocity and can impact large areas, often far from their source. In mountain valley, generally settled areas are situated close to torrents or rivers because these areas are more favorable to urban development. Therefore these areas are located where sediments and debris are deposited from the channel. In order to protect infrastructures of these areas, mitigation measures can be taken along the entire flow path. However risk is still present and must be evaluated. In case of debris flow, the extent of the potential area and the intensity of the impact have to be known to assess the risk. The prediction of the debris flow propagation (deposition area and impact within it) is called runout analysis. This analysis can provide relevant information for land use planning.

Effective methods of performing debris flow runout analysis are needed. These methods must be quantitative, and as accurate, objective and accessible as possible. Quantification gives to the user results which are easy to communicate and easy understandable by local populations. Accuracy is important because underestimation of risk leads to endanger people and overestimation of risk involves not necessary expending. Objectivity produces results which are repeatable and defensible. Finally accessibility is required otherwise the method cannot be used by practitioners. The methods should be as easy as possible. Modeling of debris flow propagation appears to be an appropriate method satisfying these criteria. Indeed debris flow models give easily flow velocity, flow depth and debris volume as an output. Moreover models require few adjustable input parameters to calculate these magnitudes. The SPH depth integrated model has been written by Pastor (2005) in order to propose an accurate and accessible method. This model is a depth integrated version of several rheological models, providing all necessary items to be implemented in a numerical model. The SPH depth integrated model is a calibration-based model, which means that the appropriate rheological parameters must be constrained by back analysis of previous real debris flows.

However, until now, the SPH depth integrated model has been applied to few real debris flows. Thus, no valuable database of calibrated parameters has been created for this model. Moreover the SPH depth integrated model calculates erosion processes with the Hungr erosion law, which do not take into account the slope and therefore the terrain morphology. Both the lack of calibration work and the erosion law implemented are the limitations of this model. These limitations comprise the specific motivation for this thesis.

1.2 Objectives and structure of the thesis

To address the limitations above, the first focus of this thesis is the calibration of the model applying it to case studies. In this study, the model is applied to three real debris flows which occurred in Hong Kong. The first case is a classic debris flow. In both other events, erosion processes occurred along the flow path. The objective of this part is the test of the model ability to simulate, using realistic values for the input parameters, the characteristics of real events (travel distance and flow path characteristics, deposition pattern, flow velocity and debris volume). The second focus of this thesis is the implementation of the Egashira erosion law. The objective of this part is to improve the results obtained in the first part.

The remainder of this chapter give the main characteristics of debris flow processes and point out the more relevant parameters and magnitudes describing debris flow. Theory and methodology are presented in the chapter 2. First this chapter gives the main equations on which is based the latest version of the SPH depth integrated model. Then chapter 2 presents the erosion laws of Hungr and Egashira. Finally chapter 2 ends with the presentation of the code of the model. The results of this study cover the chapter 3 and 4. Chapter 3 corresponds to the calibration of the model applying it to three real debris flows. Chapter 4 follows with the implementation of the Egashira erosion law. The version of the model with the Egashira law is applied to two of the three case studies presented in chapter 3. In chapter 4, the results related to erosion processes obtained in chapter 3 are compared to

the results got with the Egashira erosion law. Chapter 5 presents general discussions about the results obtained in chapter 3 and 4. Finally this document ends with some conclusions of this study and the possible future research lines.

1.3 Debris flow: description of the processes

1.3.1 Definition of the term “debris flow”

1.3.1.1 A mass movement process

Debris flows are a type of mass wasting processes. Mass movement processes can be categorized following some parameters such as the release mechanism, the sort of material, the sediment composition, the proportion of the solid phase, the velocity, the time of the event, the slope of the movement plane, the material behavior, and the physical processes during the mass movement. Lots of classification of the mass wasting processes can be found in the literature. The classifications, which are the most accepted nowadays, are those of Varnes (1958), Hutchinson (1988) and Hungr et al. (2001).

Using these classifications and the definitions given by Stiny (1910) and Sharpe (1938), we can define debris flow as an extremely rapid flow in a steep confined channel which is deposited on a debris fan. It occurs after a flood and it is a viscous mass (non-newtonian fluid) consisting of water, soil, gravel, rocks and woods. It is a transient phenomenon.

Here mudflows can be mentioned because it is a particular kind of debris flow. In fact mudflows can be defined as a fine-grained debris flow. If it derives from volcanic sources, it is called lahar.

1.3.1.2 A mixture of water and sediments

In order to better understand the behavior of a debris flow, it is important to describe the material which forms a debris flow.

Hungr et al. (2001) explained the following terms “earth”, “debris” and “mud”.

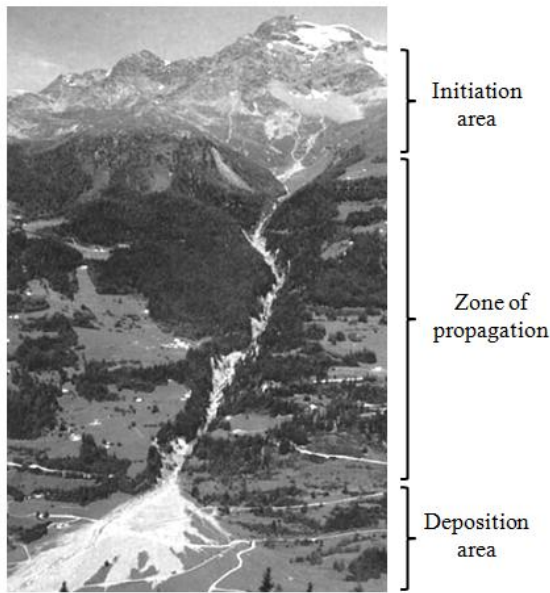
Earth refers to unsorted clayey colluviums, from clay or weathered clay-rich rocks. Earth consistency is closer to plastic limit than the liquid limit.

Debris represents loose unsorted material of low plasticity such as that produced by mass wasting processes, weathering, glacier transport, explosive volcanism, human activity (for instance mine debris). It is a mixture of sand, gravel, cobbles, and boulders and can contain organic material (logs, tree stump and tree trunk). Its consistency is non-plastic or weakly plastic.

Mud is defined as a soft, remoulded clayey soil whose matrix (sand and finer) is significantly plastic and whose liquidity index during motion is greater than 0.5.

Debris flows are composed of water and debris (solid particles). The solid phase occupies a larger volume than the liquid phase. The solid particles can be classified in two groups: fine particles (clay, silt and sand) and coarse particles (gravel, cobbles, boulders and organic particles too). Debris flows and mudflows have more or less the same water concentration but they differ in the solid particle size. Indeed solid particles of a debris flow are coarser than those of mudflow or lahars. Debris flows and mudflows are mixture of water and fine and coarse particles (cf. Appendix 1). Boulder diameters go up to a few meters. Generally boulders look suspended in the mass.

1.3.1.3 The three development phases of debris flow



Debris flow, as other gravitational mass movement, can be divided in three phases (Figure 1):

- Initiation phase, in which the initial mass is released
- Transition phase, in which the initial mass propagates along the travel path
- Deposition phase, when the mass stops and is deposited on a colluvial fan.

Figure 1. Debris flow of Val Varuna (1987)
SOURCE: Rickenmann, 1993

1.3.2 Initiation of the debris flow

1.3.2.1 Landslide-induced debris flow

Debris flows, mobilized from numerous small landslides or from a large and individual landslide, are the most common type. They occur when a debris slide or landslide changes into a debris flow. The process of forming debris flows from a static mass of water-laden soil, sediment or rock is called mobilization. Mobilization occurs under three conditions which are:

- the failure of the mass,
- a sufficient amount of water to saturate the mass,
- a sufficient conversion of the gravitational potential energy to the internal kinetic energy. The conversion of the energy changes the type of mass movement from a slide on a failure surface to a flow.

In addition to the water content in the soil, torrents can contribute to increase the water content. But in general, the required amount of water is already contained in the soil mass when the failure occurs. In this case, the water comes from rainfall infiltration or snow melt.

When the initial landslide mass rides on the torrent bed deposits (Figure 2.), an undrained loading process may generate a high pore-water pressure within the torrent deposits and this helps incorporate those deposit into moving mass. This phenomenon is called the liquefaction failure of the torrent deposits which results in the entrainment of the bed material. Thus the volume of the debris flow increases significantly.

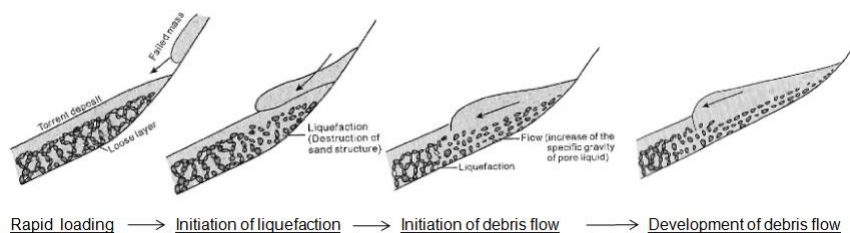


Figure 2. Illustration of the initiation of debris flow SOURCE: Sassa, 1985

1.3.2.2 Channel erosion type initiation

Debris flow can also initiate from channel bed and bank erosion. A sufficient water discharge is required to start the process of erosion. Rapidly the flow erodes the bed and mixes a large solid volume with the water. It occurs an irreversible chain of reactions which increases the solid concentration of the mixture.

Debris flow forms under required conditions which are channel bed and bank erosion capacity, water discharge, slope.

1.3.2.3 Other mechanisms of initiation

Debris flow can be also originated by different mechanisms:

- Earthquake may destabilize slope and causes landslides which are a source of material
- Natural dam may break and release sufficient material to form a debris flow. (Figure 3)
- Human activity, such as mining, may destabilize slopes
- Moraine lake may break up and deliver a large amount of water and rock.

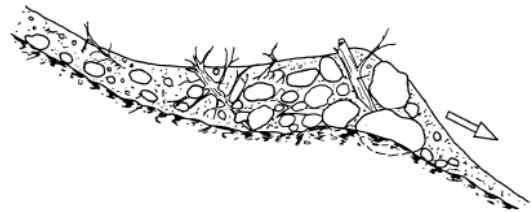


Figure 3. Natural dam composed of organic and soil debris **SOURCE:** Rickenmann, Lecture notes, 2007

1.3.2.4 Required conditions for the initiation

As it is mentioned in 1.3.2.1, the most relevant parameters controlling the initiation of a debris flow are slope, water and the amount of loose material. Some studies, led by debris flow researchers, have been done in order to determine thresholds beyond debris flow can initiate.

Slope plays an important role in the initiation of the debris flow because the stability of the slope is directly related to this parameter. Iverson et al. (1997) gathered various slope angles measured at site of debris flow initiation from landslide (c.f. Appendix 2). These data show that a slope steeper than 20° is required to initiate a landslide-triggered debris flow.

In both channel erosion and landslide initiation mechanisms, water is important. The water comes from rainfall or snowmelt. During the first mechanism, the water in the soil increases the pore water pressure and therefore decreases the resisting forces and thus the slope stability. The probability of occurrence of a landslide is higher. For the other mechanisms, precipitations increase the surface runoff and therefore water discharge of the torrent rises. Greater discharges are conducive to erosion.

Caine (1980) used data from 73 shallow landslides and debris flow to propose a threshold of rainfall intensity which has to be exceeded to initiate a debris flow. The limiting curve has the form (c.f. Appendix 3):

$$I = 14.82 \times (D^*)^{-0.39} \quad (1.1)$$

Where:

- I is the average rainfall intensity (in millimeters/hours)
- D^* is rainfall duration (in hours)

This equation was established for duration between 10 minutes and 10 days.

1.3.3 Propagation of the debris flow

Once debris flows are initiated, they flow down the channel. During the propagation phase, the flow has particular properties, which are characteristics of debris flows.

1.3.3.1 Flow variation in time

Debris flows are unsteady and non uniform flows because they move downslope as waves or series of waves. They are pulsating flows. Surges are separated by watery intersurge flow. Surges grow extempore due to flow instability, or due to the occurrence of consecutive landslides releasing material, or due to a slowdown of the flow followed by a boulder dam break. The volume of each surge may vary. The time separating surges is seconds to hours. Debris flow events can be composed of one to many tens waves.

For instance the Val Varuna debris flow, which occurred on the 18th of July in 1987, was a succession of about 10 surges. The volume of the debris flow was 200,000 m³ and the maximum volume per surge was 50,000 m³.

1.3.3.2 Geomorphologic characteristics

The solid concentration varies in the surge and thus debris flow surges have a typical longitudinal cross section. (Figure 4)

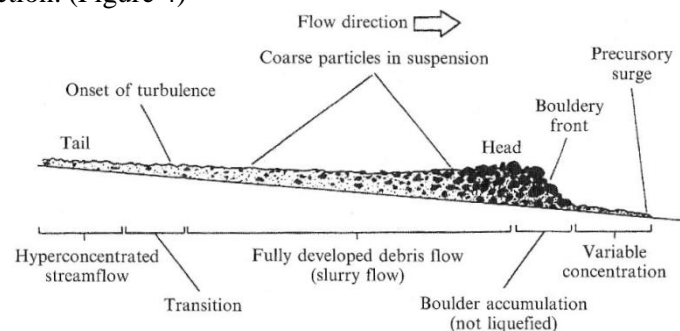


Figure 4. Sketch of a debris flow surge SOURCE: Pierson, 1986

Surges are composed of three parts. The tail, also called “afterflow”, is a flow of sediment-laden water. This part has the same characteristics as a debris flood, i.e. dilute and turbulent. This part continues until the next debris flow surge comes or until the debris flow event stops. The body of the surge is the middle part where there is a finer mass of liquefied debris. The last part of the surge is the head, which has an abrupt front. It carries the greatest concentration of large boulders and other debris. The head is free of matrix. The large sediment clasts can be incorporated and retained in the head if the flow takes them during the motion. Otherwise they come from the tail and migrate to the head by preferential transport. The depth of the flow and the concentration of solid decrease progressively from the head to the end of the tail (c.f. Appendix 4). The body of the surge is a water-saturated and liquefied fluid whereas the snout is unsaturated. The interactions between both parts give the debris flow motion and deposition characteristics, for instance the lateral levees.

Lateral levees are typical debris flow deposits. If a cross-section, through which a debris-flow is transiting, is observed, the plug flow and the marginal dead zones can be distinguished. (Figure 5) The plug flow corresponds to the central part of the flow in contact with the channel bed. The dead zones are the parts of the flow in contact with the side of the channel.

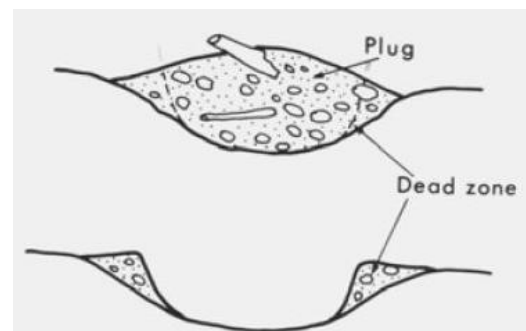


Figure 5. Channel cross section during the passage of a debris flow SOURCE: Eisbacher and Clague, 1984

If the same cross-section is observed after the passage of the debris flow, some deposition has taken place in the dead zone. These depositions are called the lateral levee. They are due to the flow depth because in the lateral part, the flow is thinner than in the central part. They are more frequent when the channel cross-section is wide. Generally the lateral levees have a depth of about 1 meter.

In the curve of the channel, because of centrifuge forces and rheological properties of the flow, the levee of the outside levee is higher than the inside one. (Figure 6)

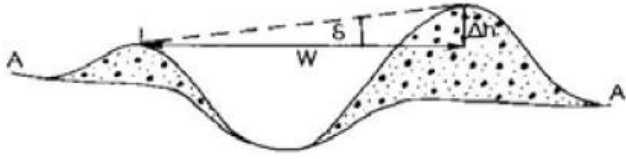


Figure 6. Sketch of superlevation
SOURCE: Selby (1993)

This phenomenon is called superlevation and enables to indicate dynamic behavior of the moving debris flow. For example it is possible to calculate the velocity using the following equation:

$$V = (k_1 r_c g \cos \beta \tan \delta)^{0.5} \quad (1.2)$$

Where:

- V is the mean velocity of the flow
- r_c is the radius of curvature of the bend
- g is the magnitude of the gravitational acceleration
- β is the channel slope (if $\beta > 15^\circ$, $\cos \beta$ can be neglected)
- Δh is the elevation difference between the inside and outside of the bend
- w is the width ($\tan \delta = \Delta h / w$)
- k_1 is the correction coefficient

The last geomorphologic characteristic of debris flows is the runout distance. The runout distance is defined as the length of the path over which travels debris flow. The runout distance is an important parameter to know where the deposition stops and where endangered zones are. Debris flow can run out over many 100 meters to many kilometers. For instance, the debris flow which occurred in Nevado del Ruiz in Colombia travelled over 10.3 km.

During the debris flow motion, the gravitational potential energy is converted to the work done during the event. The more efficiently this conversion is, the less energy is transformed to irrecoverable forms as heat and farther debris flow runs out. The total potential energy lost during the flow is:

$$E_p = MgH \quad (1.3)$$

Where:

- E_p is the total potential energy
- M is the masse of the debris flow
- g is the magnitude of the gravitational acceleration
- H is the vertical elevation of the debris flow source

The work done by the resisting forces over the runout distance, L , is:

$$W = MgRL \quad (1.4)$$

Where:

- W is the work
- R is a dimensionless net resistance coefficient

If the debris flow is considered to be an isothermal system, we obtain the following equation (Figure 7):

$$MgH = MgRL \quad (1.5)$$

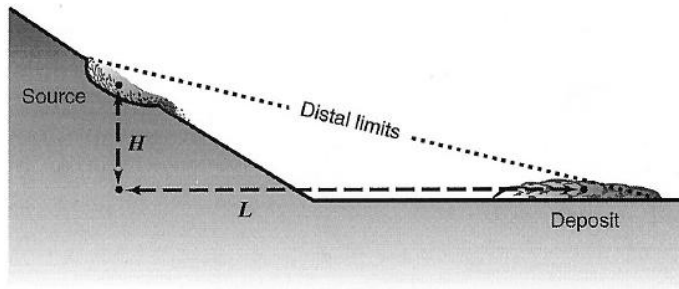


Figure 7. Schematic cross section defining H and L for debris flow paths
 SOURCE: Iverson, 1997

From equation (1.5), we get:

$$\frac{H}{L} = \frac{1}{R} \quad (1.6)$$

Some studies have proved the relationship between the quotient H/L and the volume of the debris flow, Rickenmann gave the following relationship: $L = 30 * (MH)^{(1/4)}$.

Run out distance of lahars and mudflows is larger than the one of normal debris flow because the concentration of water is larger in a lahar than a debris flow.

1.3.3.3 Material entrainment

After a debris flow event, the volume of material deposited is rarely the same as the volume involved in the flow during the initiation phase. Indeed, during the debris flow translation, the initial material may erode the channel bank and the channel bed. The result of this entrainment process is an increase of the debris flow volume. The Tsing Shan debris flow (c.f. 3.3) is a good example. The initial volume was 400 m^3 and the final volume was $20,000 \text{ m}^3$.

Two mechanisms are responsible of material entrainment. The first one is the bed destabilization. It is the result of the action of the drag forces on the base of the flow. The second mechanism is the consequence of the first one. After the channel bed erosion by a debris flow surge, the channel banks are destabilized and may release directly shallow landslide in this surge or release with delay material available for the next surge.

1.3.3.4 Flow velocity and impact forces

In order to better understand the shear behavior of debris flow material, the velocity profile (velocity=function (depth)) of a debris flow would be really relevant. Nevertheless it is quite difficult to get this information during field event observation.

Generally, field observation gives the mean velocity of the head of debris flow surge. After the Cruden and Varnes velocity scale (c.f. Appendix 5), debris flows are considered “extremely rapid” phenomena, i.e. faster than the human running velocity. However debris flow velocity varies strongly due to the different composition of sediment for each event. Velocity ranges from 0.5 m/s to 10 m/s . But in some extreme events, this limit can be exceeded and peak flow velocity of $15\text{-}20 \text{ m/s}$ can be reached. For example, the velocity of the Jiangua debris flow (in China), was about 14.5 m/s .

The high velocity gives to the debris flow a great pressure impact force, which is responsible of the destruction of settled area. Different studies have been carried out to estimate impact forces of debris flows. For example, Watanabe and Ikeya (1981) proposed the following relation to calculate the

impact forces magnitude:
$$P = \alpha \left(\frac{\gamma \times (v')^2}{g} \right) \quad (1.7)$$

Where:

- P is the pressure of the impact forces
- α is the velocity head coefficient
- γ is the unit weight of the debris flow material
- v' is the flow velocity head

If debris flows are assumed to be laminar flows (for this type of flow, $\alpha = 2$) and to have a unit weight equal to 2000 kg.m^{-3} , the last equation becomes:

$$P = 0.41 \times v^2 \quad (1.8)$$

Impact forces can be of several Newton per square meter. It explains the high danger of this natural process.

Debris flow material is a mass undergoing large and continuous deformations without important changes. The material is a non-Newtonian fluid due to the high viscosity. Thus debris flow can be considered as a one phase flow of viscous fluid. The velocity between the solid particle and the water is really small. In the flow, sedimentation is low because solids particles interact continuously. These interactions increase the material rigidity. Debris flows are laminar flows in fluid mechanics sense. When turbulence is caused by the agitation of debris flow head, the high viscosity of the fluid has a counter effect and the turbulence disappears. In particular case of mudflow, which are also considered as debris flow, the flow is turbulent. Fluid mechanism laws are used to describe debris flow processes. However debris flow dynamic cannot be depicted using only one viscosity parameter because debris flow has a heterogeneous composition and changes its fluid behavior over time.

1.3.3.5 Stresses in the flow

Debris flow mass undergoes deformations due to the different stresses applied to its particles. Because debris flows consist in a mixture of coarse particles (solid) and water or slurry (fluid), three different stresses are in the mixture:

- Solid stress
- Fluid stress
- Solid-fluid interaction stress

These stresses have both shear and normal components and each component may have both a quasi-static and an inertial components. Only the shear component, which has the greatest interest, will be described. The following expressions of the different stresses have been proposed by Iverson (1987)

The solid inertial stress is transmitted by the solid particle collision and is estimated by

$$\tau_{s(i)} \sim c \rho^{(s)} \dot{\gamma}^2 \delta^2 \quad (1.9)$$

Where:

- c is the solid volume fraction,
- $\rho^{(s)}$ is the mass density of the solid part (in kg/m^3),
- $\dot{\gamma} = \frac{v}{\delta}$ is the shear rate and v the velocity,
- δ is the mean diameter (in m).

Fluid undergoes also an internal shear stress which is

$$\tau_{f(i)} \sim c_f \rho^{(\alpha)} \dot{\gamma}^2 \delta^2 \quad (1.10)$$

Where:

- c_f is the fluid volume fraction,
- $\rho^{(\alpha)}$ is the mass density of the fluid part (in kg/m^3);

The quasi-static solid stress is caused by Coulomb sliding and enduring grain contacts. The weight of the particles existing above influences this stress and in consequence the stress increases with the depth. But the stress decreases if the static pressure of adjacent fluid increases. Therefore the quasi-static stress can be written as

$$\tau_{s(g)} \sim N v_s (\rho^{(s)} - \rho^{(\alpha)}) g \delta \tan \phi \quad (1.11)$$

Where:

- N is the number of grain above the layer of interest,
- g is the gravity,
- $\tan \phi$ is the internal angle of friction.

The quasi-static fluid stress comes from the Newton's law of viscosity:

$$\tau_{f(g)} \sim v_f \dot{\gamma} \mu \quad (1.12)$$

Where:

- μ is the viscosity (in Pa.s).

The solid-fluid interaction stress is due to the relative motion of fluid and solid components. As the other stresses, it may be composed of both inertial and quasi-static (viscous drag) component, but it has been proved by Iverson that inertial component can be neglected to the viscous coupling. The interaction stress can be estimated as

$$\tau_{s-f} \sim \frac{\dot{\gamma} \mu \delta^2}{k} \quad (1.13)$$

Where:

- k is the hydraulic permeability (in m²).

To summarize the different stresses, a list of relevant parameters influencing the stresses can be done:

- The shearing rate,
- The representative particle diameter,
- The flow depth,
- The particle density,
- The interstitial fluid density,
- The gravity acceleration,
- The apparent viscosity of interstitial fluid,
- The friction coefficient between particles,
- The velocity, and
- The hydraulic permeability.

The different stresses may explain the behavior of each particle of a debris flow, therefore these parameters are relevant to describe debris flow.

1.3.4 Deposition on the debris fan

The last phase of debris flows are the deposition of the debris.

1.3.4.1 Depositional area

Usually debris flows stop their propagation when they reach depositional fan, also referred to as colluvial fan. It is located after the channelized path of the flow. The fan is characterized by a decrease of the slope and an increase of the width. The typical fan slope is from 5% to 20%. As a debris flow reaches the fan, debris and water spread out. Flow velocity and flow depth decrease and material cannot flow anymore and is deposited. In general colluvium fan are settled area because it has good propriety for agriculture work and it is the only free space in narrow mountain valley to build infrastructures. The combination of high vulnerability and high probability of debris flow occurrence, gives to this area a large risk value. In this area, buildings, infrastructures and forest are often destroyed. Therefore part of them can be found in the deposited debris.

In some case, debris flows may stop in the channel. It occurs when, internal friction increases as the same time as volume, thickness, strength and channel slope decrease.

1.3.4.2 Lobate depositional shape

On the colluvial fan, debris deposit in a lobate shape. Lobes have a steep front composed of coarse boulders. (Figure8) Boundaries between debris deposits and clear ground cover are well delimited. As debris flows have a high density and viscosity, sediments are poorly sorted. Therefore the grain size distribution of the deposit is very wide. The deposit contains from clays to large boulders (several meters).



Figure 8. Debris flow deposit in lobate shape – SOURCE: Rickenmann, Lecture notes

As debris flow stops in the channel, the deposit can form a natural dam. This one can break during the passage of the next surge or can remain in the channel and be eroded by a further debris flow.

1.3.4.3 Large volume of deposited debris

The volume of a debris flow informs about the magnitude of the event. The volume of debris deposited is the following:

$$V_{tot} = V_{ini} + V_{ent} - V_{dep} \quad (1.14)$$

Where:

- V_{tot} is the total volume
- V_{ini} is the volume of the initial failures
- V_{ent} is the volume of the entrained debris
- V_{dep} is the volume of the deposited debris

Total volume of debris flow ranges from 100 m^3 to several $100,000 \text{ m}^3$ and for the biggest events many $1,000,000 \text{ m}^3$. For instance, the debris flow of December 1999 in Venezuela Stream San Julian had a volume of $2.6 \times 10^6 \text{ m}^3$.

1.3.5 Parameters describing debris flows

1.3.5.1 Relevant parameters

As the previous description of the phenomena shows, lots of parameters have to be considered to describe such flow. These parameters can be divided in two categories: terrain properties and flow properties. The terrain properties are the slope and characteristics of the ground surface (mainly the erodibility of the channel bed). The other parameters, which characterize the flow, are the sediment concentration, the particle density, the amount of water, the flow velocity, parameters describing stresses and the initial and final volumes.

1.3.5.2 Parameters used for debris flow modeling

A model uses data as input parameters to give results as output parameters. The parameters described previously are both input and output parameters.

The input parameters may be the following:

- The slope of the terrain is provided generally by a digital terrain model (DTM).
- The erodibility of the channel bed informs on the capacity of the bed to be eroded. The parameters representing the erodibility depend on the erosion law used in the model. (cf. subsection 2.5)
- A hydrograph gives the amount of water. Not all the models use a hydrograph as input data.
- The initial conditions (volume initial, initial flow depth) are required to describe the initial state of the flow. These data can be provided after a field survey.
- The density of the solid particles varies from 2500 kg/m^3 to 3000 kg/m^3 .
- The density of the fluid is from 1000 kg/m^3 to 1200 kg/m^3 .
- The viscosity of the fluid ranges from 0.001 Pa.s to 0.1 Pa.s .
- The internal angle of friction comprises between 25° to 45° .
- The solid volume fraction varies from 0.5 to 0.8, therefore the fluid volume fraction is between 0.2 and 0.5.
- In case of mudflow or debris flow with large amount of water, turbulence processes can occur. There is a turbulence coefficient to describe this phenomenon.

These previous typical values are given by Iverson in *The physics of debris flows* (1997).

The output parameters constitute the results after a simulation. They are calculated during the simulation. Generally the output parameters of a debris flow model are the velocity, the flow depth, the volume, and the position of the deposit.

1.4 Discussion

Debris flows are complex phenomena. It consists in the movement of a mixture of water and solid particles. During the event, the flow properties vary and therefore it is really difficult to model such flow. Lots of parameters are required to describe this type of flow. More numerous are the input parameters used, more difficult will be the calibration of the model.

Measurements of preceding parameters have to be done during the propagation of the flow because the properties of the flow depend on the character of debris motion. However debris flows are a transient phenomenon and are hard to forecast, thus it is quite impossible to survey a real event. And only few measurements of debris flows artificially released have been done due to the high cost and hard realization of such experiment. Therefore only few data exist. Moreover all the input parameters described previously have a wide range of possible values. Because of the few available data and a wide range of possible values, the calibration of a debris flow model is quite difficult.

On another hand, although all the parameters presented in this chapter are important to describe debris flow processes, debris flow models do not take into account all these parameters. In fact, debris flows models are based on constitutive laws which connect some of these parameters. The quality of debris flows models does not depend on the number of input parameters, but the quality depends on the ability to predict runout distance, flow velocity, deposition pattern and final volume of debris flows, implementing the constitutive laws.

In the next chapter, the parameters and the equations of the 2D SPH depth integrated are described in order to better understand how to use this model and to know how to calibrate the model.

2 METHODOLOGY: THE SPH DEPTH INTEGRATED MODEL

2.1 Introduction

Debris flows generate important yearly human and property losses. Predicting both the runout distance and the velocity through mathematical modeling of the propagation can avoid important losses. Moreover data from modeling can be used as input in risk studies, where hazardous areas are defined and appropriate protective measures are designed.

In the last decades, modeling of propagation stage has been largely carried out in the framework of the continuum mechanics, and a number of new and sophisticated numerical models are developed. Most of the available approaches handle the heterogeneous and multiphase moving mass as a single phase continuum. The model described here after consists on considering two phases, a granular skeleton with voids filled with either water or mud. If the shear resistance of the fluid phase can be neglected, the stress tensor in the mixture can be decomposed into a “pore pressure” and an effective stress, and the mechanical behavior of the mixture can be described by a system of differential equations governing the dynamics of each of the phases as well as the coupling among them. Once the required initial and boundary conditions are provided, the spatial and temporal integration of the system of differential equations can be carried out with numerical methods.

The depth integrated, coupled with the SPH model, is able to simulate the propagation of debris flows (and also landslides). It is based on a mathematical model, on rheological models and on a numerical model. The mathematical model, which is the coupled depth integrated model, comes from a velocity-pressure version of Biot-Zienkiewicz equations. Next, rheological models relate stress and strain tensor. Some rheological models are described in the second part of this chapter. The third part is dedicated to the description of basic concept regarding the SPH method, which constitutes the numerical model. Then the next subsection describes both the Egashira and Hungr erosion laws. The last part of this chapter presents the structure of the SPH code.

2.2 Mathematical model

2.2.1 Introduction

Soils are geomaterials with pores, which can be filled with water, air and other fluids. They are, therefore, multiphase materials, exhibiting a mechanical behavior governed by the coupling between all the phases. The pore pressure of the fluid, which fills the pores, plays a fundamental role in the behavior of these materials. When soils are considered as a mixture, the mass balance and momentum balance equation, and the constitutive equation can be formulated for each phase. The first model describing the coupling between solid and fluid phases was proposed by Biot (1941, 1955) for linear elastic materials. This initial model has been improved by further development at Swansea University, where Zienkiewicz and coworkers (1980, 1984, 1990, and 2000) extended to the theory of non-linear materials and large deformation problems. It is also worth mentioning the work of Lewis and Schrefler (1998), Coussy (1995) and de Boer (2000). This theoretical framework has not been applied to model the propagation of debris flow and landslides until recently. We can mention here the work of Hutchinson (1986), who proposed a sliding consolidation model to predict runout of landslides, the work of Iverson and Denlinger (2001), and those of Pastor et al. (2002).

2.2.2 Physical properties of geomaterials

Soils are heterogenic materials and they are generally a mixture of solid particles juxtaposed in an interstitial fluid (water and air), which fills the pores.

2.2.2.1 Porosity

The porosity (n) represents the part of the voids in the mixture, i.e. the quotient between the volume of voids (V_v) and the volume total (V_t).

$$n = \frac{V_v}{V_t} = \frac{V_v}{V_v + V_s} \quad (2.1)$$

Where V_s is the volume occupied by the solid phase.

From this definition the following relations can be defined (Figure 9):

$$V_s = (1-n) V_t \quad (2.2)$$

$$V_v = V_a + V_w = n V_t \quad (2.3)$$

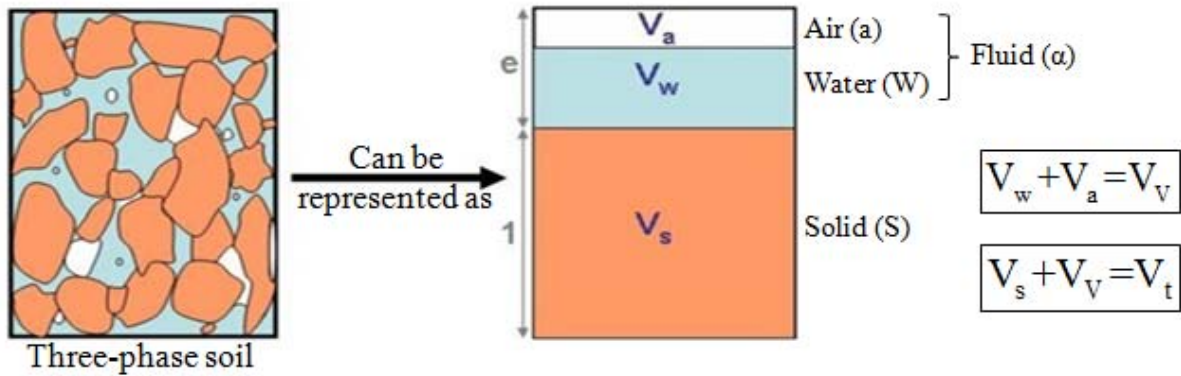


Figure 9. Sketch of representative sample of soil

2.2.2.2 Degree of saturation

The voids can be filled by air (a), water (w) or both. Assume that the fluid phases (α) are not miscible, the degree of saturation (S_α) can be defined for each fluid phase α as the quotient between the volume of voids occupied by the fluid and the total volume of voids.

$$S_\alpha = \frac{V_\alpha}{V_v} \quad (2.4)$$

In case that the fluids are air and water, the most frequent case, the fraction of water and air in the pores can be denominated as.

$$S_w = \frac{V_w}{V_v} \quad ; \quad S_a = \frac{V_a}{V_v} \quad (2.5)$$

Such as

$$S_w + S_a = 1 \quad (2.6)$$

According to the degree of saturation of the mixture, different type of soil can be distinguished (Figure 10):

- Saturated soils when $S_a = 0$ and $S_w = 1$, i.e. the voids are fill only by water,
- Dry soils when $S_a = 1$ and $S_w = 0$,
- And finally semi-saturated soils, when $0 < S_w < 1$, i.e. the interstitial space is occupied by water and air.

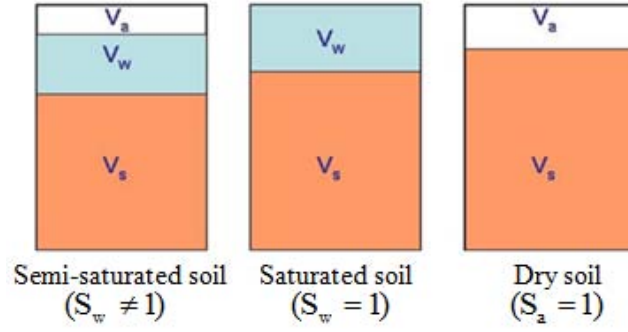


Figure 10. Representation of the different type of soils

2.2.2.3 Density

The density, $\rho^{(\alpha)}$, of the fluid phase (α) is defined as the quotient of the mass by the volume the phase. If ρ_a is considered as the density of the fluid of this phase, the density is determined by:

$$\rho^{(\alpha)} = nS_\alpha \rho_a \quad (2.7)$$

The density of the air (ρ_a) is strongly dependant of the pressure. The density of the water is almost constant and is $\rho_w = 1000 \text{ kg / m}^3$

For the solid phase, its density is:

$$\rho^{(s)} = (1-n)\rho_s \quad (2.8)$$

The density of the solid particle (ρ_s) is constant and takes a value of about 2650 kg/m^3 .

2.2.2.4 Darcy relative velocity

The relative velocity of Darcy (ω^α), which is the velocity of the fluid phase in respect to the velocity of the solid phase, links the velocity of the fluid phase (v^α) with the velocity of the solid phase (v^s) and is formulated as follow:

$$\omega^\alpha = nS_\alpha (v^\alpha - v^s) \quad (2.9)$$

The Darcy velocity can also be formulated as:

$$\omega^\alpha = nS_\alpha \omega_\alpha \quad (2.10)$$

From the relation (2.9), the velocity of the fluid phase can be presented as a function of the velocity of the solid phase:

$$v^\alpha = \frac{\omega^\alpha}{nS_\alpha} + v^s \quad (2.11)$$

2.2.2.5 Partial and effective stresses

The total Cauchy stress, σ , acting on the mixture can be decomposed in:

$$\sigma = \sigma^{(s)} + \sum_{\alpha=1}^{nfases} \sigma^{(\alpha)} \quad (2.12)$$

Where:

- $\sigma^{(s)}$ is the partial stress of the solid phase
- $\sigma^{(\alpha)}$ is the partial stress of the pore fluid phases.

These partial stresses, $\sigma^{(s)}$ and $\sigma^{(\alpha)}$ can be defined as:

$$\sigma^{(s)} = (1-n)\sigma_s \quad (2.13)$$

and

$$\sigma^{(\alpha)} = nS_\alpha\sigma_\alpha \quad (2.14)$$

As the same time the partial stress, $\sigma^{(\alpha)}$, can be decomposed, as usually in mechanic of continuum medium, in hydrostatic and deviatoric components:

$$\sigma^{(\alpha)} = -nS_\alpha p_\alpha \mathbf{I} + nS_\alpha \mathbf{s}_\alpha \quad (2.15)$$

Where:

- $\mathbf{s}_\alpha = dev(\sigma_\alpha)$ is the deviatoric component,
- \mathbf{I} is the tensor identity of second order
- p_α is the pressure of the fluid phase α .

In case that the interstitial fluid is only water, the deviatoric component can be neglected and therefore the partial stress is:

$$\sigma^{(w)} = -nS_w p_w \mathbf{I} \quad (2.16)$$

The averaged pressure, \bar{p} , of the fluid phase can be introduced as:

$$\bar{p} = \sum_{\alpha=1}^{nfases} p^{(\alpha)} = \sum_{\alpha=1}^{nfases} S_\alpha p_\alpha \quad (2.17)$$

In general case that the three phases (solid, water and air) are present in the soil, the total Cauchy stress is:

$$\sigma = \sigma^{(s)} + \sigma^{(w)} + \sigma^{(a)} \quad (2.18)$$

With

$$\begin{aligned} \sigma^{(s)} = (1-n)\sigma_s \quad ; \quad \sigma^{(w)} = -nS_w p_w \mathbf{I} \quad y \quad \bar{p} = S_w p_w + S_a p_a \\ \sigma^{(a)} = -nS_a p_a \mathbf{I} \end{aligned}$$

On the other hand, the tensor of effective stress comes from the following expression:

$$\sigma = \sigma' - \bar{p}\mathbf{I} + n \sum_{\alpha=1}^{nfase} S_\alpha \mathbf{s}_\alpha \quad (2.19)$$

In case that the deviatoric tension of the interstitial fluid is null, the effective tension becomes:

$$\sigma' = \sigma + \bar{p}\mathbf{I} \quad (2.20)$$

2.2.3 General model

2.2.3.1 Definition of the material derivative

The material derivative or rate of change following a particle, $\frac{D}{Dt}$, represents the velocity of change for a fixed fluid particle and is defined as the following operator:

$$\frac{D}{Dt} = \frac{\partial}{\partial t} + v \cdot \text{grad} \quad (2.21)$$

Therefore, in general case of a scalar material property ϕ associated to particles, we would have:

$$\frac{D\phi}{Dt} = \frac{\partial\phi}{\partial t} + \frac{\partial\phi}{\partial x_j} v_j \quad (2.22)$$

Or in a more compact manner:

$$\frac{D\phi}{Dt} = \frac{\partial\phi}{\partial t} + v_i \text{grad} \phi \quad (2.23)$$

Thus, the material derivative is the combination of:

- The local derivative, $\frac{\partial\Phi}{\partial t}$, which represent the quantity if change in time in a fixed location.
- The convective derivatives, $v_i \text{grad} \Phi$, which represent the change due to the movement of the fluid particle from a position to another one, where the fluid properties are spatially different.

2.2.3.2 Equations of general models

The general model consists into the following equations:

First the equations of mass balance for the solid and fluid phases are

$$\frac{D^{(s)}\rho^{(s)}}{Dt} + \rho^{(s)} \text{div} \mathbf{v}^{(s)} = 0 \quad (2.24)$$

$$\frac{D^{(\alpha)}\rho^{(\alpha)}}{Dt} + \rho^{(\alpha)} \text{div} \mathbf{v}^{(\alpha)} = 0 \quad (2.25)$$

Secondly the equations of linear momentum balance for the solid and fluid:

$$\rho^{(\alpha)} \frac{D^{(\alpha)}\mathbf{v}^{(\alpha)}}{Dt} = \rho^{(\alpha)} \mathbf{b} + \text{div} \boldsymbol{\sigma}^{(\alpha)} - k_\alpha^{-1} \boldsymbol{\omega}^{(\alpha)} \quad (2.26)$$

$$\rho^{(s)} \frac{D^{(s)}\mathbf{v}^{(s)}}{Dt} = \rho^{(s)} \mathbf{b} + \text{div} \boldsymbol{\sigma}^{(s)} + k_\alpha^{-1} \boldsymbol{\omega}^{(\alpha)} \quad (2.27)$$

Where:

- \mathbf{b} is the term for the external forces
- $\boldsymbol{\sigma}^{(s)}$ is partial stress tensor of Cauchy for the solid phase
- $\boldsymbol{\sigma}^{(\alpha)}$ is partial stress tensor of Cauchy for the fluid phase
- k_α is the permeability of the phase α
- $\boldsymbol{\omega}^{(\alpha)}$ the Darcy relative velocity

Thirdly the model is based on constitutive equations (c.f. subsection 2.3).

Finally the last equations are the kinetic equations which link the velocities to rate of deformation tensors:

$$D^\alpha = \frac{1}{2} \left(\frac{\partial v_i^\alpha}{\partial x_j} + \frac{\partial v_j^\alpha}{\partial x_i} \right) \quad (2.28)$$

Where D represents the rate of deformation tensor

2.2.4 The V-p_w model

2.2.4.1 Introduction

The behavior of a soil is governed by the coupling between the different phases. In this framework can be found the mathematic model “u-p_w” proposed by Zienkiewicz and his team from the University of Swansea, (C.T.Chang, P.Bettess, T.Shiomi, A.H.C.Chan, M.Pastor, O.K.Paul and B.Schrefler). They enlarged the theory of Biot (1941, 1955) to a non lineal material and large

deformations (1980, 1984, 1990, 2000). The model “u- p_w” is formulated with movements of the solid skeleton and pore pressures, whereas the model “V- p_w” is formulated with velocities instead of movements.

2.2.4.2 Equations of the model V-p_w

Assuming that the relative velocities between the fluid phases and their accelerations are small, the model V-p_w can be formulated in function of the velocities of the solid skeleton and the relative velocities of the fluid to the skeleton (Darcy velocity). Moreover, assuming that the soil is saturated, the model consists to the following equations:

$$- \operatorname{div} (-k_w \operatorname{grad} p_w) + \operatorname{div} v^s = 0 \quad (2.29)$$

$$- \rho \frac{D^{(s)} v^s}{Dt} = \rho b + \operatorname{div} \sigma \quad (2.30)$$

- The constitutive (c.f. subsection 2.3) and kinetic equations (equation 2.28) are the same as the ones of the general model.

Remark: In case that the density is constant, the mass balance of the mixture is reduced to:

$$\operatorname{div} v^s = 0 \quad (2.31)$$

2.2.5 Propagation-consolidation approximation

In the last subsections, models, which can be applied to several general problems in soil mechanics, have been considered. The analysis of landslides and debris flows, due to their shape and geometrical properties, allow interesting simplifications. In this section, the “propagation – consolidation” models, where pore pressure dissipation takes place along the normal to the terrain surface are presented. In the next subsection (2.2.6) the second simplification, which is the depth integration, is presented.

An important aspect is that fast flows involve two physical phenomena which appear in equations above:

- Consolidation and dissipation of pore pressure
- Propagation.

The x_1 and x_2 axes will be chosen on a plane close to that of the slope, or a horizontal one and the x_3 axis will be normal to this plane. The V-p_w model can be cast in a dimensionless form by introducing

$$\begin{aligned} \hat{x}_1 &= x_1 / L & \hat{x}_2 &= x_2 / L & \hat{x}_3 &= x_3 / H \\ \hat{v}_1 &= v_1 / \sqrt{gL} & \hat{v}_2 &= v_2 / \sqrt{gL} & \hat{v}_3 &= v_3 / \varepsilon \sqrt{gL} \\ \hat{\sigma} &= \sigma / \rho_0 g H & \hat{p}_w &= p_w / \rho_0 g H \end{aligned} \quad (2.32)$$

Assuming that the velocity field can be decomposed as

$$\hat{v} = \hat{v}_0 + \hat{v}_1 \quad (2.33)$$

And the pore pressure field decomposed as:

$$\hat{p}_w = \hat{p}_{w_0} + \hat{p}_{w_1} \quad (2.34)$$

In this way, the perturbed field v_1 can be identified as the velocity field corresponding to the unidimensional consolidation and v_0 as the velocity field corresponding to propagation. This result is of paramount importance, and clarifies the assumptions which should be made when modeling these phenomena.

2.2.5.1 Equations of the model after the “propagation - consolidation” approximations

The starting point is the balance equations for saturated soils obtained above, equations (equation 2.29) and (equation 2.30). The “propagation – consolidation” model consists in the following set of partial derivative equations:

$$\rho \frac{Dv_0}{Dt} = \rho b + \text{div } \sigma \quad (2.35)$$

$$\text{div } v_0^{(s)} = 0 \quad (2.36)$$

$$\frac{1}{K_T} \frac{Dp_w}{Dt} = \frac{\partial}{\partial x_3} \left(k_w \frac{\partial p_w}{\partial x_3} \right) \quad (2.37)$$

Where K_T is the volumetric rigidity of the solid skeleton.

Taking into account the incompressibility condition (equation 2.36), equation (2.35) can be written in the conservative form as:

$$\rho \frac{\partial v_i}{\partial t} + \frac{\partial}{\partial x_j} (\rho v_i v_j) = \frac{\partial}{\partial x_j} (\sigma_{ij}) + \rho b_i \quad (2.38)$$

More details about the calculation to get these equations are given in Appendix 6.

2.2.6 Depth integrated model

2.2.6.1 Introduction

Many fast, catastrophic landslides have an averaged depths which are small in comparison with their length or width. In this case, it is possible to simplify the 3D propagation-consolidation model described in Section 2.2.5 by integrating its equations along the vertical axis. The resulting 2D depth integrated model presents an excellent combination of accuracy and simplicity providing important information such as velocity of propagation, time to reach a particular place, depth of the flow at a certain location, etc.

The following model derives from the equation presented in the last section (equations 2.35 to 2.38). Next, the sub indexes “0” in the velocity field and “1” in the pressure field will be dropped. These equations will be integrated along the direction normal to the terrain surface using the Leibnitz and Reynolds theorem.

The reference system given in figure 11 will be used.

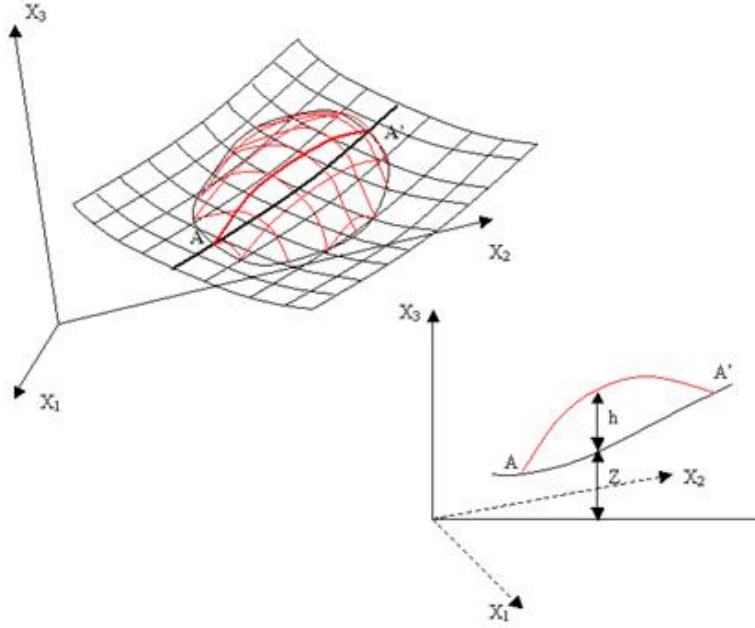


Figure 11. Reference system and notation used in the analysis – Source: Thesis of B.Hadad

2.2.6.2 Integration along depth of the propagation equations

- Balance of mass:

The equation of mass balance is integrated along depth and gives:

$$\frac{\partial h}{\partial t} + \frac{\partial}{\partial x_j} (h \bar{v}_j) = 0 \quad \text{con } j=1,2 \quad (2.39)$$

Where \bar{v}_j is the component of the averaged velocity along the axis X_j .

In general, the basal surface do not change and $\frac{\partial}{\partial t} (h + z) = \frac{\partial h}{\partial t}$ but in some occasions, erosion occurs and this phenomena has to be taken into account by introducing an erosion rate, e_r , defined as:

$$e_r = -\frac{\partial z}{\partial t} \quad (2.40)$$

Thus, $\frac{\partial}{\partial t} (z + h) = \frac{\partial h}{\partial t} - e_r$ is obtained and has to be integrated to the equation of mass balance.

Therefore the depth integrated equation of the balance of mass is:

$$\frac{\partial h}{\partial t} + \frac{\partial}{\partial x_j} (h \bar{v}_j) = e_r \quad \text{con } j=1,2 \quad (2.41)$$

- Balance of linear momentum:

Assuming that the stresses on the surface are null and the stresses at the bottom are given by:

$$t^B = -\rho g h \text{ grad } Z - \tau_b \quad (2.42)$$

The equation (2.38) of linear momentum balance is integrated along the depth and gives:

$$\rho \frac{D(h\bar{v})}{Dt} + \text{grad} \left(\frac{1}{2} \rho g h^2 \right) = -\frac{1}{\rho} e_r \bar{v} + \rho b h + \text{div} (h \bar{s}) - \rho g h \text{ grad } Z - \tau_b - \rho h \bar{v} \text{ div} (\bar{v}) \quad (2.43)$$

2.2.6.3 Integration along depth of the consolidation equation

The existence of a saturated layer with a height, h_s , at the bottom of the flow has been considered (Hung, 1995). Therefore, the decrease of the pore pressure is caused by the vertical consolidation of this layer.

The consolidation coefficient, C_v , can be introduced:

$$C_v = \frac{k_w}{\gamma_w c'} = K_T k_w \quad (2.44)$$

Where:

- C_v is the consolidation coefficient,
- k_w is the permeability,
- γ_w is the specific weight of the fluid,
- c' the compressibility of the material, and
- K_T is the volumetric rigidity of the solid skeleton.

The depth integrated consolidation equation comes from the integration of the equation (2.37) and is:

$$\frac{\partial}{\partial t} \left(P_{w_1} h \right) + \frac{\partial}{\partial x_k} \left(\bar{v}_k P_{w_1} h \right) = - \frac{\pi^2}{4h^2} c_v P_{w_1} \quad (2.45)$$

2.2.6.4 Equation of the depth integrated model

Assuming a fixed volume, which corresponds to a column integrated along depth and moving with an averaged velocity, the equations of the depth integrated model are:

$$\begin{aligned} \frac{Dh}{Dt} + h \operatorname{div}(\bar{v}) &= e_r \\ \rho \frac{D(h\bar{v})}{Dt} + \operatorname{grad} \left(\frac{1}{2} \rho g h^2 \right) &= - \frac{1}{\rho} e_r \bar{v} + \rho b h + \operatorname{div}(h\bar{s}) - \rho g h \operatorname{grad} Z - \tau_b - \rho h \bar{v} \operatorname{div}(\bar{v}) \quad (2.46) \\ \frac{\partial}{\partial t} \left(P_{w_1} h \right) + \frac{\partial}{\partial x_k} \left(\bar{v}_k P_{w_1} h \right) &= - \frac{\pi^2}{4h^2} c_v P_{w_1} \end{aligned}$$

More details about the calculation to get these equations are given in Appendix 7.

This system of equation can be solved using numerous numerical methods (finite difference, finite elements, finite volume or meshless method as SPH). In the section 2.4, the discretization using the SPH method is described.

2.3 Rheological models of a fluidized material

2.3.1 Introduction

Mathematical models described in the preceding section have to be completed using constitutive or rheological models relating stress and strain tensors. In the case of solid soils, great effort has been devoted in the past decades to develop accurate constitutive models accounting for the most important aspects of soil behaviour, and today there is a wide choice between many elastoplastic, viscoplastic, hypoplastic, non linear incremental and generalized plasticity models, just to number some of them.

One important limitation is that, so far, no satisfactory model able to reproduce the behaviour of soil mixtures under the full range of strain rates which appear in fast slope movement problems. After liquefaction or fluidization has taken place, the soil behaves in a fluid like manner, and models used here are different from those used for reproducing the triggering mechanism. Indeed, both classes of models for solid or fluidized soils are often referred to as “constitutive equations” and “rheological models”.

Basically, there are two different lines of research dedicated to the behavior of fluidized geomaterials. The first one started with the work of Takahashi (1978). He considered that the material, which forms debris flows, consists in particles scattered in a viscous fluid. Takahashi assumed that the Bagnold’s theory (Bagnold 1954) could be applied to debris flows. The Bagnold’s theory refers to fast flows compound of uniform and spherical particles. The Bagnold’s model is valid to describe the behavior of extremely rapid flows of dry mass formed by non cohesion particles. However this model is not advisable in case of a mixture of water and soil, such debris flows (Coussot & Meunier, 1996). Moreover, the Bagnold’s theory is not able to predict and estimate the yield stress of debris flows, which is one of the main characteristics. The yield stress corresponds to the minima stress, which must be exceeded to release the flow. Based on this behavior, a second line of research has been developed, which is to consider the material of debris flows as a viscoplastic fluid. Several models have been developed from experimental data got with rheometer (Wan, 1982; Locat & Demers, 1988; O’Brien & Julien, 1988; Coussot & Piau, 1994a, 1995c; Wang et al., 1994), from theoretical considerations (Chen, 1988; Julien & Lan, 1991) and from field observations (Fink et al., 1981; Johnson & Rodine, 1984; Pierson, 1986; Whipple & Dunne, 1992). The most famous viscoplastic model is the one of Bingham (Bingham & Green, 1919), first used by Johnson (1970) and Daido (1971) to model debris flows.

In the last decade more focus has been given to the solid fraction within a debris flow mixture and models from geotechnical science have been employed.

In this chapter, only the frictional and the Voellmy model will be presented, although the SPH depth integrated model proposes the use of the following models: Newton’s, Bagnold’s, Bingham’s and frictional model. However in these reports, all the study cases have been solved either using a frictional model or using the Voellmy model.

2.3.2 The frictional model and the Voellmy model

Most of the depth integrated model use simple rheological law due to the difficulty to implement them. The frictional model is one of the available simple laws and comes from the Cheng & Ling model, neglecting the cohesion and viscous terms.

In this case, the vertical distribution of the shear stress (τ) and the strength of Mohr-Coulomb(s) are given by:

$$\tau(z) = \rho g (h - z) \sin \theta \quad (2.47)$$

And

$$s(z) = \rho'_d g (h - z) \cos \theta \tan \phi \quad (2.48)$$

Where:

- h is the flow depth
- z is the elevation
- θ is the slope
- ρ'_d is submerged density of particle and is equal to $\rho_s - \rho_w$.

Since both distributions are linear, if the values (2.47) and (2.48) are equal at the bottom, these values will be equal along the depth. This condition reads:

$$\tan \theta = \frac{\rho'_d}{\rho} \quad (2.49)$$

In this case, it is not possible to get the velocity distribution without additional information. For that reason, the depth integrated models purely frictional cannot include a factor of linear momentum correction.

Concerning the basal friction, it is usually approximated by:

$$\tau_b = -\rho'_d gh \tan \phi \frac{\bar{v}_i}{|\bar{v}|} \quad (2.50)$$

In some cases, the fluidized soil flows on a bottom compound of another material. In this case, if the friction angle, δ , between both materials is smaller than the one of the fluidized soil, the basal shear stress is given by:

$$\tau_b = -\rho'_d gh \tan \phi_b \frac{\bar{v}_i}{|\bar{v}|} \quad (2.51)$$

Where the friction angle with the bottom, ϕ_b , is:

$$\phi_b = \min(\delta, \phi) \quad (2.52)$$

In this simplified model, the pore pressure can be included:

$$\tau_b = -\left(\rho'_d gh \tan \phi_b - p_w^b\right) \frac{\bar{v}_i}{|\bar{v}|} \quad (2.53)$$

From the last equation, it can be concluded that the pore pressure has an effect similar to a decrease of friction angle.

Another interesting model, which is demonstrated to be suitable for debris flow modeling is the Voellmy model (Hung, 1995 and Evans et al., 2001). In this model, the friction law can be written as:

$$\tau_b = -\left\{ \left(\rho'_d gh \tan \phi_b - p_w^b \right) \frac{\bar{v}_i}{|\bar{v}|} + \rho g \frac{|\bar{v}|}{\zeta} \frac{\bar{v}_i}{|\bar{v}|} \right\} \quad (2.54)$$

In this model, a friction term, due to the turbulence dissipation, has been introduced. ζ is the turbulence coefficient and takes into account the depth of the basal layer, where most of the shear deformation takes part.

2.4 Numerical model: SPH approximation

2.4.1 Introduction

Numerical models have become a fundamental tool to obtain approximations to engineering and science problems for which there is no available analytical solution.

In the last decades, a new group of methods, characterized for not using meshes but only nodes has been developed. They have been called “meshless”, and provide an interesting and powerful alternative to more classical numerical methods such as finite differences, finite elements and finite volumes. Their name comes from the fact that they do not rely on meshes but on points to approximate functions or derivatives. As examples of these methods, it is worth mentioning the Diffuse Element Method introduced by Nayroles, Touzot and Villon (1992), the Element Free Galerkin Method of Belytschko, Lu and Gu (1994), the hp-cloud method of Duarte and Oden (1996), the Partition of Unity Method of Babuska and Melenk (1995), the Finite Point Method introduced by Oñate and Iddlesohn (1998) and, finally, the Smoothed Particle Hydrodynamics Method which is the technique described in this text.

Smoothed particle hydrodynamics is a meshless method based on discretized forms of integral approximations of functions and derivatives. The method was introduced independently by Lucy

(1977) and Gingold and Monaghan (1977) and applied to astrophysical modeling, a domain where SPH presents important advantages over other methods (see also the work of Monaghan and Latanzio 1985). Goods review can be found in Benz (1990), Monaghan (1992) or in the recent texts of Liu and Liu (2003) or Li and Liu (2004).

SPH is well suited for hydrodynamics, and researchers have applied it to a variety of problems, like those described in Gingold and Monaghan (1982), Monaghan and Gingold (1983), Takeda, Miyama and Sekiya (1994), Monaghan (1994), Monaghan and Kocharyan (1995), Monaghan and Kos (1999), Monaghan, Cas, Kos, and Hallworth (1999), Bonet and S. Kulasegaram (2000), and Monaghan, Kos and Issa (2003).

2.4.2 *Integral approximation of functions and derivatives: General aspects*

Smoothed particle hydrodynamics is based on the possibility of approximating a given function $\phi(x)$ and its spatial derivatives by integral approximations defined in terms of a kernel. In a second step these integral representations are approximated numerically by a class of numerical integration based on a set of discrete point or nodes, without having to define any “element”.

More details about the integral approximation of functions and derivatives are given in Appendix 8.

2.4.3 *SPH discretization of integral approximation of functions and derivatives*

2.4.3.1 *Discrete approximation of functions*

The approximations of functions and derivatives given in the preceding Section are valid at continuum level. If the information is stored in a discrete manner, for instance, in a series of points or nodes, it is necessary to construct discrete approximations. The SPH method introduces the concept of “particles”, to which information concerning field variables and their derivatives is linked. But indeed, they are nodes in the same way that in finite elements or finite differences.

All operations are to be referred to nodes. A set of particles or nodes $\{x_K\}$ with $K=1 \dots N$ will be introduced. Of course, the level of approximation will depend on how the nodes are spaced and on their location. The classical finite element strategy of having more nodes in those zones where larger gradients are expected is of application here.



Figure 12. *SPH mesh to model a debris flow in Hong Kong*

As an example, the figure 12 gives an SPH mesh of nodes which will be used to model a fast slope movement. It is interesting to notice that we are using two different meshes, one to describe the terrain topography and the SPH mesh. Another interesting aspect is that SPH nodes are grouped in different places, which are the sources of the avalanching movement.

Figure 13 illustrates the numerical integration procedure performed:

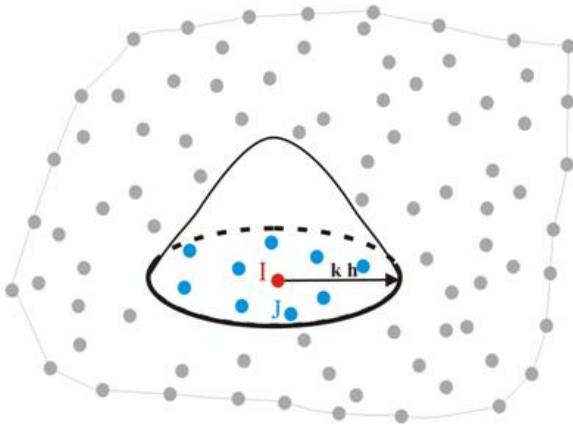


Figure 13. Nodes and numerical integration in a SPH mesh

More details about the integral approximation of functions and derivatives are given in Appendix 9.

The balance of mass, the balance of momentum and the pore pressure dissipation are discretized. (c.f. equations 9.63, 9.71 and 9.75 – from appendix 9.) The discretization results in ordinary differential equations (ODE). The resulting ODE equations can be integrated using a scheme such as Runge Kutta 4th order.

2.4.4 Numerical solution of an ODE using Runge Kutta 4th (RK4) order method

The Runge Kutta 4th (RK4) method is used by the SPH depth integrated model to solve the ordinary differential equation. The description of this method is presented in the appendix 10.

2.5 Erosion law

This subsection describes the erosion laws which are implemented in the 2D depth integrated model.

2.5.1 Introduction

There are only few studies which attempted to quantify the erosion during debris flow events because erosion can be only estimated during field survey. After an event, it is hard to estimate the evolution of the following parameters along the flow path: flow velocity, flow depth, transported debris volume. Therefore it is difficult to find a relation between the erosion rate and the others magnitudes characterizing debris flows. Few erosion laws are available in the literature. In this chapter two erosion laws are presented, the Hungr erosion law and the Egashira erosion law. The first one was already implemented in the SPH depth integrated model, whereas the second has been implemented for this study.

2.5.2 Description of the Hungr erosion law (Hungr 1995)

Hungr used an erosion rate (as defined by the equation 2.40), which increases in proportion to the flow depth, resulting in a depth proportional distribution of entrained material and exponential growth of the debris flow with displacement. Although this law is empirical, it has a physical basis. Indeed the changes in the stress conditions leading to a failure in the bottom of the flow path and with this the entrainment of the material are related to the changes in the total bed-normal stress and thus with the flow depth.

This empirical law is based on a input parameter, E_s , given by the user. E_s is a displacement erosion rate, so called growth rate. This parameter represents the bed-normal depth eroded per unit flow depth and unit displacement. The dimension of this parameter is L^{-1} . It is worth mentioning the difference with the erosion rate, e_r , defined in the equation (2.40). In fact e_r is a time dependant erosion rate and not a displacement erosion rate. The growth rate, E_s , is independent to the flow velocity. For example when E_s is constant and takes the value 0.01, the debris flow volume increases by 1% when it travels 1 meter.

The Hungr law consists of the relation between the erosion rate e_r and the growth rate E_s :

$$e_r = E_s \times h \times v \quad (2.55)$$

where h is the flow depth and v is the depth averaged flow velocity.

From equation (2.55) it is possible to derive the volume change during a time step dt . The SPH model gives the following relation:

$$h_i = \frac{V_i}{A_i} \quad (2.56)$$

Where:

- V_i is the volume of a particle i
- h_i is the height of the particle i
- A_i is the area of the particle i (constant over the time).

Reminding that $e_r = \frac{\Delta h}{dt}$ and after equation (2.55), the volume change during dt can be obtained as:

$$\begin{aligned} \frac{\Delta h_i}{dt} &= E_s h_i v_i \\ \Delta h_i &= \frac{\Delta V_i}{A_i} = E_s h_i \times (v_i dt) \\ \Rightarrow \Delta V_i &= E_s \times (h_i A_i) \times \Delta s \quad \text{where } \Delta s \text{ is the path travelled during } dt \\ \Rightarrow \Delta V_i &= E_s V_i \Delta s \end{aligned} \quad (2.57)$$

The last equation corresponds to the natural exponential growth equation for a debris flow.

In the SPH code, the two main lines of the subroutine ‘‘Erosion_SW’’ are:

- The calculation of the erosion rate after the equation (2.55), and
- The actualization of the new debris flow volume:

$$V_i = V_i + \frac{dt \times e_r \times V_i}{h_i} \quad (2.58)$$

The subroutine ‘‘Erosion_SW’’ is called at the end of each time step and takes the update value for the velocity and the flow depth got after the Runge Kutta approximation.

2.5.3 Description of the Egashira erosion law (Egashira1993)

The Egashira law is based on flume tests, as well as numerical and dimensional analyses. Egashira assumes that the bed slope is always adjusted to its equilibrium in case of debris flows travelling over an erodible bed.

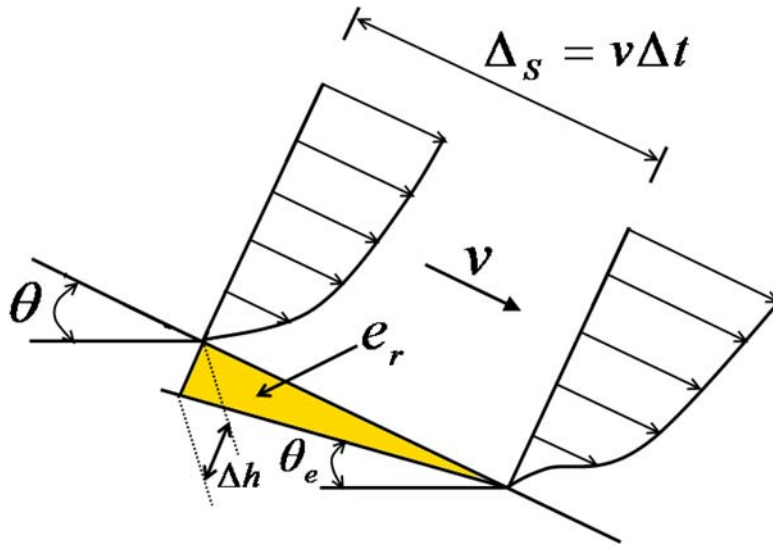


Figure 14. *Definition sketch of the erosion rate*

Referring to the figure 14, the mass conservation law of eroded material yield can be applied:

$$e_r \Delta_s = e_r v \Delta t = c_* v \Delta h \quad (2.59)$$

Where:

- c_* is the sediment concentration by volume of bed sediment (of the non moving layer),
- θ is the bed slope,
- θ_e is the equilibrium bed slope, and
- the other magnitudes are have already been defined previously.

From the equation 2.59, the next step is obtained:

$$\frac{e_r}{v} = c_* \frac{\Delta h}{\Delta_s} \quad (2.60)$$

From here, Egashira derived his erosion law, substituting in the last equation the term $\theta - \theta_e = \arctan\left(\frac{\Delta h}{\Delta_s}\right)$:

$$e_r = c_* v \tan(\theta - \theta_e) \quad (2.61)$$

with:

$$\theta_e = \tan^{-1} \left\{ \frac{(\rho_s - \rho_w)c}{(\rho_s - \rho_w)c + \rho_w} \tan \phi \right\} \quad (2.62)$$

where:

- ρ_s the mass density of the sediment particle
- ρ_w the mass density of the water
- c the sediment concentration of the debris flow by volume, and
- ϕ the internal friction angle of the bed approximated by the basal friction angle $\tan \phi_b$.

The Egashira law corresponds to equations (2.61) and (2.62) and requires the value of the sediment concentration of the debris flow and the sediment concentration (by volume) of the bed sediment. Both of these magnitudes have not been used in the SPH depth integrated model yet.

Therefore, they have to be introduced as input parameter. In comparison with the Hungr law, where the user has to input only one parameter (the erosion coefficient, or growth rate), in the Egashira law, the user has to input two parameters which are:

- c , the sediment concentration of the debris flow by volume
- c_* , the sediment concentration by volume of bed sediment (of the non moving layer).

Experimentally, Takahashi (1992) has proved that the sediment concentration of the debris flow (c) cannot exceed the value $0.9c_*$. Therefore the following has to be always verified:

$$c < 0.9c_* \quad (2.63)$$

The SPH depth integrated model verifies this condition in case that the input parameters given by the user would have not verified it.

2.5.4 Adaptation of the Egashira erosion law to the SPH depth integrated model

2.5.4.1 Deposition processes

The Egashira law is also able to estimate the volume of sediment, which is deposited during the flow. In fact, when $\theta_e > \theta$, the erosion rate, e_r , is negative and it corresponds to deposition of sediments and a decrease of debris flow volume. When $e_r < 0$, $\frac{dh}{dt} < 0$. Therefore the height of the particle would decrease. However in the SPH depth integrated model, the deposition processes are not represented by a decrease of the particle height but deposition are represented by a particle velocity equal to 0 m/s. Therefore, the Egashira erosion law has been implemented to estimate only the erosion processes, i.e. when the erosion rate is negative for a particle, there is no change of its volume.

2.5.4.2 Influence of the erosion processes on the sediment concentration

When bed material is eroded, it is incorporated in the flow. So erosion processes provide an increase of the volumetric sediment concentration. Therefore the density of the mixture is not constant. However to solve the equation (2.36) of the SPH depth integrated model, the assumption that the density of the mixture is constant was made. Normally the sediment concentration changes over time, however it is not possible in the current version of the SPH depth integrated model. Therefore the assumption was made that when the erosion processes occurs, the sediment concentration of the flow remains constant.

This assumption has already been done in other debris flow model using the Egashira law. For instance, Bruffau (2000) implements in his 1D debris flow model the Egashira law assuming that the sediment concentration remains constant.

2.5.4.3 Empirical factor

After its implementation, the Egashira erosion law has been tested applying it to the case studies of the 1990 and 2000 Tsing Shan debris flows. The first results were not in accordance with the observations. Indeed, for these two case studies, the final volume of debris was of in the order of more than 10^9 m³. The erosion rate obtained by the Egashira law was really larger than the erosion rate calculated after the Hungr law. Moreover, it was not possible to define values for the input parameters, bed sediment concentration and debris flow sediment concentration, which produced realistic results. Therefore an empirical factor to modify the Egashira law has been proposed:

$$e_r = Kc_*v \tan(\theta - \theta_e) \quad (2.64)$$

with:

$$\theta_e = \tan^{-1} \left\{ \frac{(\rho_s - \rho_w)c}{(\rho_s - \rho_w)c + \rho_w} \tan \phi \right\} \quad (2.65)$$

where K is the empirical factor.

The modified Egashira law requires three input parameters that the user of the model has to find in order to get a realistic simulation. These parameters are:

- c , the sediment concentration of the debris flow by volume
- c_* , the sediment concentration by volume of bed sediment (of the non moving layer), and
- K , the empirical factor.

The chapter 4 concerns the calibration of this law and the comparison of the results obtained after the Hungr and the Egashira law.

2.6 SPH code

2.6.1 Introduction

The SPH code is written in FORTRAN 90 language. The code implements the equations presented previously in the last subsections of this chapter. The program consists of 7 modules. 4 of them are the base of program:

- 2 modules related to the variables (declaration and definition)
- 1 module related to the topography of the terrain
- the main module.

The 3 others modules are not used at the same time. Each is used to simulate a type natural hazards:

- a module to simulate debris flows and landslides (the “shallow water” module)
- a module to solve the Navier-Stokes equations
- a module to simulation the propagation of waves in reservoir initiated by a landslide

The input data are containing in three files:

- The “*.top” file contains information about the topography. The information can be either a DTM or points of a mesh that the SPH generates.
- The “*.pts” file contains all the nodes or particles which are the initial mass of the flow.
- The “*.dat” file contains information about the type of event, the control parameters of the simulation and the material properties.

As the work is related to debris flows, only the “shallow water” module has been used. In the next subsection, the 4 modules consisting the base of the program and the “shallow water” has been described in a diagram. In this figure only the main subroutine has been represented.

2.6.2 Overview of the SPH code structure

The Structure of the SPH code is summarized in figure 15 where the relation between the modules and the subroutine are indicated in a scheme.

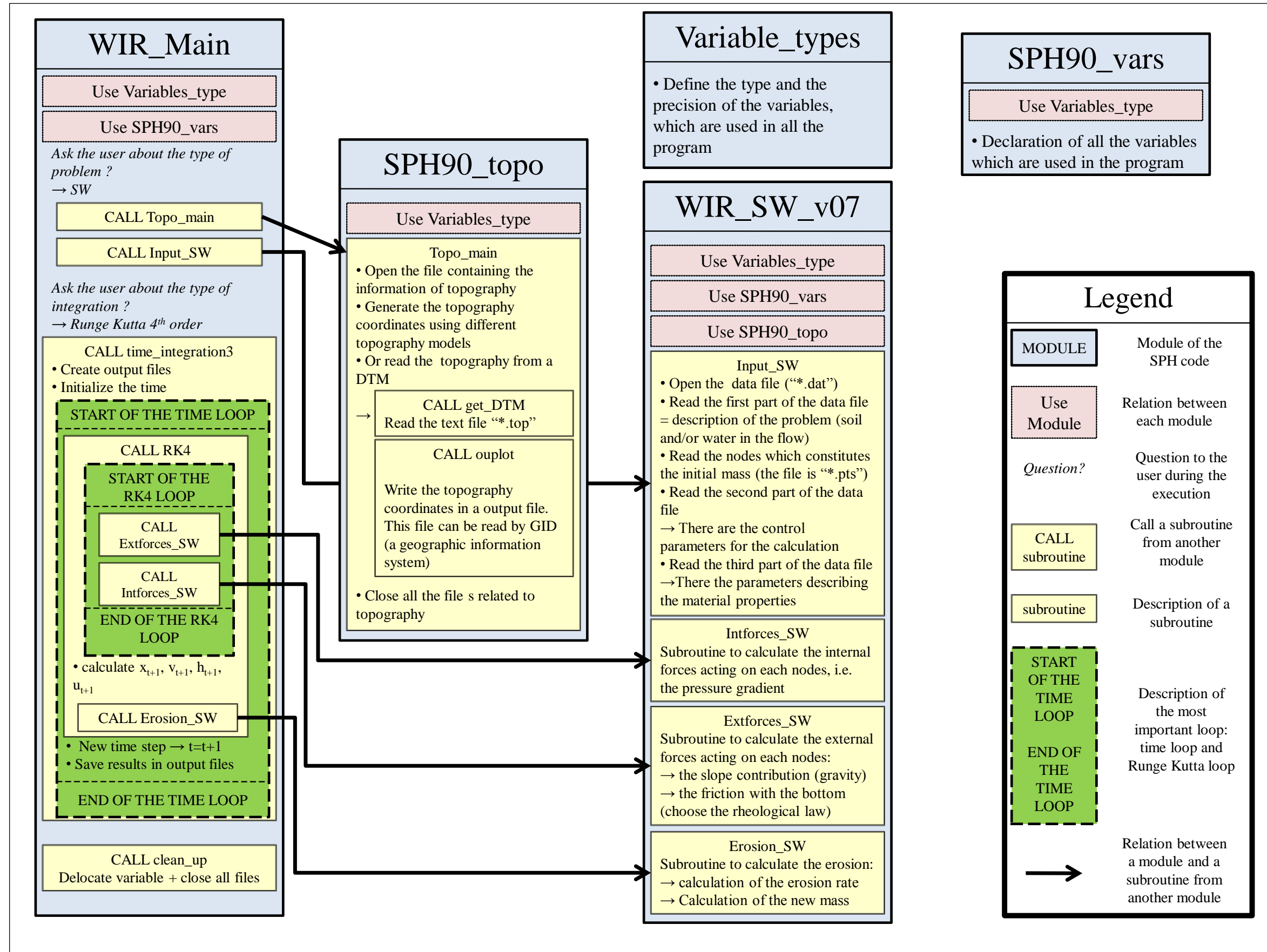


Figure 15. Overview of the SPH code structure

2.6.3 Implementation of the Egashira erosion law

As the Egashira law was not integrated in the model yet, some modifications have been done in order to implement this law. These modifications are presented in this subsection.

2.6.3.1 Parameters of the subroutine "Erosion_SW"

The input parameters for the erosion law are found in the data file (*.dat). The constant number 4, called "const(4)", takes positive or negative value in order to choose the erosion law. Figure 16 summarizes all the possible cases.

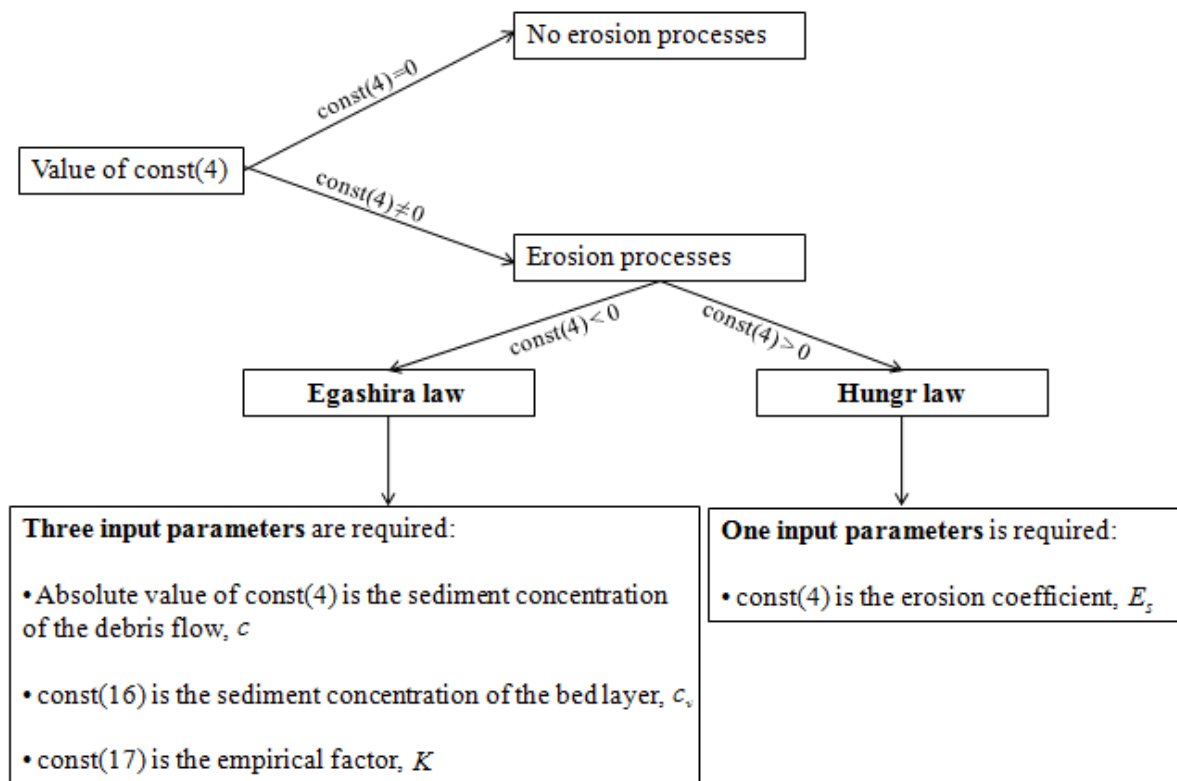


Figure 16. Parameters of the subroutine "Erosion_SW"

2.6.3.2 Structure of the code of the Erosion_SW subroutine

The subroutine "Erosion_SW" has been modified to integrate the Egashira law. The part concerning the Hungr law has not been modified. The structure of the subroutine integrated both laws is represented in Figure 17.

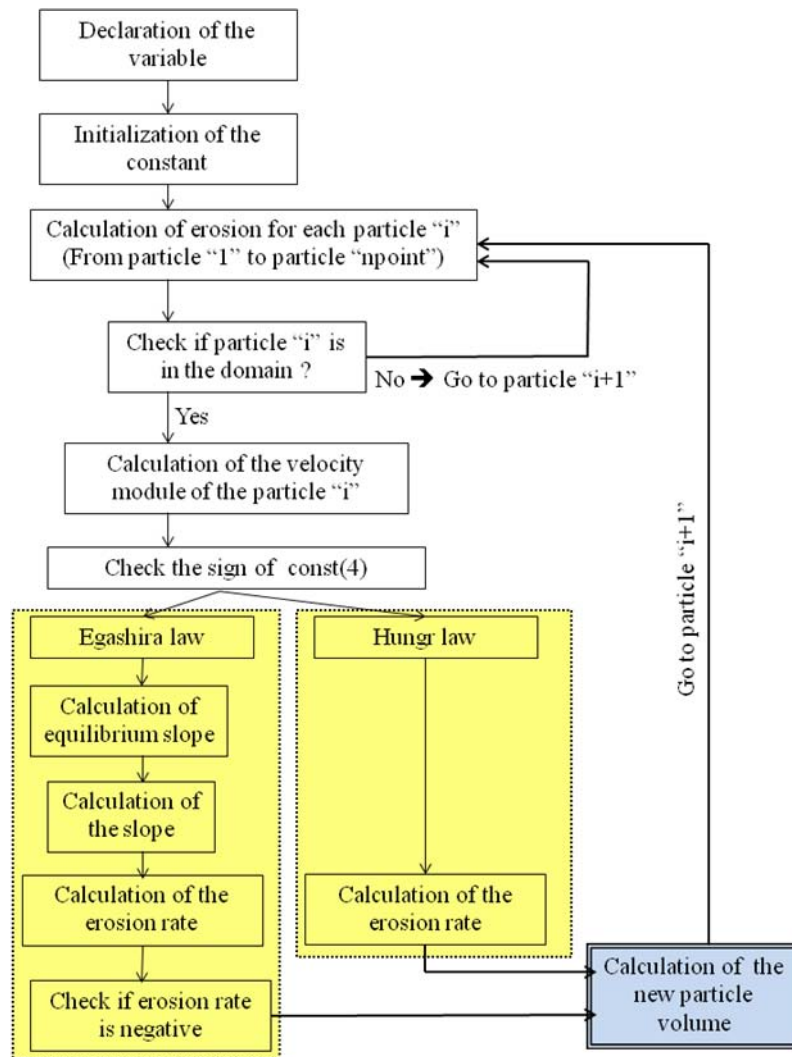


Figure 17. Structure of the subroutine "Erosion_SW"

Currently the subroutine is able to calculate the erosion rate after the Egashira and the Hungr law. The user decides, which law he wants to use when he inputs the value of the constant "const(4)". This subroutine is called at each time step and actualizes for each particle its volume after that erosion processes occurs.

Remark:

As it appears in the equations (2.46.a), (2.46.b), the erosion rate is present in the equations of balance. As a consequence, in the SPH depth integrated model, the erosion rate is calculated in the subroutine "Erosion_SW", as well as when the momentum of the particles is calculated. Therefore other parts of the SPH depth integrated code have been also modified to implement the Egashira law.

2.7 Discussion of the parameters used in the model

Parameters of the final equations of the SPH depth integrated model can be compared to the parameters described in the subsection 1.3. These parameters have been defined as most important parameters to describe debris flow phenomena. Are they included in the equations of the model?

Parameters presented in the first chapter (cf. subsection 1.4)	Is the parameter taken into account in the 2D SPH depth integrated model?	Which does mathematical symbol represent the parameters in the equations?	Which equation contains the parameters?	Which type of parameter is?
Slope	Yes	Z (the elevation)	(2.46.b)	Input parameter
Erodibility	Yes	e_r (The erosion rate)	(2.46.a)	Calibration parameter
Amount of water (given by hydrograph)	No			
Initial volume	Yes	Deduce from the initial height: h	(2.46.a.b.c)	Input parameter
Viscosity	No			
Angle of friction of the mixture	Yes	$\tan \phi$	(2.53) and (2.54)	Calibration parameter
Volumetric solid fraction	Yes	c	(2.65)	Calibration parameter
Turbulence coefficient	Yes	ζ (Voellmy coefficient)	(2.54)	Calibration parameter
Flow velocity	Yes	\bar{v} (Depth integrated velocity)	(2.46.a.b.c)	Output parameter
Flow depth	Yes	h	(2.46.a.b.c)	Input parameter + Output parameter
Volume	Yes	Deduce from the flow depth		Output parameter
Position of the deposit	Yes	Deduce from the velocity		Output parameter

Table 1. Comparison of the parameters describing debris flow processes from the SPH model and those from the literature

Remarks:

- (i) The equations (2.46) are derivative equations of the following magnitudes: flow depth (h), flow velocity (v) and pore pressure (p_w). Flow depth and flow velocity are the two main output magnitudes of the model because once the value of these magnitudes are known, the flow deposition and flow impact can be delimited. Pore pressure cannot be considered as an output parameter because its value is not relevant to assess debris flows. Nevertheless the model requires this magnitude as it includes the pore pressure effects to derive in a more accurate way the flow velocity and flow depth.
- (ii) The slope is required and thus the topography of the terrain is required. This information is contained in a digital terrain model (DTM).

(iii) To calculate the basal friction, the frictional model requires some parameters which are the density of the mixture (ρ), the angle of friction ($\tan(\phi)$) and in case of Voellmy model, the turbulence coefficient (ζ). These parameters are the main calibration parameters of the model. The user gives a value for this parameter before starting the simulation.

The SPH depth integrated model takes into consideration most of the parameters which have been defined relevant to describe debris flows. However to define SPH depth integrated model as a “good” model, the model need to be calibrated. For the calibration, the model must be applied to case studies and values for the input parameters have to be found in order to match as well as possible the results of the simulation with the real event. The chapter 3 presents the results of the model calibration.

3 RESULTS –PART 1: CALIBRATION OF THE MODEL

3.1 Introduction to the calibration

In order to assess the validity of a model, it is necessary to choose (i) the mathematical model, (ii) the rheological model and (iii) the numerical model implementing the two first. Concerning the numerical model, it has already been validated against problem with an analytical solution, such as the depth integrated solution of dam break over a wet or a dry bottom

Concerning the rheological model, comparisons can only be made using simple fluids whose rheological properties have been obtained in laboratory. In general, laboratory tests are rarely available for fluidized soils involved in catastrophic debris flow. Therefore, the common solution to validate the rheological model is to use numerical models (here: the SPH method), implement the approximated mathematical model (here: the depth integrated model) and a rheological model, and to back-calculate observations from past events. The output parameters have to be compared to the field observation in order to assess the model.

To validate and calibrate the SPH depth integrated model, three case studies are used. They are presented in this chapter. These case studies are well-documented debris flows events which occurred in Hong Kong. In the first case there is no erosion phenomenon. The two last examples are debris flows with erosion and therefore, increase of volume during the event.

3.2 The Sham Tseng San Tsuen Debris Flow, Hong Kong

3.2.1 *Description of the event*

3.2.1.1 *Description of the site*

In the morning of 23 August 1999, a debris flow occurred in the hillside above the Sham Tseng San Tsuen. This debris flow destroyed a house (referred as House No. 38 in the following figures) and damaged several other buildings of the village. The debris flow ran a little bit over the House No.38 passing through a nullah (southern Asia term for a concrete lined channel designed to prevent flooding). Unfortunately, there was one fatality and thirteen injuries. The topography of the rocky stream in which passed the debris flow is very rugged and several steep steps including a 10m high waterfall can be observed. The debris flow path has a length of 210 m and the elevation difference between the starting area to the village (deposit area) is 90 m, with an averaged slope of 24° . The averaged width of the channel is 1.5 m and ranges from 0.8 m (close to the top of the waterfall) to 10 m where some material was deposited (downstream to the waterfall). The catchment above the waterfall is approximately 27 000m². Figure 18 gives an aerial view of the debris flow path and Figure 19 shows the topography of the terrain.

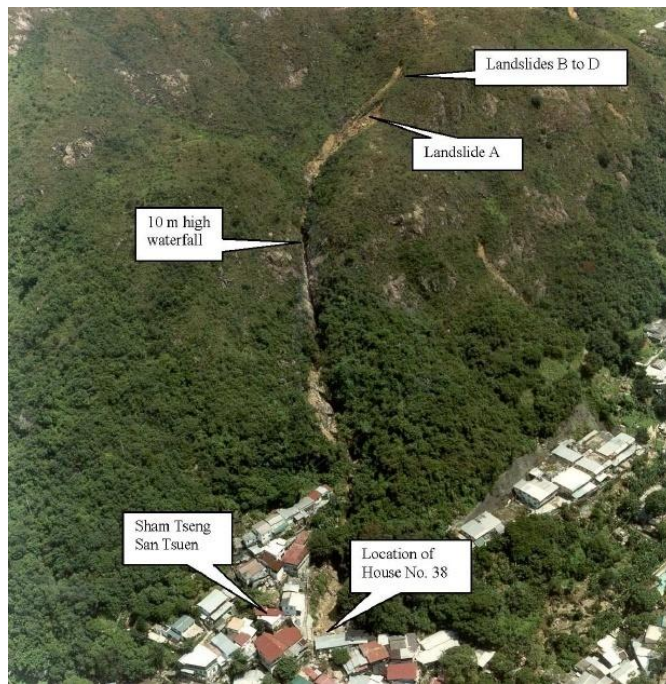


Figure 18. *General view of the Sham Tseng San Tsuen debris flow – Source: Geotechnical Engineering Office of Hong Kong*



Figure 19. *Topography of the terrain*

3.2.1.2 A starting zone formed by four landslides

The debris flow initiated from four landslides which occurred at the natural, lightly vegetated hillslope. In figure 20 the landslides are referred as Landslides A to D. The slope gradient at the Landslide A varies from 32° to 37° and the slope at the Landslide B to D is steeper (40° to 45°). The landslide scars are situated 10 m below the crest of the hillside, thus the catchment area above the starting zone is quite small. The Landslide A is the biggest one and has a maximum depth of 3.8 m. The volume of the Landslide A is approximately 600 m^3 , of which 480 m^3 came from the initial scar, leaving a main scarp of 14 m wide and 3.8 m high. The other landslides are much smaller in comparison with the Landslide A. Indeed the total volume involved in Landslide B to D is about 20 m^3 . The history of the site shows that the area, where took place Landslide A to D, was affected by an extensive hillfire (probably in the 1995-1996 dry season). This fire removed much of the vegetation cover of the landslide area and charred the top soil. Therefore the soil was more susceptible to direct infiltration. The final deposition volume was about 420 m^3 .



Figure 20. *Oblique Aerial View of the Landslide Sites (Photograph Taken on 26 August 1999)– Source: Geotechnical Engineering Office of Hong Kong*

3.2.1.3 *A geology favorable to slope instability*

The lithology in the landslide area consisted of predominantly medium-grained megacrystic granite in contact with fine-grained granite near the northern end of the main scarp of Landslide A. The rock in the main scarp of Landslide A varies in weathering grade, with highly to moderately decomposed at the southern end and slightly to moderately decomposed near the northern end of the scarp. In the rock mass of the main scarp of Landslide A, three joints are present. The persistence of joint is up to 5 m. These joints are likely to be filled by water during rainfall precipitation that would increase the cleft-water pressure and thus increase the instability of the rock mass. Behind and in the front of the main scarp, colluviums are present. In the front, the thickness of colluvium increases gradually to a depth of 1.2 m. The landslide debris overlies a layer of colluvium (up to 0.3 m thick) which overlies complete decomposed granite. It is likely that the local surface of rupture lies at the interface formed between the complete decomposed granite and the colluvium, although the main part of the failure surface was in the colluvium layer.

The shear strength properties of the surface colluvium and the complete decomposed granite were assessed by consolidated undrained triaxial compression tests using samples recovered from the Landslide site A. The angle of shearing resistance of the surface colluvium and complete decomposed granite are respectively 37° and 38° with zero cohesion.

3.2.1.4 *Important rainfall precipitation before the event*

Rainfall data were obtained from an automatic rain gauge situated approximately 300 m to the south of the landslides. The rain was heavy in the morning of 23 August 1999 up to the time of debris flow at about 7:30 a.m. The 24-hour and 12-hour rainfall before the event were 479 mm and 341 mm, respectively. The maximum 60-minute rainfall was recorded as 127 mm between 5:25 a.m. The 2-hour rainfall corresponds to a 49-years event.

3.2.1.5 *Probable sequence of events and cause of initiation*

The probable sequence of events has been reconstructed from eye-witnesses, records of Hong Kong Police and field mapping. According to witnesses, the debris flow impacted the village at 7:30 a.m. The first incident of the early morning was a water flow across a house and along the road. This flow took place at about 6:15 a.m. to 6:30 a.m. This period consists of the maximum rolling 15-minute rainfall intensity (42 mm/hour). Field mapping shows that the trail from Landslide A has blot out the trail from Landslide B to C. Therefore Landslide A occurred probably after the others. The debris flow was a result of Landslide A. Back analyses of the debris flow movement, together with the superelevation of debris marks, indicate that it probably took a relatively short time to travel down the 210 m (of order of less than one minute).

The landslides A to D were triggered by rainfall. The landslides were probably caused by elevated water pressure within the surface colluvium. This elevated pressure may result from the hydrogeological setting. Indeed the thin mantle of boulder colluvium overlies a less permeable layer composed of dense weathered colluvium and locally weathered granite. That is favorable to increase the water pressure in the colluvium layer. Moreover the presence of partially filled joints increased the instability. It is worth mentioning that the hillfire was also responsible of the instability of the hillside due to a high infiltration rate of water and a light vegetation cover.

3.2.2 *Parameters of the calibration*

In addition to the topography, three others parameters are required to simulate this case. First the density of the mixture is 2000 g/m^3 . The rheological model used to simulate this debris flow is the Voellmy fluid. The parameters found to best fit the re-constructed even from August 1999 were a turbulence coefficient of 1000 m/s^2 , a basal friction angle of about 16° ($\tan \phi_b = 0.3$) and zero cohesion. The following results are obtained using these values for the parameterization.

3.2.3 Results

The results obtained from the simulation are presented in the figures 21 and 22:

In Figure 21, the field observations are represented by a red line and the model predictions are the blue area

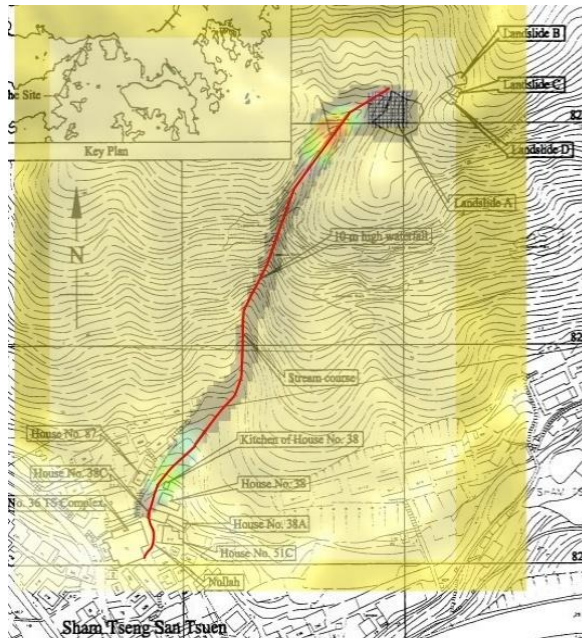


Figure 21. *Sham Tseng San Tsuen debris flow: Model predictions versus Field observations*

The model provides a good match of the general extent in the real event and the distribution of the deposit after the simulation with the SPH depth integrated model. The model uses a constant bulk basal friction of 16° to give the best result.

A Voellmy fluid has been chosen to model this event. The debris flow was formed after a small landslide (only 600 m^3 of debris) and large rainfall precipitation (49-years event). Therefore the assumption that the mixture did not have a large sediment concentration can be done. Thus turbulence phenomenon could appear during the flow. In this case, the Voellmy model is more adapted than the frictional model because the Voellmy model takes into consideration the turbulence phenomena. The simulation has also been done with the frictional model and the results were worse. Indeed the runout distance is shorter when the rheological model used the frictional model. The reason is that the frictional model is more adapted for flows with a high concentration of sediment.

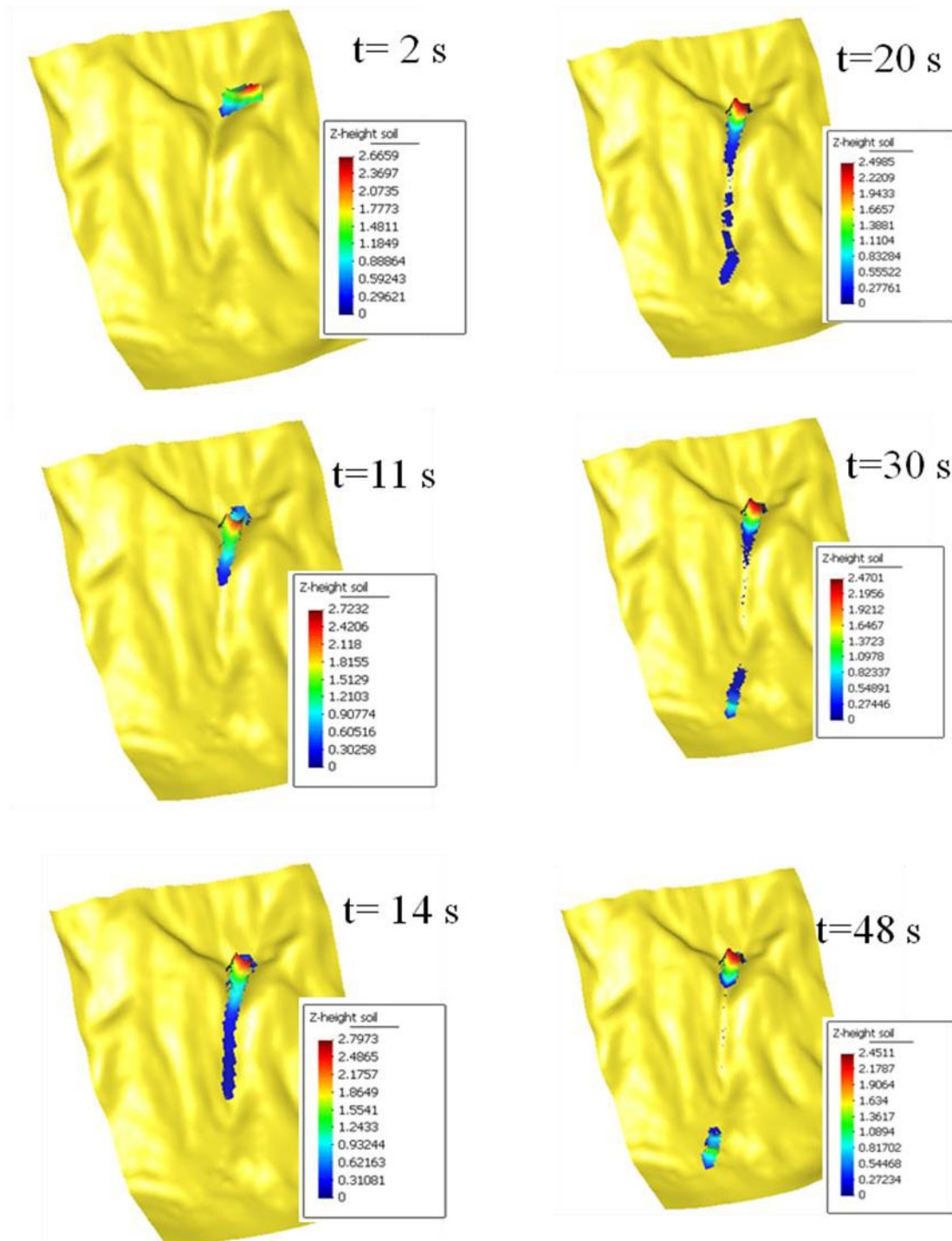


Figure 22. *Sham Tseng San Tsuen debris flow: Model predictions - evolution of the debris flow*

Another conclusive result is the event duration. Indeed, after some witnesses, the debris flow occurred during a short time, less than one minute. The simulation respects the event duration, because after 48 seconds, all the debris have flowed through the channel and are deposited in the village (Figure 22). Figure 21 shows that the debris have passed over the house No. 38 and it is in agreement with the reality, in which the house was destroyed. However, in the real event, the flow continues after the House No. 38 and passed through a nullah (a concrete lined channel designed to prevent flooding). In the simulation, the flow stopped at the House No. 38 and thus a little bit before than in the reality.

During the event, some debris was deposited downstream to the waterfall. In the simulation, this deposition cannot be observed. Figure 23 shows that debris are deposited but at the top of the waterfall. It is the only results in contradiction with the field observations.

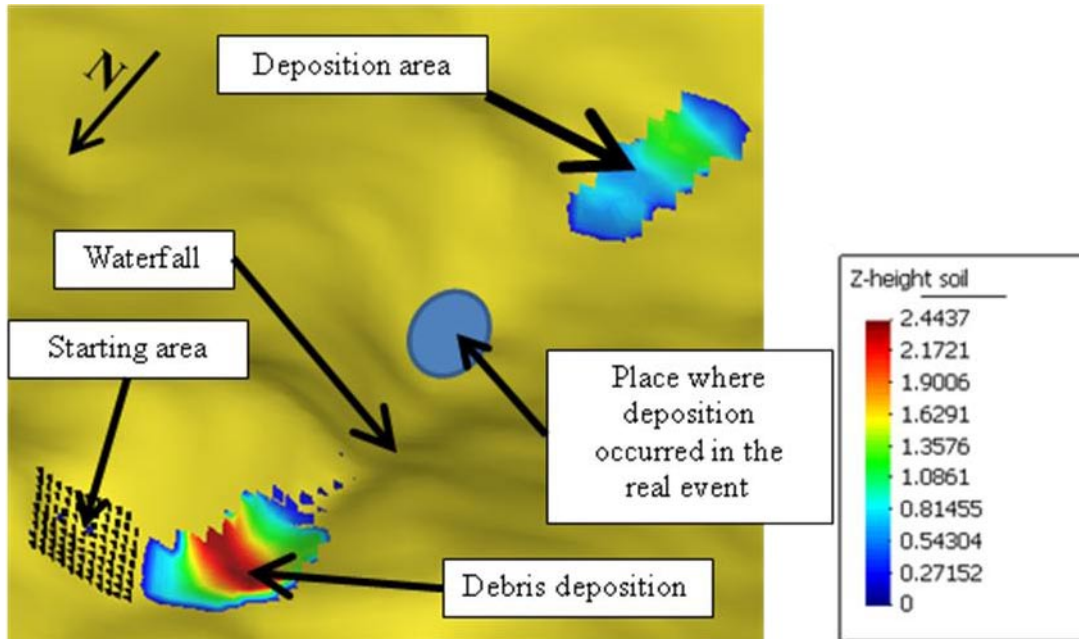


Figure 23. *Sham Tseng San Tsuen debris flow: Debris deposition after the event*

These results are acceptable and show that the SPH depth integrated model can be used to model real events. However the results, especially the deposition area, can be improved.

In the two next case study, the simulated event are more complex than the Sham Tseng San Tsuen debris flow because erosion processes occurred and therefore the volume increases gradually during the flow.

3.3 The 1990 Tsing Shan Debris Flow, Hong Kong

3.3.1 Description of the event

3.3.1.1 Introduction



Figure 24. *General view of the 1990 Tsing Shan debris flow – Source: Geotechnical Engineering Office of Hong Kong*

In the early morning of September 11th 1990, a debris flow occurred on the eastern flank of Tsing Shan. Tsing Shan is located about 2 km west to Tuen Mun. The summit rises to 583 meters. The debris flow path is about 1035 m long. On the summit and upper slope, grass is generally the only vegetation. On the sideslope, scrubby brushes and small trees occur locally in depressions and become larger and more extensive in the main valleys. As this area is not urbanized, nobody was injured and damage to property was negligible.

The debris flow has its origin at an elevation 404 meters a.s.l (Figure 24). The first part of the debris flow scar is aligned along a spur on the upper side slopes. In this part, a gully was eroded into loose bouldery colluvium. After 100 m the gully becomes a larger eroded depression in an area of thicker colluvium. Downslope, the scar descends into a drainage line where it widens and spreads high up until it narrows again at the constriction formed by the valley mouth.

At the valley mouth, a concrete water intake has been damaged. Beyond here the scar intersects the footslopes where the slope angle reduces and channelization ends.

3.3.1.2 *Geology of the area*

The summit and the upper part of the hillside are forms of fine grained granite. Downslope from the granite, there are some sedimentary and volcanic rocks of the Upper Jurassic. The sedimentary rocks are on the lower slope and contain sandstone, siltstone and mudstone with conglomerate. The volcanic rocks are on the footslope.

The debris flow scar is generally incised into deposits of colluvium. It starts on the granite upper slope, passes the sedimentary rocks and ends on the volcanic rocks at the footslope.

3.3.1.3 *A steep area dissected in gullies*

The summit and ridge tops are rounded. Below the upper ridge, the slope gradient is about 45° and the slope is dissected by a network of rocky gullies where ephemeral streams are found. Soils consist of boulder colluvium lining the gullies. Downslope from this upper area, the slope gradient decreases from 37° at the top to 20° at the footslope. The footslope of Tsing Shan has an overall slope of about 10° south-east towards the pre-development coastline.

The drainage line has a catchment of 114 000 m².

3.3.1.4 *No exceptional rainfall precipitation before the event*

Rainfall occurred in this area on the 11th of September. First a rainstorm started at 2.30 a.m. This event reaches its maximum intensity at 6.00 a.m. This storm is likely the trigger of the debris flow. Precipitation before the storm was about 50 mm in the previous 24 hours and 16 mm in the two days before that. At the start of the storm the hourly rainfall was 9.5 mm by 3.00 a.m. but then increases hourly to 23 mm, 34 mm and 50 mm. At 7.00 mm the rainstorm stopped. The total rainfall was 136 mm in 5 hours.

The return period of the maximum rainfall for periods of 5 minutes to 4 days before 7.00 a.m. on the 11th have been calculated. All rainfall has a return period of less than 2 years except for the 2 hour and 5 hour rainfall which have a return period of 2.5. This seems that this rainstorm was not exceptional for this site.

3.3.1.5 *Large erosion processes and deposition*

The debris flow involved the erosion and transportation of soil and rocks from the flanks of Tsing Shan and the deposition of these displaced material along the scar and at the footslope. A large amount of material has been eroded during the debris flow. Indeed the total volume of deposit material was about 20 000 m³ for an initial volume of 350 m³. When the flow passed through the drainage line, it increased its volume by 200 %. The erosion was not constant during the entire event. The erosion volume can be approximated as:

- Volume of trigger landslide: 350 m³ (in the depletion area)
- Volume of parent landslide: 2 500 m³ (in the depletion area)
- Spur erosion: 1 000 m³ (in the depletion area)
- Valley erosion: 8 000 m³ (in the depletion area)
- Erosion in deposition area 6 500 m³
- No erosion in the last part of the path (debris fan).

Figure 25 represents the divisions of the flow path according to erosion and deposition processes. In the first part of the stream, the depletion area, erosion processes were predominant (eroded volume of 12000m³) and only 880 m³ of debris were deposited. In the second part, the deposition area, the erosion was still important (6 500 m³ eroded) and the first lobes of debris appear. The volume of deposited debris in this part was about 13 000 m³. The debris flow path ends with debris fans, where no erosion was noticed and where huge amount of debris (7 000m³) was deposited in a small area. The debris constitutes the debris fans.

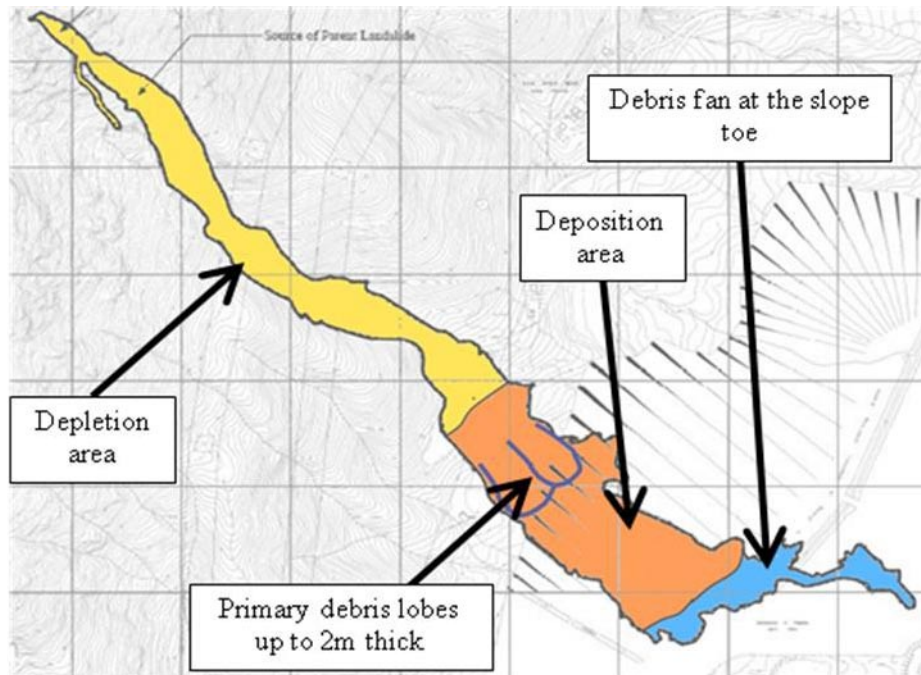


Figure 25. *The 1990 Tsing Shan debris flow: Erosion and deposition processes*

3.3.1.6 Probable sequence of events

First a small landslide with a volume of 350 m^3 was triggered on the spur. The debris from this landslide flowed down and entrained material. This material resulted in a large debris flow in the drainage line where more erosion took place. Several pulses of debris occurred due to the erosion in the drainage line.

3.3.2 Parameter of the calibration

The topography is provided by a digital elevation model which has been built on a Geographic Information System platform based on 1:1000 topographic maps and spot heights. It is uniformly at 5 m grid resolution. In this case the density of the mixture is 2000 kg/m^3 . The rheological model used is the frictional model. The parameters found to best fit the re-constructed even from 1990 were a basal friction angle of about 14° ($\tan \phi = 0.25$) and zero cohesion. Erosion processes are integrated to the simulation using the Hungr erosion law (c.f. chapter 4). The erosion coefficient (E_s) used is 0.0018. The following results have been obtained with this parameterization.

3.3.3 Results

The figures 26 and 27 show the results of the simulation:

In Figure 26, the field observations are represented by a red line and the model predictions are the blue area.



Figure 26. *The 1990 Tsing Shan debris flow: Model predictions versus Field observations*

The model provides a good match of the general extent in the real event and the distribution of the deposit after the simulation with the SPH depth integrated model. However the distribution of the deposit was better in the last example. Indeed in this study case, after the simulation, the debris is deposited a little bit at the north of the real deposition place. The model uses a constant bulk basal friction of 14° .

The erosion processes are successfully modeled because the final volume is about $20\,400\text{ m}^3$. In the real event the total deposition volume was about $20\,300\text{ m}^3$. More discussion about this results are given in the next chapter (chapter 4)

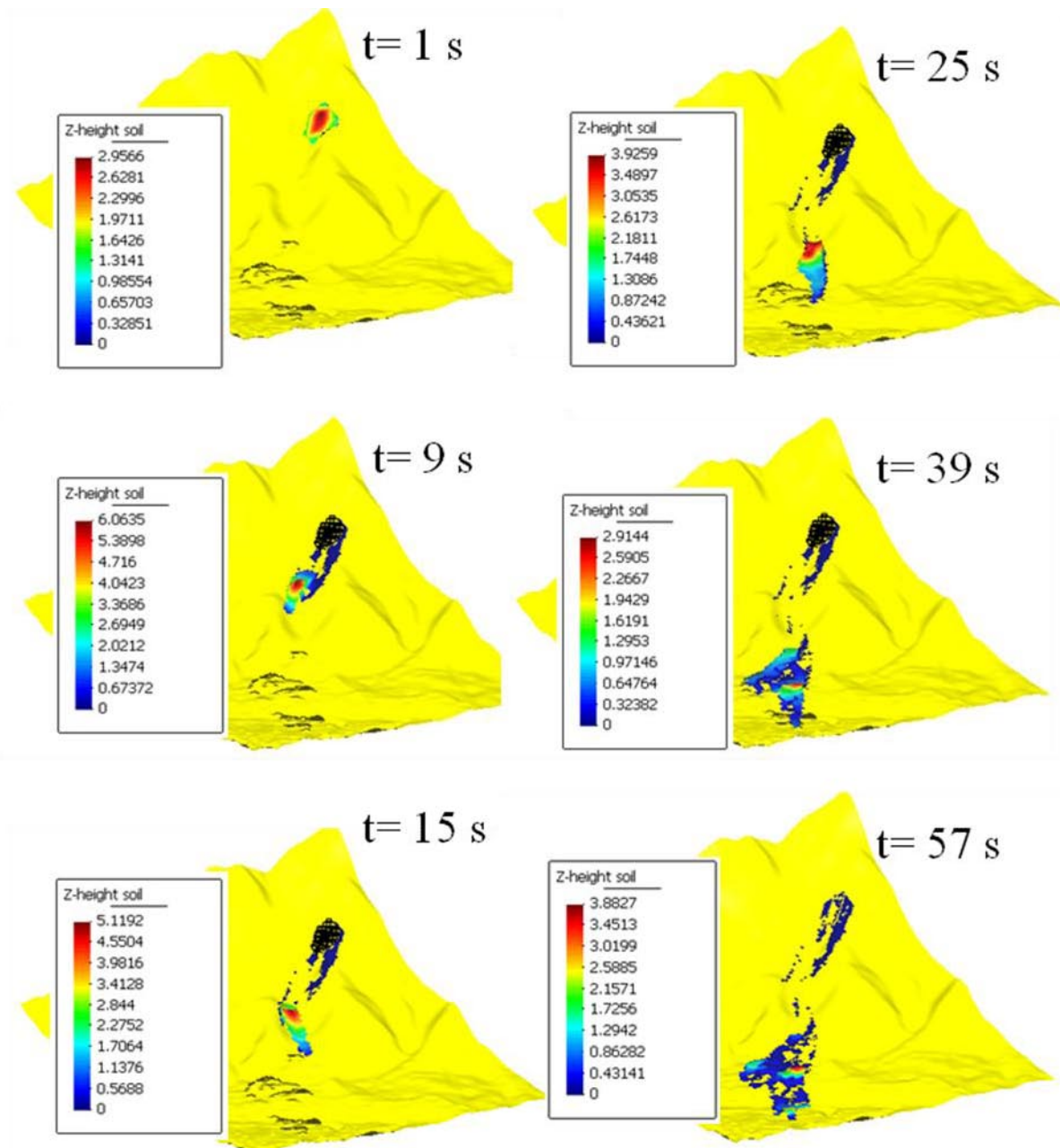


Figure 27. *The 1990 Tsing Shan debris flow: Model predictions - evolution of the debris flow*

The debris flow occurred during a short time, less than one minute. It is in agreement with the time duration of a debris flow, which is a rapid and transient phenomenon. After the simulation, the debris takes 57 seconds to flow down from the initiation area to the final deposition place (Figure 27). The debris flow path in the simulation is a little bit shorter than the one of the real event and is about 940 m long. In the simulation, the debris flow averaged velocity is 16.5 m/s. In the documentation, the

averaged velocity of the debris during the real event was estimated to 16.5 m/s using the equation of Johnson and Rodine (1984). The velocity of the flow in the simulation is exactly the same as the one in the real event. Therefore the SPH depth integrated model is able to find out the velocity of debris flows.

Figure 28 can be compared with the deposition got after the simulation.

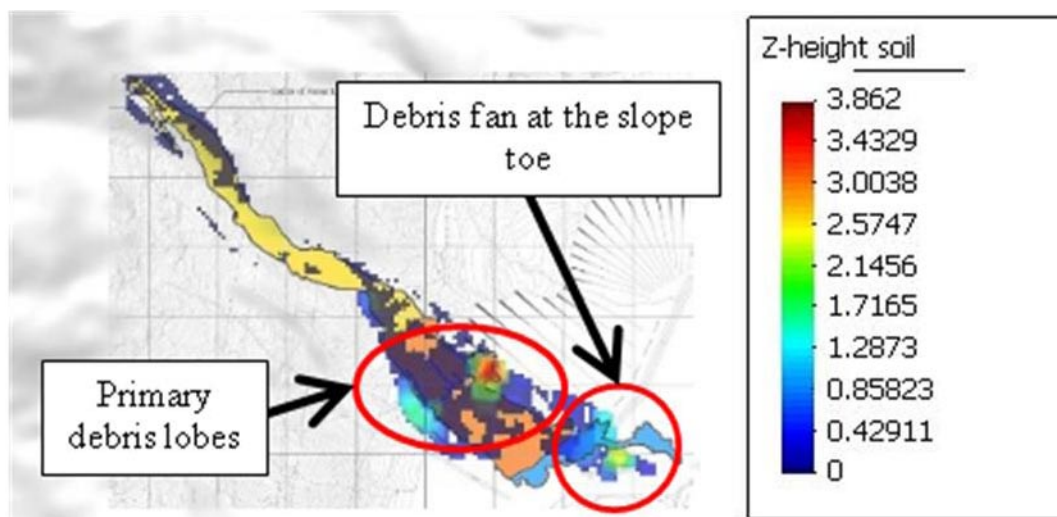


Figure 28. *The 1990 Tsing Shan debris flow: Deposition after Model predictions versus real deposition*

The last figure shows that the two main characteristics of the debris deposition appear in the results of the simulation. Indeed, after the simulation, the primary debris lobes and the debris fan at the slope toe are well situated. However the primary lobes are up to 4m height, which is higher than in the reality (up to 2m).

The results of this simulation seem to be really realistic. Indeed, the averaged velocity and the deposition area are more or less the same as during the real event. However, the deposition height, which is relevant in order to build protective structures, is not exactly the same as the one of the real event. This simulation used the Hungr law to model the erosion processes. This law allows to get the same final volume as the one of the real event. Thus the SPH depth integrated model is able to model debris flow including erosion processes. The next case study is a debris flow with erosion and presents a particularity in the shape of the flow.

3.4 The 2000 Tsing Shan Debris Flow, Hong Kong

3.4.1 Description of the event

3.4.1.1 Introduction

In the early morning of the 14th of April 2000, a debris flow occurred on the southeastern slopes of Tsing Shan area, about 200m southwest of the 1990 Tsing Shan debris flow. It originates at about 360 m on the rocky upper slopes and ended at about 70 m where the last bouldery debris was deposited (Figure 29). The total volume of debris was about 1 600 m³.



Figure 29. *The 2000 Tsing Shan debris flow: General view – Source: Hong-Kong Geotechnical Engineering Office*

The conditions (vegetation, geology and geomorphology) of Tsing Shan area have already been described in the last subsection. They consist of steep rocky upper slopes of granite and colluvium valleys at lower slopes. The lower slopes are formed of andesitic volcanic rocks, which are completely decomposed at the footslopes. The size of the subcatchments above the starting area is 6 400 m².

This debris flow is particular due to the division of the flow in two drainage lines.

3.4.1.2 No exceptional rainfall precipitation

The debris flow was reported to have occurred between 4.00 a.m. and 6.00 a.m. The debris flow appears to be related a rainstorm which started in the late evening on 13 April 2000. The peak of rainfall precipitation was recorded at 7.00 a.m. after that the debris flow occurred. The cumulative rainfall precipitation before the event was about 160 mm and about 350 mm when the rainstorm was over at 9.00 a.m. on 14 April. For all the durations from 5 minutes to 48 hours, the estimated return period for the rainfall preceding 5.00 a.m. is less than 2 years. Therefore this seems that the rainstorm was not exceptional for this site.

3.4.1.3 Landslide is the trigger of the debris flow

The initiation of the debris flow was due to a landslide which occurred at 360 m in a vegetated area of colluvial boulders on a slope at about 40°. The volume of this landslide was 150 m³. This area is close to the ridgeline where the drainage pattern is not so developed. However this area is situated at the narrow outlet of a subcatchment where groundwater and surface flows converge.

The causes of the initiation are the steep slope and the geology of the area. Indeed the colluvium, which forms a layer above the topsoil and bedrock, has a relatively high permeability compared to the layers underneath. Therefore the water can accumulate between the layers and form a partially confined aquifer and causes an increase of pore water pressure which simultaneously decreases the shear strength of the soil.

3.4.1.4 Particular shape of the debris flow

The landslide flowed down and transformed to a debris flow into an indistinct rocky gully where there is evidence of considerable erosion and little deposition. This gully ends at a planar to convex 30° slope. The upper part of debris flow scar descends to the China Light and Power (CLP) pylon at an elevation of 180 m. At this point the flow is divided into drainage lines, hereafter called north and south branch (Figure 30). More than 200 m³ was deposited at the pylon and formed an obstruction above the northern drainage line.

The northern drainage line is relatively straight and its upper slope gradient is about 50°. In the upper part of this drainage line, bedrocks are exposed and in the lower part, there are few colluvial deposits. The north branch appears to have a low likelihood of debris flow due to its small catchment and the general lack of colluvium from previous event. The southern drainage line has a more regular long profile than the northern drainage line. In this branch debris flows appear likely due to the large catchment and extensive colluvium deposit. Before the bifurcation, the debris was mixed with additional water, which enhanced the debris mobility.

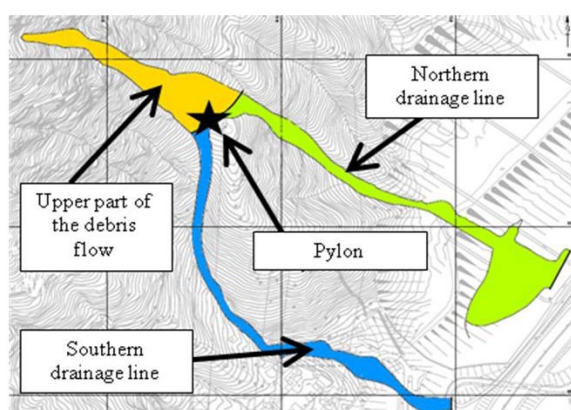


Figure 30. *The 2000 Tsing Shan debris flow: Bifurcation of the flow in two drainage lines*

3.4.1.5 Evolution of erosion and deposition processes during the flow

The volume of debris changed from 150 m³ (trigger landslide) to 1600 m³ (volume of deposits). The erosion took mainly place in the upper part of the flow, where 1010 m³ were eroded. In both branches, the erosion was lower, 295 m³ and 315 m³ respectively for the northern and southern drainage line. Little debris was deposited in the upper part of the channel, only 200 m³. Deposition was larger in the southern branch where 800 m³ were deposited and in the northern branch where about 600 m³ were deposited.

3.4.2 Parameters of the calibration

The topography is provided by a digital elevation model which has been built on a Geographic Information System platform based on 1:1000 topographic maps and spot heights. It is uniformly at 5m grid resolution. In this case study, the density of the mixture was 2000 kg/m³. The rheological model used to simulate this debris flow is the Voellmy fluid. The parameters found to best fit the re-constructed even from 2000 were a turbulence coefficient of 500 m/s², a friction angle of about 10° ($\tan \phi = 0.18$) and zero cohesion. The following results have been obtained with this parameterization.

3.4.3 Results and discussion

The figure 31 and 32 show the results of the simulation:

Figure 31, the field observations are represented by a red line and the model predictions are the blue area

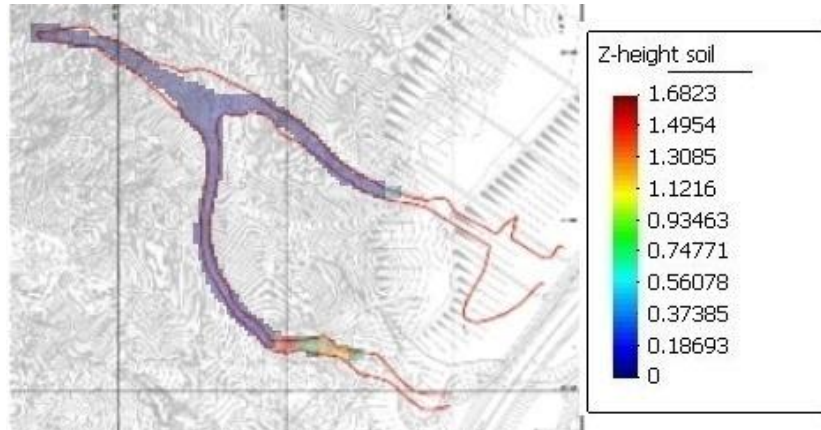


Figure 31. *The 2000 Tsing Shan debris flow: Model predictions versus Field observations*

The model provides a good match of the general extent in the real event and the distribution of the deposit after the simulation with the SPH depth integrated model. The main characteristic of this debris flow is represented in the results of the simulation, indeed in the simulation, the debris bifurcates exactly at the same place as in the real event. However the runout distance of the debris flow in the simulation is a little bit shorter than in the real event. In order to increase the runout distance, the internal friction angle should have been decreased. But the simulation with a smaller friction angle does not give the bifurcation of the flow in two branches. In the simulation the final deposit are located at the beginning of the slope decrease. In the real event, the debris flowed down until the end of the foothill.

As in the first case study, a Voellmy fluid has been chosen to model the event with a basal friction angle of about 10° and a turbulence coefficient of 500 m/s^2 . The low friction angle and the turbulent parameter are required to get the bifurcation in two drainage lines. Before the bifurcation, the debris has been mixed with water, which increased their mobility. In this case, the Voellmy fluid has been preferred to the frictional to model the resistance due to possible turbulence. The simulation with the frictional model is not able to get the bifurcation of the flow.

The erosion processes have been successfully modeled because the final volume is about $1\,580 \text{ m}^3$. In the real event the total deposition volume was about $1\,620 \text{ m}^3$. More discussion about this result are given in the next chapter (c.f. chapter 4).

Figure 32 shows the time duration of the simulation. The debris flow runs over the upper part faster than in the lower part. It takes 35 second to travel over this first part. After the bifurcation, the velocity slows down.

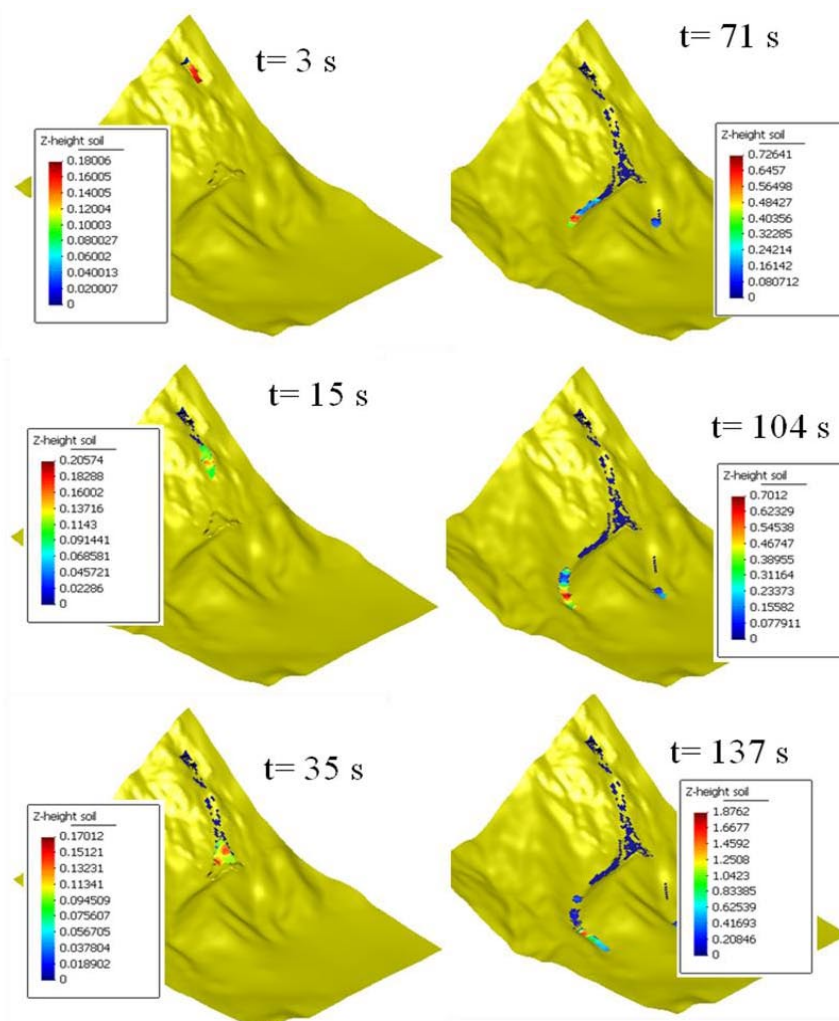


Figure 32. *The 2000 Tsing Shan debris flow: Model predictions - evolution of the debris flow*

Table 2. summarizes the different velocity along the path obtained in the simulation.

	Length of the section (m)	Time to travel over the section in the simulation (s)	Averaged velocity (m/s)
Upper part	300	35	8.6
Northern branch	288	69	4.2
Southern Branch	454	102	4.5
From the source to the end of the northern branch	588	104	5.7
From the source to the end of the Southern Branch	754	137	5.5

Table 2. *Flow velocities predicted by the simulation for the 2000 Tsing Shan debris flow*

The table shows a large difference between the velocities in the first part of the debris flow (upper part) and the one in the last part of the flow (drainage lines). The velocity of the real event was estimated by the team of J.P. King using a super-elevation at 14 m/s for the northern branch and 18 m/s for the southern branch. In the simulation, the velocity in the upper part was about 15 m/s. Therefore the velocities obtained by the simulation are really lower than the real one. Moreover after the bifurcation, the velocity is divided by a factor two. Therefore the velocities got after the simulation are really far from the real event. The reasons of this result can be that:

- In the real event, there was an input of water (surface runoff) at the bifurcation. In the simulation, water cannot be added during the simulation, therefore it is normal that the velocity is lower than in the real event.
- The change of slope gradient (from 38° for the upper part to 20° for the northern branch and 16° for the southern branch),
- The division of the total volume in two volume smaller,
- The planar slope at the bifurcation area (location of the pylon).

The velocities got after the simulation are not in accordance with the real event, and they are at the limit of the debris flow velocity range.

This case study has shown that it is possible to simulate some particular cases of debris flow. Moreover the Hungr law allows to get an increase of volume during the event due to erosion processes.

3.5 Conclusion

In this chapter the SPH depth integrated model has been applied to three case studies. In each case, the model provides a good match of the general extent of the debris. In the two first cases, the runout distance is the same as in the real event. Moreover in the second case, the velocity in the simulation is exactly the same as in the reality. The erosion processes have been integrated in the second and the third simulation in order to represent the increase of volume, which occurs during the event. The SPH depth integrated model has given the real final volume. In the third case, which is more complex due to the branching of the flow path, the flow velocity in the simulation is not the same as in the reality. However the values are still realistic.

Therefore these three back-analyses show that the SPH depth integrated model is able to predict the characteristics, which are relevant for debris flow risk analysis: runout distance, deposition pattern, flow velocity, flow path and final volume.

In the next chapter, the study focuses on the erosion processes and on the Hungr and Egashira erosion laws. This part of the study gives the application of the Egashira law to the 1990 and 2000 Tsing Shan debris flows, as well as a comparison of the results obtained with both erosion laws.

4 RESULTS – PART 2: COMPARISON BETWEEN TWO EROSION LAWS

4.1 Application of the Egashira law to the case studies

The SPH depth integrated model has been applied again to the 1990 and 2000 Tsing Shan debris flows using the Egashira law. In order to compare the results obtained with the Hungr law and the Egashira law, all the input parameters, which do not appear in the erosion subroutine, have the same value as during the precedent simulations (c.f. chapter 3).

4.1.1 The 1990 Tsing Shan Debris Flow, Hong Kong

In this simulation, the density of the mixture is $2\,000\text{ kg/m}^3$. The rheological model used is the frictional model. The parameters found to best fit the re-constructed even from 1990 were a basal friction angle of about 14° ($\tan\phi=0.25$) and zero cohesion. The erosion processes are modeled with the Egashira law with the parameters:

- The sediment concentration of the flow, $c = 0.58$
- The bed sediment concentration, $c_* = 0.67$
- The empirical constant, $K = 0.016$.

The figures 33 and 34 show the results.

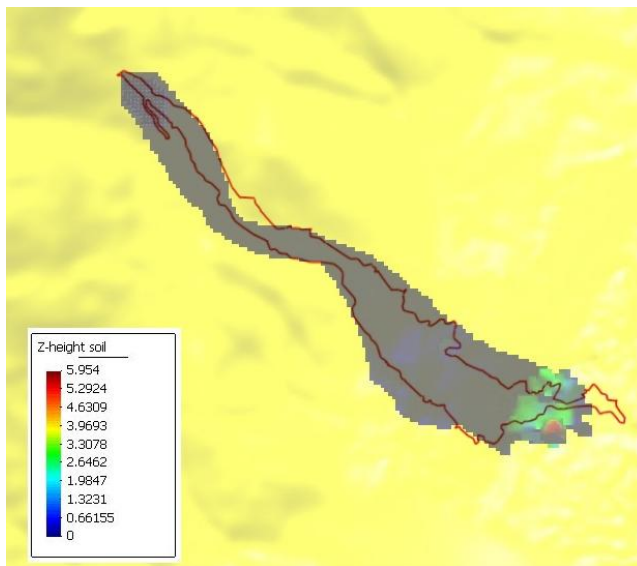


Figure 33. *The 1990 Tsing Shan debris flow: Model predictions versus Field observations*

The deposition pattern is the same as in the simulation with the Hungr erosion law. However, in the northern part of the deposition, the extension of the debris is a little bit larger and therefore closer to the real event. The erosion processes have been successfully modeled because the final volume is about $20\,310\text{ m}^3$.

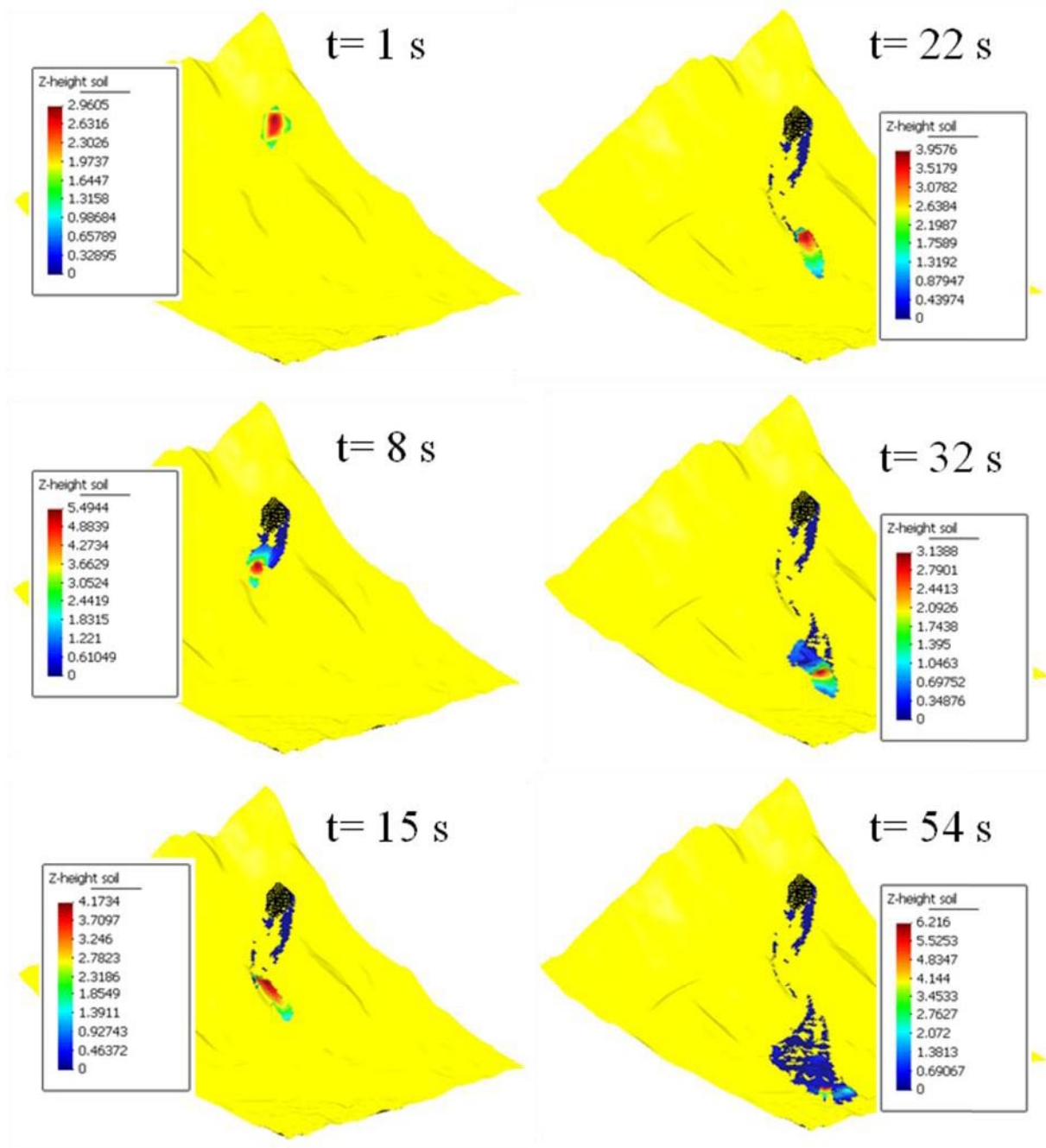


Figure 34. *The 1990 Tsing Shan debris flow: Model predictions – evolution of the event*

The duration is a bit shorter than in the simulation of chapter 3 but it is still in accordance with the duration of the real event. In the simulation, the debris takes 54 seconds to flow down from the initiation area to the final deposition area (Figure 34). The runout distance is 940 m (the same as in the simulation with the Hungr law). The velocity of the flow is about 17.4 m/s. It is higher than in the first simulation but still in agreement with the real event, where the velocity was about 16.5 m/s.

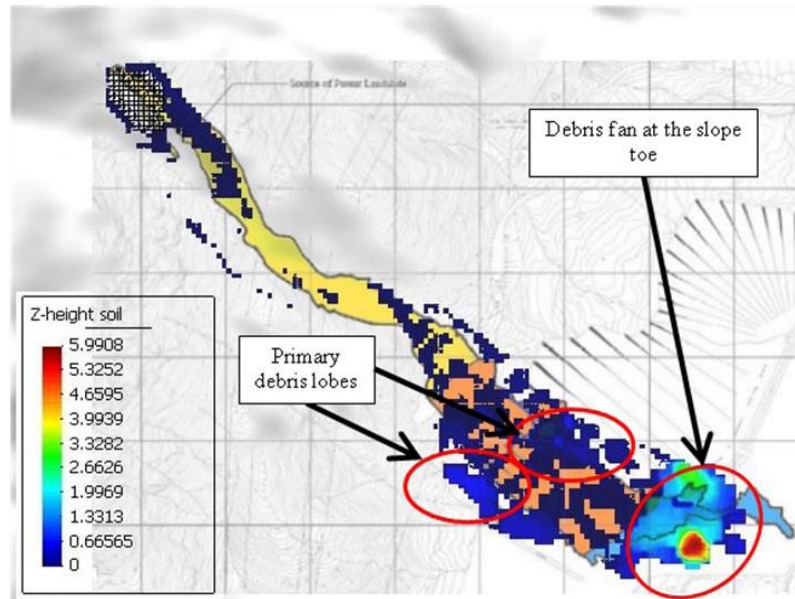


Figure 35. *The 1990 Tsing Shan debris flow: Deposition after Model predictions versus real deposition*

Figure 35 shows the deposition pattern in details. The primary lobes are well represented and the height of these lobes (from 1.3 m to 1.9m) is in agreement with the height after the real event (2m). Therefore the result of the modified simulation is better than the result of the first simulation with the Hungr erosion law, where the height of the primary lobes was about 4m. In the last figure, the debris fan at the slope toe can also be observed.

This first case shows that the SPH depth integrated model can also model debris flows where erosion processes are significant by using the Egashira erosion law. Employing the Egashira law the results (the height of the deposition lobes) could be improve considerably compared to using the Hungr law.

4.1.2 *The 2000 Tsing Shan Debris Flow, Hong Kong*

In this simulation, the density of the mixture was $2\,000\text{ kg/m}^3$. The rheological model used to simulate this debris flow is the Voellmy fluid. The parameters found to best fit the re-constructed even from 2000 were a turbulence coefficient of $500\text{ m}^2/\text{s}^2$, a friction angle of about 10° ($\tan\phi=0.18$) and zero cohesion. The following results have been obtained with this parameterization. The erosion processes are modeled with the Egashira law with the parameters:

- The sediment concentration of the flow, $c = 0.62$
- The bed sediment concentration, $c_* = 0.71$
- The empirical constant, $K = 0.011$.

The figures 36 and 37 show the results.

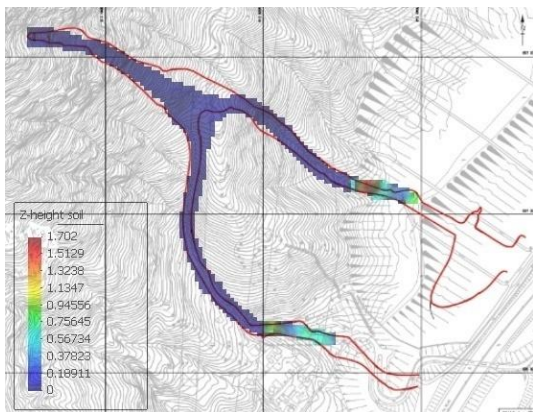


Figure 36. *The 2000 Tsing Shan debris flow: Model predictions versus field observations*

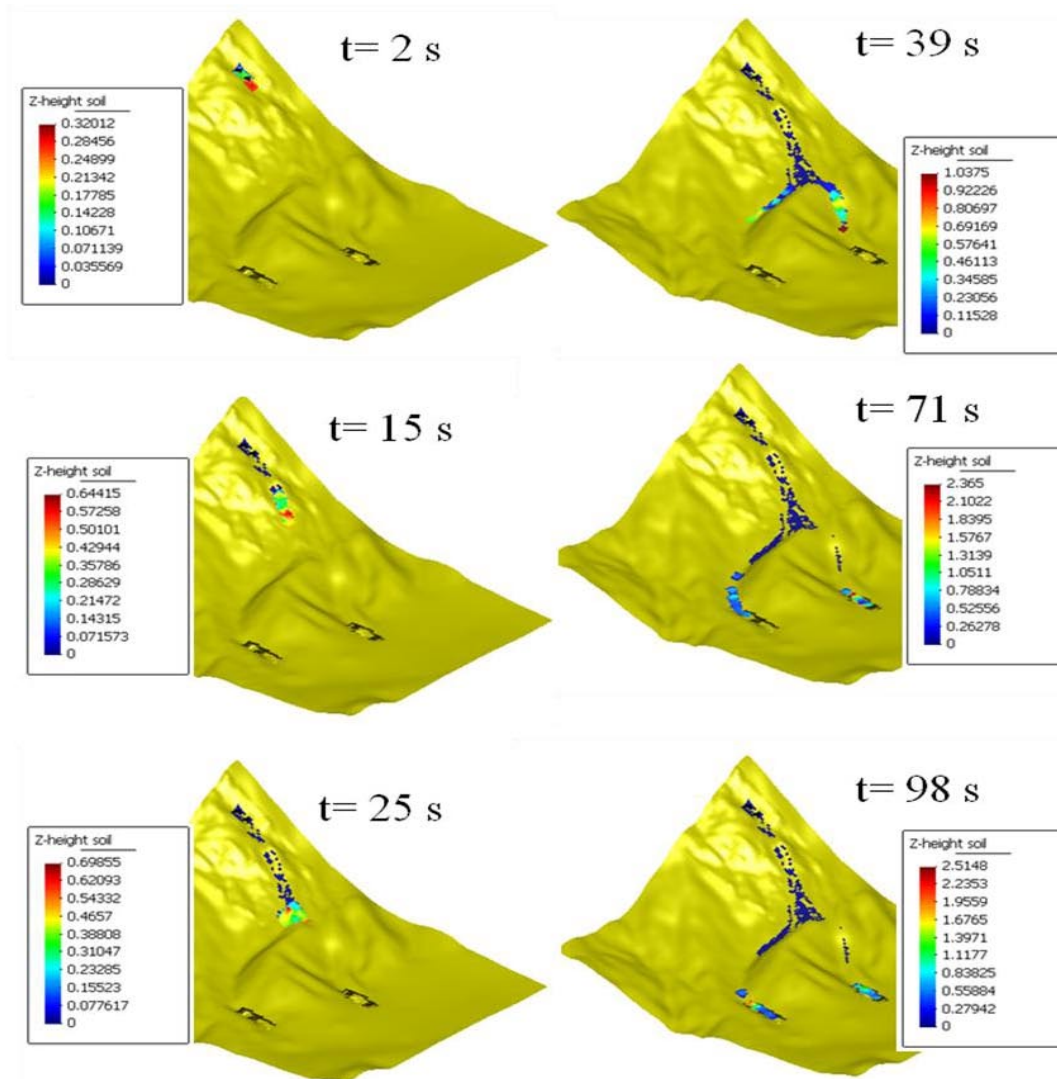


Figure 37. *The 2000 Tsing Shan debris flow Model predictions - evolution of the event*

Like in the simulation with the Hungr law, the runout distance is shorter than in the real event (Figure 36). However the model provides a good match of the general extent and the distribution of the deposit. The erosion processes have been successfully modeled because the final volume is about $1\,595\text{ m}^3$ and is close to the final volume in the real event (about $1\,600\text{ m}^3$).

The time duration of the event in this simulation is shorter than the one of the simulation in chapter 3 (Figure 37). Therefore the flow velocities are larger and more realistic. Table 3 describes these velocities. In the upper part, the velocity is really close to the reality. Indeed the model predicts a velocity of 12 m/s and in the reality the velocity was estimated at 15 m/s . After the bifurcation, the velocity decreases again but it is still high and therefore more realistic for a debris flow than calculated in the simulation with the Hungr erosion law.

	Length of the section (m)	Time to travel over the section in the simulation (s)	Averaged velocity (m/s)
Upper part	300	25	12
Northern branch	340	46	7.4
Southern Branch	415	73	5.6
From the source to the end of the northern branch	640	71	9.0
From the source to the end of the Southern Branch	715	98	7.3

Table 3. *Flow velocities predicted by the simulation for the 2000 Tsing Shan debris flow*

The first conclusion about the implementation of the Egashira law is that the model has the same ability to predict the deposition pattern, but it seems to be more efficient to predict the flow velocity.

4.2 Comparison of results after Hungr and Egashira law

In order to conclude which of the proposed laws are more efficient, some magnitudes relating to erosion processes have to be introduced. First of all the linear erosion rate, E_l , corresponds to eroded volume (in cubic meter) per meter travelled:

$$E_l = \frac{\text{Volume eroded over a subsection } i}{\text{length of the subsection } i} \quad (m^3 / m) \quad (4.1)$$

The next magnitude is the volume increase rate, ΔV , which is defined by the following expression:

$$\Delta V = 100 \times \frac{V_t - V_i}{V_f - V_i} \quad (4.2)$$

where:

- V_t is the volume at the time t ,
- V_i is the initial volume of the debris flow, and
- V_f is the final volume of the debris flow.

The last magnitude is the relative traveled distance, ΔL , which is defined as follow:

$$\Delta L = 100 \times \frac{\text{travelled distance}}{\text{total runout distance}} \quad (4.3)$$

In the following subsection, the variations of these magnitudes are presented in chart representations for both case studies of the Tsing Shan debris flows.

4.2.1 The 1990 Tsing Shan debris flow

First the linear erosion rate of both simulations, using the Egashira law the Hungr law, has been compared to field observations carried out after the event. However, the initial volume in the real event was about 350 m³ and in the data used for the simulation (given by the Hong Kong Geotechnical Engineering Office) the volume of the started area is about 7150 m³. The final volumes are similar in the real event and in the both simulation and therefore the linear erosion rate simulated and in the

nature cannot be of same order. However their variations can be compared in order to see if they have the same trend. The variation of the erosion rates is shown in Figure 38.

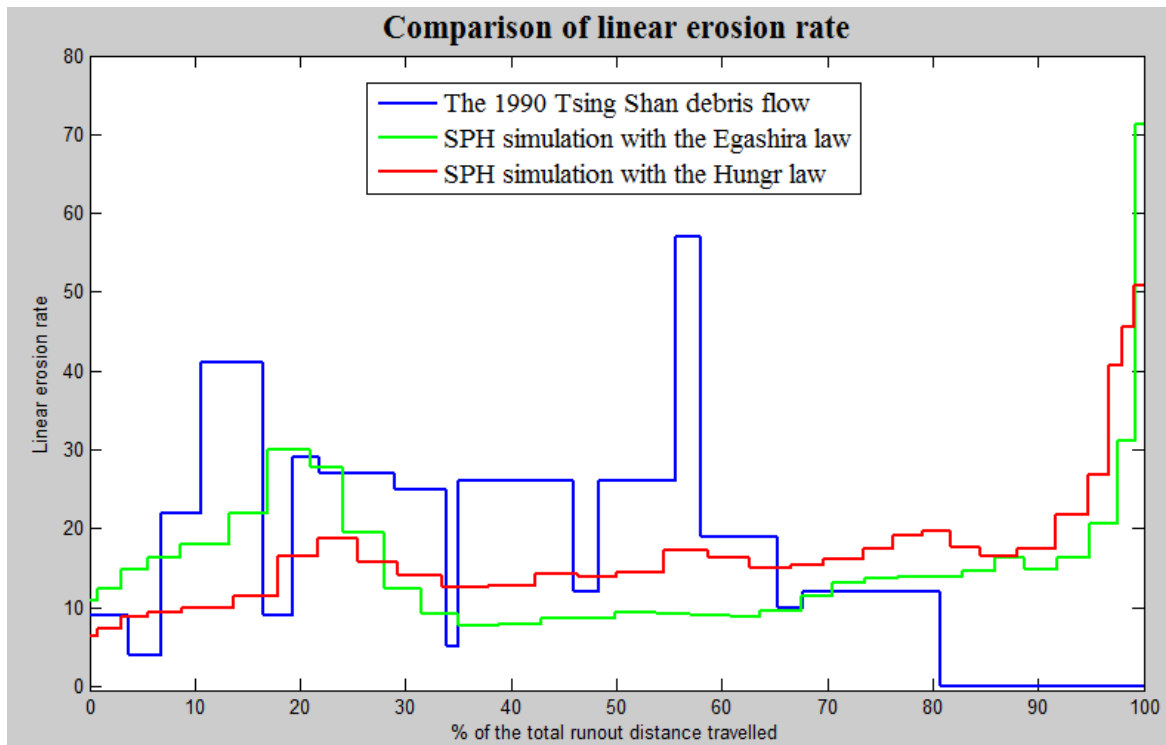


Figure 38. *Comparison of the linear erosion rate obtained during the 1990 Tsing Shan debris flow and those calculated by the simulations*

During the real event, the linear erosion rate is equal to $0 \text{ m}^3/\text{m}$ in the last part of the flow path (from 80 % to 100% of the travelled distance). Indeed, at the end of the flow path, the debris is deposited. This area corresponds to the deposition area. In both simulations the linear erosion rates in the both simulations reach their highest values in this region, which is not realistic, because debris flows normally do not erode in the deposition area.

In the first part of the flow path, the linear erosion rate of the real event varies unsteadily, when the variation of the linear erosion rate in both simulations is more or less constant.

The value of the linear erosion rate cannot be directly compared, but the increase of volume along the path can be compared and they are represented Figure 39.

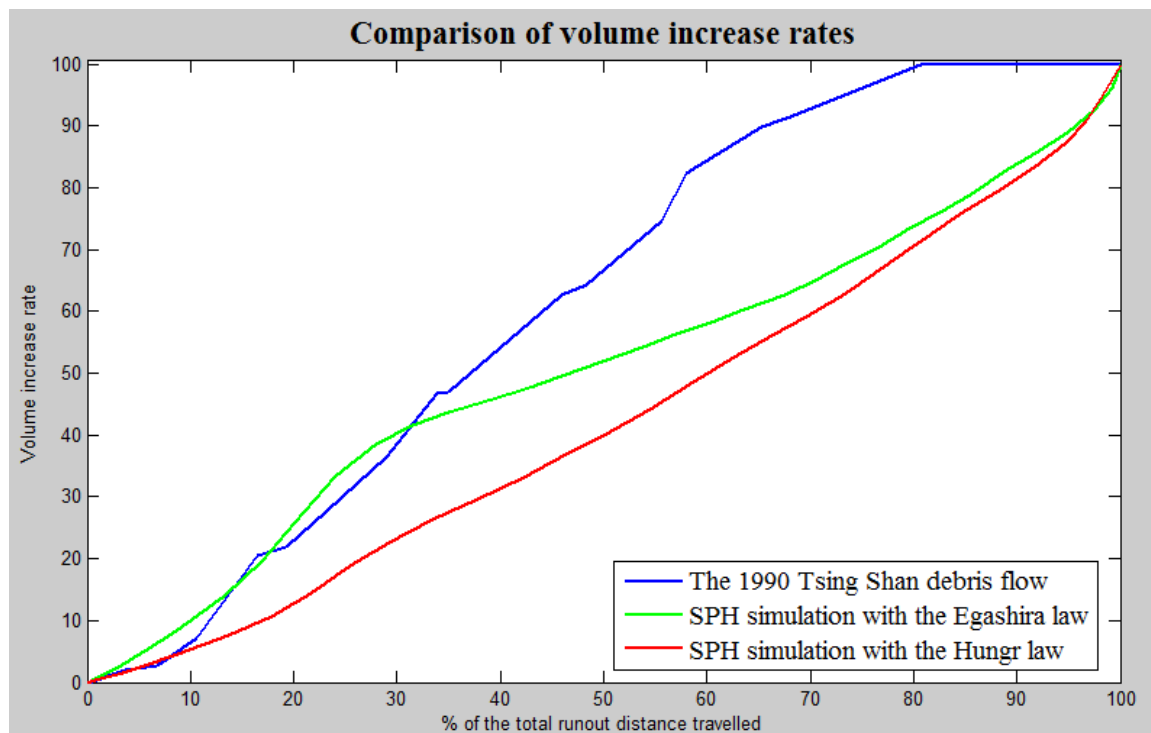


Figure 39. Comparison of the volume increase rate of the 1990 Tsing Shan debris flow and those calculated by the simulations

The volume of debris increases faster in the real event than in the simulation. It can be explained by the fact that all erosion processes take place along the entire path in the simulation. In the first part of the flow path, the curve representing the simulation with the Egashira law is closer to the curve representing the increase volume of the Tsing Shan debris flow than the one representing the simulation with the Hungr law. Therefore, in this case study the Egashira law is more adapted than the Hungr law. However the results are not good enough to conclude the Egashira law is better than the Hungr law.

4.2.2 The 2000 Tsing Shan debris flow

In this subsection, the same type of graphics as in the preceding subsection is interpreted for the upper, northern and the southern part of the 2000 Tsing Shan debris flow. For the same reasons as in the last example, the value of the linear erosion rate in the real event cannot be compared to the one of both simulations.

First the results of the upper part of the flow (before the bifurcation) can be observed. During the event, the linear erosion rate decreased along the path until reaching the bifurcation point. In the simulation, the contrary can be observed. Indeed the linear erosion rates increase. Erosion processes are thus inversely modeled (Figure 40).

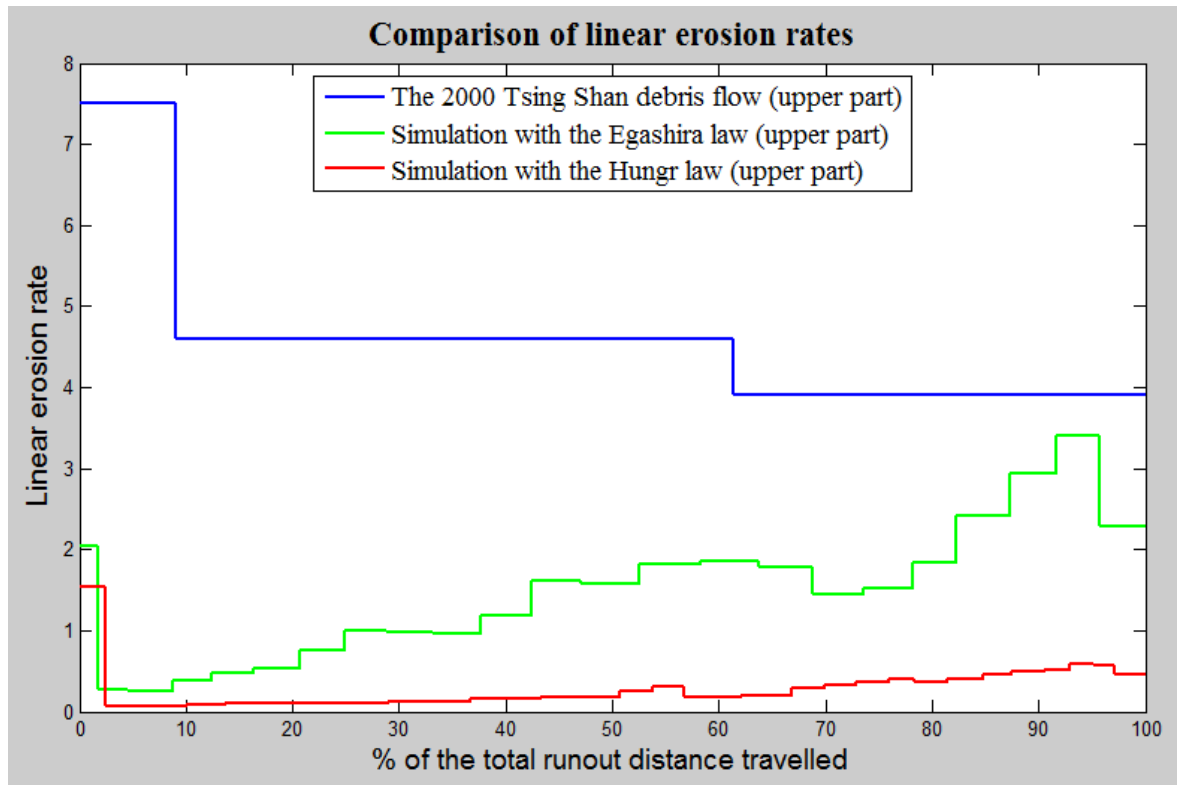


Figure 40. *Comparison of the linear erosion rate obtained during the 2000 Tsing Shan debris flow (upper part) and those calculated by the simulations*

The following charts (Figure 41 and 42) represent the increase volume rate in the northern and southern part of the debris flow. Here a significant difference between the Hungr and the Egashira law can be observed. Indeed, in the northern path, during the real event and the simulation with the Egashira law, at 70 % of the total runout distance travelled, the volume is equal to more than 95 % of the final volume. On another hand, in the simulation with Hungr, at the same location, the volume represents only 70 % of the final volume (Figure 41).

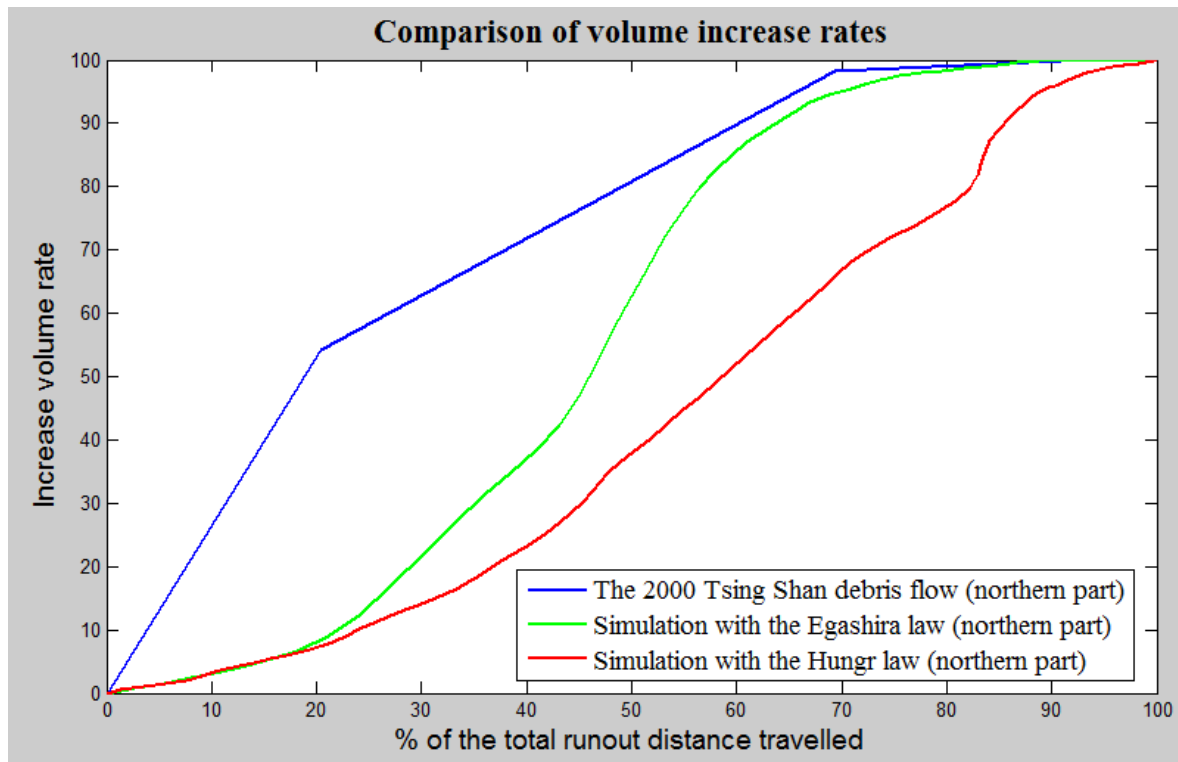


Figure 41. Comparison of the volume increase rate of the 2000 Tsing Shan debris flow (northern branch) and those calculated by the simulations

The same results are observed in the southern branch of the flow. At 80 % of the total runout distance traveled, the volume in the real event and in the simulation with the Egashira law represents more than 97 % of the final volume. In the simulation with the Hungr law, at this point, the volume corresponds only to 80 % of the final volume (Figure 42).

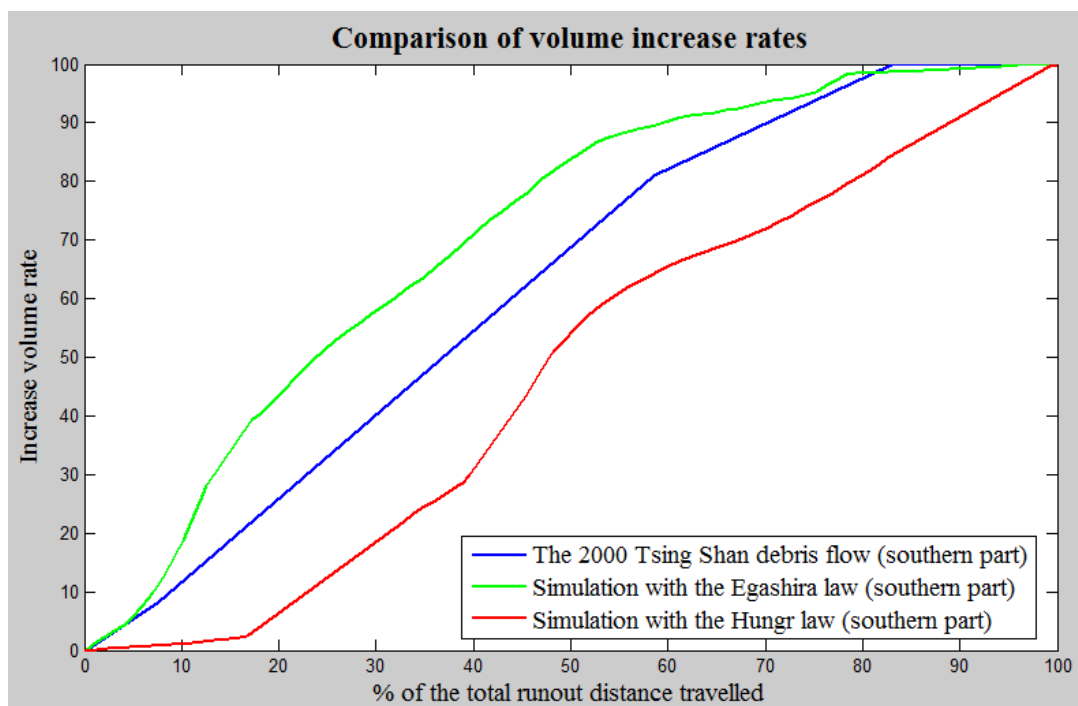


Figure 42. Comparison of the volume increase rate of the 2000 Tsing Shan debris flow (southern branch) and those calculated by the simulations

These results are interesting and show that the Egashira law is more adapted than the Hungr law to represent the stopping process of debris flow, where no erosion takes place. These results can be confirmed with the Figure 43 representing the variation of linear erosion rate in the southern branch.

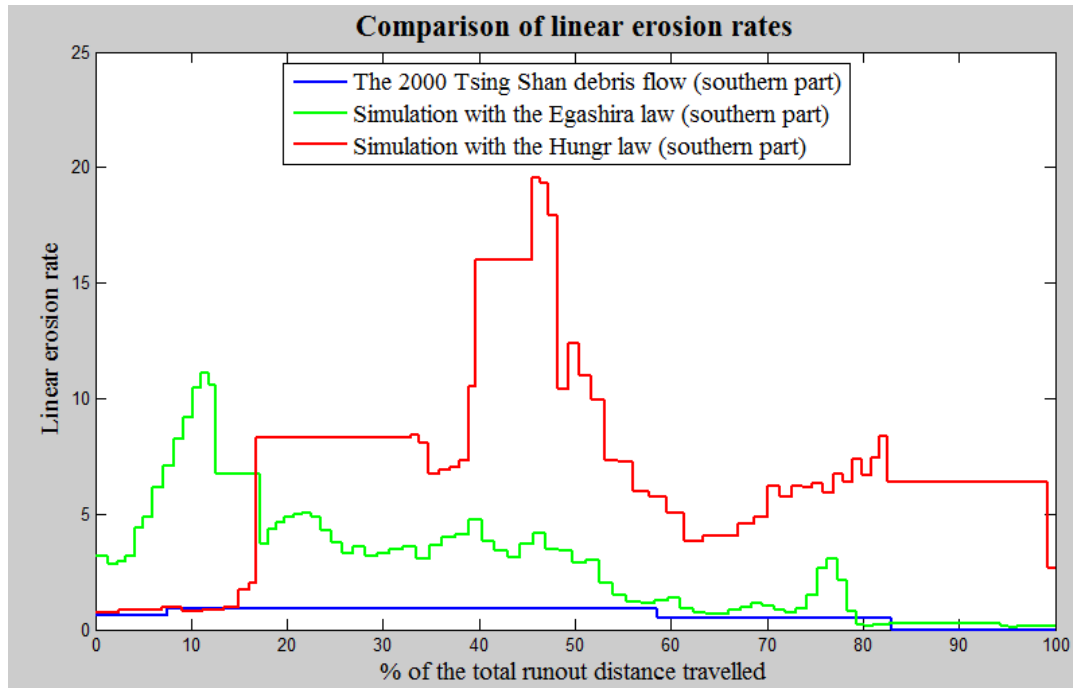


Figure 43. Comparison of the linear erosion rate obtained during the 2000 Tsing Shan debris flow (southern part) and those calculated by the simulations

Here the variations of the linear erosion rate are quite similar between the simulation with the Egashira law and the real event. The linear erosion rate increases until 10 % of the total runout distance traveled and after that it decreases slowly until the end. In the last part of the flow (from 80 % to the end of the flow path), the low linear erosion rate in the simulation with the Egashira law and in the real event justify the volume increase rates presented in the preceding chart. On another hand, in the simulation with the Hungr law, on this same part of the flow, the linear erosion rate has a quite high value and therefore it explains that the volume increases along the entire flow path.

4.3 Conclusion

This chapter has shown mixed results concerned the Egashira erosion law. Indeed, the Egashira erosion law improves some characteristics of debris flows: flow velocity, debris deposition pattern (height of debris lobes). However, the results concerning the erosion rate and the increase volume are quite similar to those got with the Hungr erosion law. Indeed, with both erosion laws, the volume of debris increases not exactly as in real event and the erosion rate does not vary exactly as in reality. However in the last test case using the Egashira erosion law, the volume does not increase at the end of the flow path, area where no erosion processes take place.

Finally this work has shown that erosion processes seems to be strongly dependent on the channel slope. Therefore it could be interesting to try a new erosion law composed of the parameters found important by evaluating the erosion laws of Egashira and Hungr. The proposed new law would have the following form:

$$e_r = K \times v \times h \times (\tan \theta)^{2.5} \quad (4.4)$$

where:

- K is an empirical parameter
- θ is the slope
- v is the flow velocity
- h is the flow depth.

This type of law would allow calculating erosion rates taking into account the slope as well as the others magnitudes (the flow velocity and flow depth). This law should be tested in laboratory and in the SPH depth integrated model before to be validated.

The proposed erosion law has been applied to the 1990 and 2000 Tsing Shan debris flows. Hereafter, the results derived with this erosion law are presented.

In the simulation of the 1990 Tsing Shan debris flow with the proposed erosion law, the density of the mixture is $2\,000\text{ kg/m}^3$. The rheological model used is the frictional model with a friction angle of about 14° ($\tan\phi = 0.25$) and zero cohesion. The erosion processes are modeled with an empirical constant, K , equal to 0.01. The simulation gives similar results for the deposition pattern, debris volume and flow velocity as in the simulation with the Egashira law. However the results concerning the erosion processes are different. Figure 44 shows the volume increase rates obtained with the different simulations.

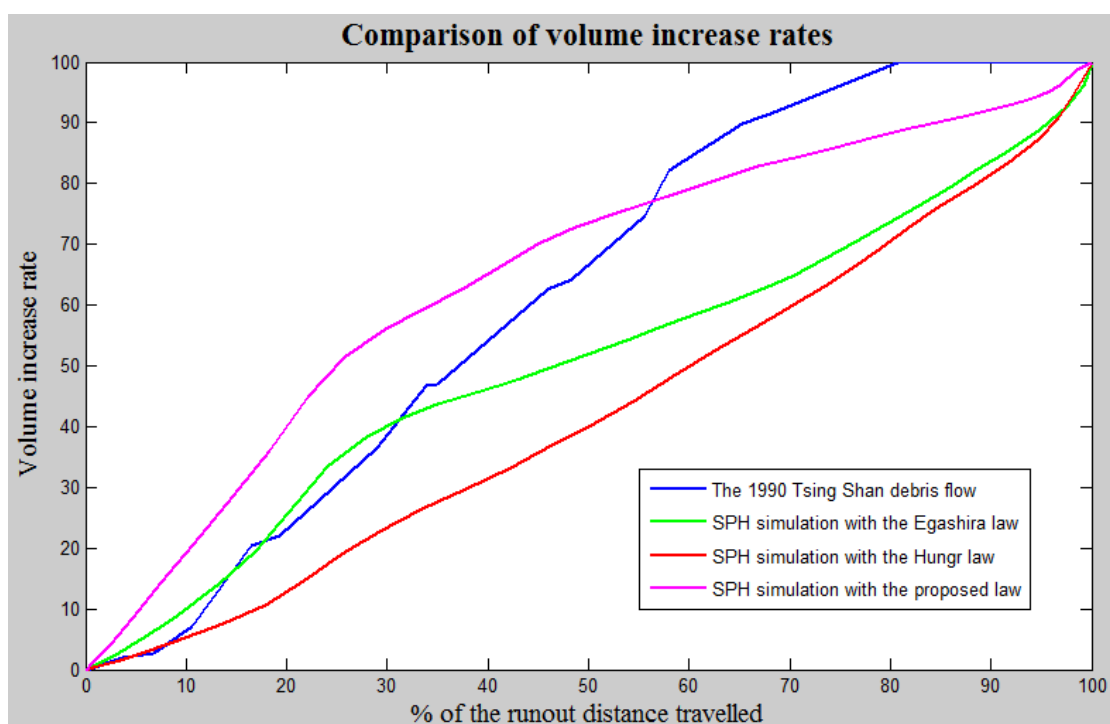


Figure 44. Comparison of the volume increase rate of the 1990 Tsing Shan debris flow and those calculated by the simulations (with the proposed erosion law)

In this chart, the curve representing the variation of the volume increase rate in the simulation with the proposed erosion law is more realistic than in the other simulations. Indeed the volume increases faster in the first part of the travelled path and slower in the last part. Therefore in the deposition area, less material is eroded and more is deposited which correspond well with observations carried out after the event.

In the simulation of the 2000 Tsing Shan debris flow with the proposed erosion law, the density of the mixture is $2\,000\text{ kg/m}^3$. The rheological model used is the Voellmy model with a friction angle of about 10° ($\tan\phi = 0.18$) and a turbulent coefficient of 500 m/s^2 . The erosion processes are modeled with an empirical constant, K , equal to 0.033. Like in the case study earlier, the simulation gives similar results for the deposition pattern, debris volume and flow velocity as in the simulation with the Egashira law. However the results concerning the erosion processes are different. Figure 45 shows the volume increase rates obtained with the different simulations.

First, in the northern branch of the flow, the results of the proposed law are good. In fact, the volume increases in the same manner than during the real debris flow. It increases rapidly to reach its maximum when the flow has travelled over 70 % of the total distance travelled. In the last 30 % of the travel, no material is eroded and only deposition processes occurs (Figure 45).

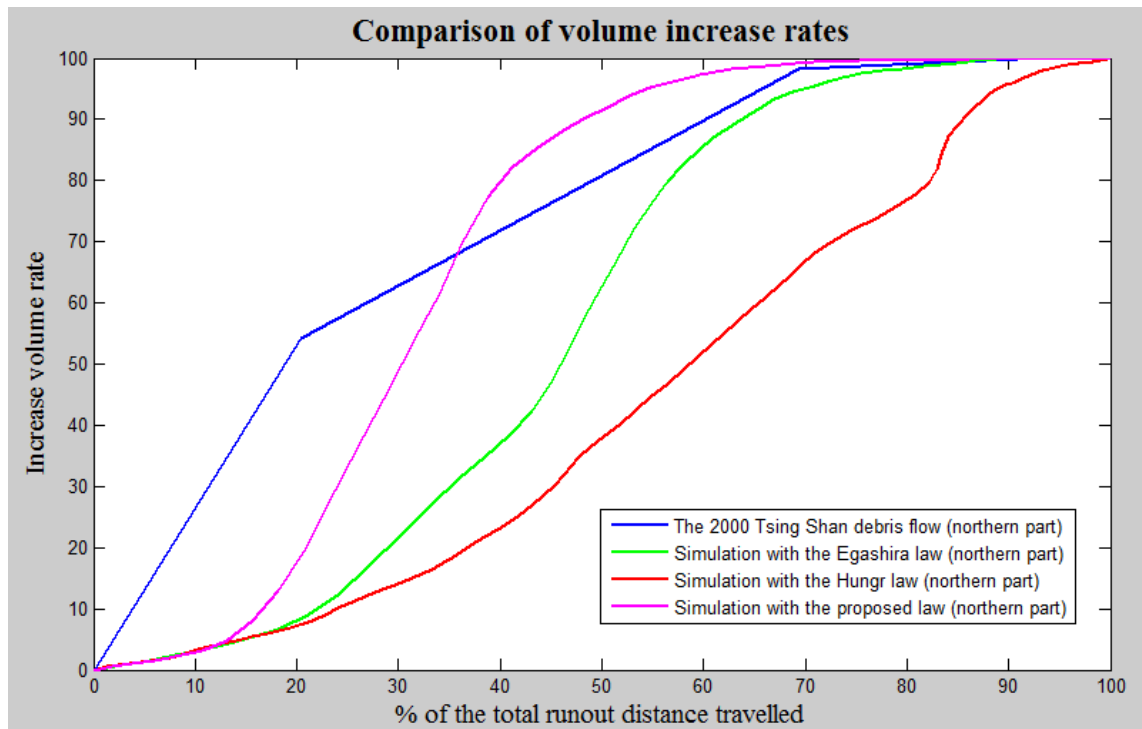


Figure 45. Comparison of the volume increase rate of the 2000 Tsing Shan debris flow (northern branch) and those calculated by the simulations (with the proposed erosion law)

In the southern branch, the results are not so conclusive. The results using the proposed law are really similar to those got with the Egashira law. Both of these results are more realistic than those got with the Hungr law (figure 46).

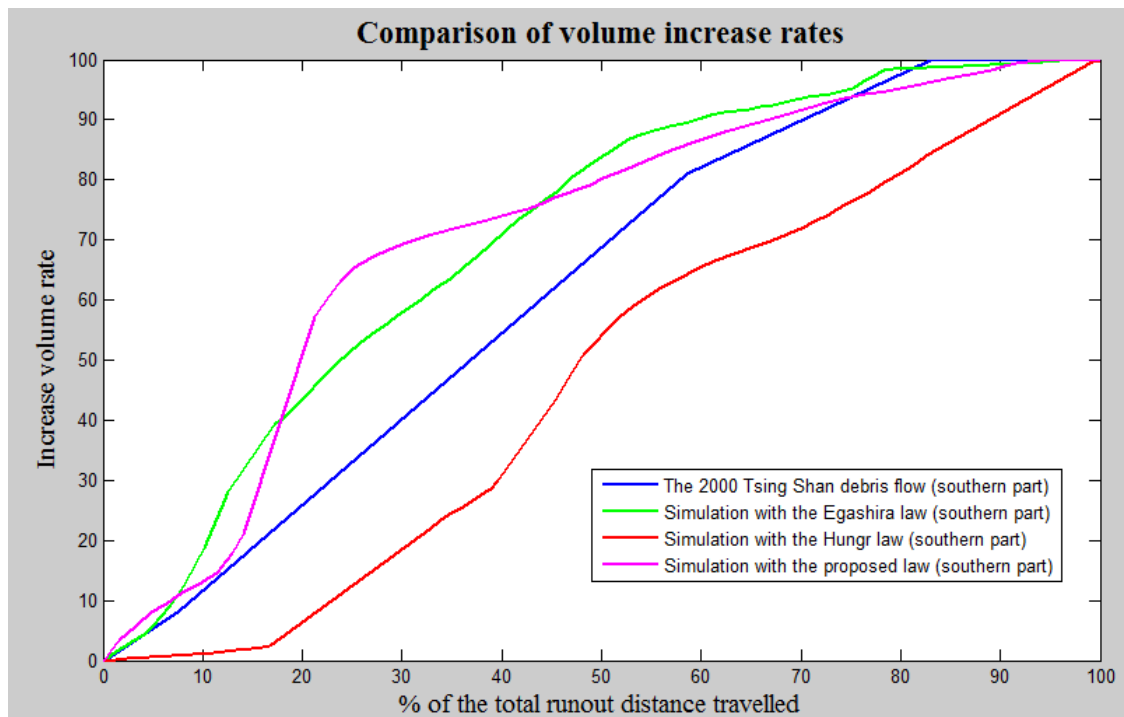


Figure 46. Comparison of the volume increase rate of the 2000 Tsing Shan debris flow (southern branch) and those calculated by the simulations (with the proposed erosion law)

The erosion proposed law has been integrated to the SPH depth integrated model and gives more realistic results, for the two case studies, which are more realistic than those got with the other

erosion laws. However this law has been proposed after the analysis of the results got for the presented case studies and has not been tested in laboratory experiments. The empirical parameter, K , has to be calibrated. The exponent of $\tan \theta$ has also to be calibrated. Indeed higher this exponent is, the more the erosion process depends on the slope.

To conclude, this law is only a proposition in order to reinforce the influence of the slope on erosion processes. Works on this law may constitute future research line for the SPH depth integrated model.

5 DISCUSSIONS

5.1 Discussion on the results of part 1

Chapter 3 shows that the SPH depth integrated model is able to simulate real debris flow events. In the three test cases, the deposition got after the simulation match well the deposition observed in the field after that the debris flows occurred. To know where the deposition takes place and the debris flow runout distance are really important to assess the risk in an area susceptible to such phenomena.

However, all the results got after the simulation are not always in agreement with real events. For the example, after the three cases, it seems hard to forecast the exact velocity and the exact deposition height. These magnitudes are useful to calculate pressure of debris flow and therefore useful for calculations to plan mitigation measures (like check dams, reservoirs...).

The results obtained show the difference between the frictional model and the Voellmy model. In fact, the Voellmy model will be preferred in case that the debris flow has a large amount of water. Therefore it is also preferable to use this model in case of mudflow. On another hand, the frictional model is preferred for flows with drier granular behavior.

The simulation of these three case studies points out some conclusions with regards to the calibration work of a model. First of all, three case studies are not enough to create a database of calibrated parameters. The values got for each case study can be compared with values results got by McDougall (1998), who modeled debris flows, rock avalanches, and rock/ice avalanches using the DAN3D model. This model is similar to the SPH depth integrated model. Indeed it uses the same rheological constitutive equations, either the Voellmy model or the frictional model. The erosion processes are integrated in the simulation using the Hungr law and the numerical model used is the SPH. As the DAN3D model uses the same rheological models, it is useful to compare the values for the input parameters of these models. Results are displayed in the Figure 47:

Remarks: The parameters f , used in the Voellmy model, is the basal friction coefficient and corresponds to the parameter $\tan \phi_b$.

In case of the frictional model, the parameter values for ϕ_b chosen by McDougall, are larger than the one chosen for the SPH. McDougall chose an angle of friction of about 30° and in our case study number 2 the friction angle was 16° . However the values for the parameters of the Voellmy model are of the same order. The parameter $\tan \phi_b$ has a quite low value of about 0.1 in the McDougall cases and between 0.18 and 0.29 in our case studies. After the case studies of McDougall, the turbulent coefficient ranges from 200 to 1000 m/s^2 and in our cases from 500 to 1000 m/s^2 . The values for the erosion coefficient E_s are of the same order in both studies.

Both of the different case studies and the values given by McDougall show the large variation of parameter ranges. In consequence, it is difficult to find a unique value for these parameters. Moreover the values of the parameters do not depend only on the environmental conditions, where the debris flow takes place. Although the 1990 and the 2000 Tsing Shan debris flows were compound of the same soil and took place in the same area and the calibration for one case is not valid for the other one. Therefore the calibration of the parameter depends not only on the area condition (vegetation, geology and geomorphology) but also on the condition of debris flow (influence of the fine topography, rainfall condition, soil/water mixture properties).

Case Study	Landslide Type	N	B	C	D	ϕ_i (°)	Basal Rheology and Parameters		E_e (m ⁻¹)
							Before Entrainment	After Entrainment	
Frank	rock avalanche	2000	4	0	200	40	frictional $\phi_b=14^\circ$	no change	0
Val Pola	rock avalanche	4000	6	0.01	200	35	frictional $\phi_b=16^\circ$	no change	0
Cervinara	debris avalanche/ flow	2000	4	0	200	35	frictional $\phi_b=30^\circ$	Voellmy $f=0.07$ $\xi=200 \text{ m/s}^2$	0.01
Quindici	debris avalanche/ flow	2000	4	0	200	35	frictional $\phi_b=30^\circ$	Voellmy $f=0.07$ $\xi=200 \text{ m/s}^2$	0.01
Nomash River	rock slide – debris avalanche	2000	4	0	200	35	frictional $\phi_b=30^\circ$	Voellmy $f=0.05$ $\xi=400 \text{ m/s}^2$	1.9×10^{-3}
Zymoetz River	rock slide – debris flow	4000	4	0.01	200	35	frictional $\phi_b=31^\circ$	Voellmy $f=0.1$ $\xi=1000 \text{ m/s}^2$	3.3×10^{-4}
McAuley Creek	rock avalanche	4000	4	0.01	200	35	frictional $\phi_b=30^\circ$	Voellmy $f=0.1$ $\xi=500 \text{ m/s}^2$	0
Kolka	ice/rock avalanche	4000	4	0.01	200	20	Voellmy $f=0.05$ $\xi=1000 \text{ m/s}^2$	no change	0

Parameter values used in each case study. N is the number of particles, B is the particle smoothing coefficient, C is the velocity smoothing coefficient, D is the stiffness coefficient, ϕ_i is the internal friction angle, ϕ_b is the bulk basal friction angle (for frictional basal resistance), f is the basal friction coefficient (for Voellmy basal resistance), ξ is the turbulence parameter (for Voellmy basal resistance) and E_e is the entrainment growth rate within a specified entrainment zone.

Figure 47. Parameter used by McDougall in various case studies – Source: Thesis of McDougall

Finally, as it was mentioned before, it is important to keep in mind that, after these case studies there are still uncertainties in the calibration of the model. These uncertainties have to be left out in order to have a calibrated model, i.e. tables giving, for each parameter, all the potential values according to the conditions of the event. These tables are required to forecast debris flows which could occur in mountain area. These uncertainties can be left out applying the SPH depth integrated model to other case studies.

5.2 Discussion on the results of part 2

The study on the erosion processes allows comparing two erosion laws which are not based on the same parameters. On one hand, the Hungr erosion law is based on the flow velocity and the flow depth. On another hand, the Egashira law is based on the flow velocity and the slope of the terrain. Both of these laws allow increasing the initial volume of debris along the path in order to get the same final volume of debris as in the real event. However the volume does not vary in the same manner using both laws. The results show that using the Egashira law, the volume tends to vary in a more similar way as in the real debris flow. Indeed, the simulation of the 2000 Tsing Shan debris flow event shows that the volume becomes a maximum before the end of the flow path. This feature is characteristic of a debris flow, which normally ends in deposition area, where no erosion processes take place and where debris materials are only deposited.

The application of the Egashira law to the 1990 and 2000 Tsing Shan debris flows shows that this law gives interesting results concerning the deposition pattern, i.e. the height of the deposition lobes and the flow velocity. Especially the flow velocity is more realistic when the Egashira law is used.

Therefore the Egashira law presents results, which seems to be more realistic than those got using the Hungr erosion law. However, the Hungr erosion law has one advantage, which is really relevant for people working on debris flow simulation. It concerns the number of input parameters. The Hungr law requires only one input parameters (the erosion coefficient, E_s) when the Egashira erosion law requires three input parameters. Therefore the Hungr erosion law is easier to use.

This study about the Hungr and the Egashira law shows also that it is quite difficult to assess the erosion processes occurring during debris flow event. Indeed, the comparison of the linear erosion rate shows that this magnitude does not vary in the same manner during the real event and during the simulations.

The chapter 4 ends with the proposition of a new erosion law depending strongly on the channel slope. This law tries to represent in a more realistic manner erosion processes. Indeed, as it is written in the literature, erosion processes depends strongly on the slope of the terrain. For instance, Rickenmann, Webber and Stephanov proposed in 2003 (*Erosion by debris flows in field and laboratory experiments*) proposed an erosion law based on a slope factor:

$$A_e = a_0 (V_m) \left(\frac{\rho_m}{\rho_w} \right) S^{\beta_1} \quad (5.1)$$

Where:

- A_e is the erosion yield per unit channel length
- a_0 is an empirical factor
- V_m is the mixture volume which enters the reach from upstream
- ρ_m is the density of the mixture entering
- ρ_w is the water mixture density
- S is the channel gradient
- β_1 is the exponent of the slope channel

The proposed erosion law has only been tested in the model using two case studies and has given more realistic results. This law has to be validated in laboratory test.

6 CONCLUSION

As describe in the chapter 1, this work has aims to test and improve the SPH depth integrated model written by Pastor (2005) in order to develop a model able to be used for risk analysis in engineering praxis. This model was already validated using analytical methods and few back-analyses of real case studies. In this master thesis, the model has been applied to three well-documented case studies in order to test its ability to predict the runout distance, the debris deposition and the final volume. The model is able to predict the flow velocity for debris flows, which have a simple flow path (i.e. without bifurcation). In case that debris flows bifurcate in two branches, the flow velocity decreases strongly at the bifurcation. This characteristic has not been observed in the real event and therefore it is a failing of the model.

However, in the second part of the thesis, the work done on erosion processes has improved the results obtained with the former version of the model. Indeed, the implementation of the Egashira erosion law gives to the model the ability to better predict flow velocity and deposition pattern than the version of the model with the Hungr erosion law. Nevertheless, both Hungr and Egashira laws do not predict the variations of erosion rate and volume increase as it occurs during the real events. Erosion processes are hardly modeled. However both of these erosion laws give a good estimation of the final volume.

In general the SPH depth integrated model has been validated to anticipate the most important characteristics of debris flow, which are runout distance, final volume, flow velocity and deposition pattern. For engineers it is important to assess these magnitudes as accurate as possible to plan mitigation measures in response of a potential risk.

The results got in this thesis correspond to the two initial objectives. Indeed the model has well simulated three case studies. Moreover the values for the input parameters have been compared to values found in the literature and are in the same range. Secondly some functions of the SPH depth integrated model have been improved by implementing a modified erosion law.

However the research about the depth integrated model is not completed and some future research lines can be proposed:

- (i) The work on erosion processes, which has been started in this thesis, should be continued. The proposed erosion law should be tested in the laboratory with flume experiments. Moreover new erosion laws can be found using finite elements methods (like PFC3D) to simulate the flow of granular suspensions in 'virtual' rheometers.
- (ii) The model has to be applied to others case studies in order to create a valuable database of calibrated parameters.
- (iii) Currently a PhD student is working on the SPH depth integrated model in order to use hydrographs as input. In fact rainfall precipitations are not taken into consideration until now although this data are relevant to predict debris flows.
- (iv) At the moment the SPH depth integrated is a 2D model. A possible and interesting development is the upgrade to three dimensions. 3D models are more accurate than 2D models because for each point of calculation (each node), the magnitudes of the different parameters vary along the vertical axis.
- (v) A commercial version of the model could be a good opportunity to increase the community of users and therefore improve the valuable database of parameters.

REFERENCES

- Brufau P., Garcia-Navarro P., Ghilardi P., Natale L. and Savi F., (2000) 1D mathematical modeling of debris flow, *Journal of Hydraulic Research*, vol. 38, n° 6, p. 435-446
- Cannon S.H. and Savage Z.S., (1988) A mass-change model for the estimation of debris-flow runout, *Journal of geology*, vol. 96, p. 221-227
- Chen H. and Lee C.F., (2003) A dynamic model for rainfall-induced landslide on natural slope, *Geomorphology*, vol. 51, p. 269-288
- Chen H, Crosta G.B., and Lee C.F., (2006) Erosional effects on runout of fast landslides, debris flows and avalanches: a numerical investigation, *Géotechnique*, vol. 56, n° 5, p. 305-322
- Coe J.A. et al., (2007) Initiation conditions for debris flows generated by runoff at Chalk Cliffs, central Colorado, *Geomorphology*
- Coe J.A. et al., (2007) Introduction to the special issue on debris flows initiated by runoff, erosion, and sediment entrainment in western North America, *Geomorphology*
- Costa J.E., (1984) Physical of Geomorphology of debris flow. *In Developments and application of geomorphology. Edited by Costa J.E. and Fleisher P.J., Springer – Verlin Heidelberg*, p. 268 – 317
- Coussot P. and Meunier M., (1995) Recognition, Classification and Mechanical description of debris flows, *Earth Sciences Reviews*, vol. 40, p. 209-227
- Coussot P., (1997) *Rhéologie des boues et laves torrentielles: étude de dispersions et suspensions concentrées*, France, CEMAGREF, Les études. Montagne, 415 pages
- Crosta G.B., (2004) Introduction to the special issue on rainfall triggered landslides and debris flow, *Engineering Geology*, vol. 73, p. 191 – 192
- Davies T.R., Phillips C.J., Pearce A.J. and ZHANG X.B., (1992) Debris flow behaviour – an integrated overview. *In Erosion, debris flow and environment in mountain regions (Proceedings of Chengdu Symposium, June 1992)*, IAHS Publication, n° 209
- Egashira S., Honda N. and Itoh T., (2001) Experimental study on the entrainment of bed material into debris flow, *Physics and chemistry of the Earth (C)*, vol. 26, n° 9, p. 645-650
- Erlichson H., (1991) A mass-change model for the estimation of debris-flow runout: a second discussion: conditions for the application of the rocket equation, *Journal of Geology*, vol. 99, p. 633-634
- Fannin R.J. and Wise M.P., (2001) An empirical-statistical model for debris flow travel distance, *Canadian Geotechnical Journal*, vol. 38, p. 982-994
- Frenette M. and Julien P.Y., (1987) Computer modeling of soil erosion and sediment yield from large watersheds, *International Journal of Sediment Research*, n° 1
- Govindarajou R.S and associate member, (1998) Effective erosion parameters for slopes with spatially varying properties, *Journal of Irrigation and Drainage Engineering*, vol. 124, n° 2, p. 81-88
- Haddad B., (2007) *Modelización numérica mediante elementos finitos y SPH de los geomateriales fluidificados: Aplicación a los deslizamientos rápidos de ladera*, Universidad Complutense de Madrid, Facultad de Ciencias Geológicas, Departamento de Geodinámica, 400 pages (PhD thesis)
- Hungr O., Morgan G.C. and Kellerhals R., (1984) Quantitative analysis of debris torrent hazards for design of remedial measures, *Canadian Geotechnical Journal*, vol. 21, p. 663-677

Hungr O., (1990) Momentum transfer and friction in rock avalanches: Discussion, *Canadian Geotechnical Journal*, vol. 27, p. 687

Hungr O. and Evans S.G., (1997) A dynamic model for landslides with changing mass. *In Proceedings international symposium on engineering geology and the environment*, 23 – 27 June 1997, Athens. Edited by Marinos P.G., Koukis G.C., Tsiambaos G.C. and Stournaras G.C., Brookfield, p. 719-724

Hungr O., (1995) A model for the runout analysis of rapid flow slides, debris flows, and avalanches, *Canadian Geotechnical Journal*, vol. 32, p. 610-623

Hungr O., McDougall S. and Bovis M., (2005), Entrainment of material by debris flows. *In Debris flow and related phenomena*. Edited by Jakob M. and Hungr O., Praxis-Springer, Chapter 7, pp. 135-158

Hungr O., (2006) Rock avalanche, process and modeling. *In Proceedings of the NATO advanced Research on Massive Rock Slope Failure, New models for hazard assessment Celano, Italy, 16-22 June 2002*. Edited by Evans S.G., Scarascia Mugnozza G., Storm A. and Hermans R.L., Springer

Iverson R.M., (1997) The physics of debris flows, *Review of geophysics*, vol. 35, n° 3, p.245 – 296

Iverson R.M, Reid M.E. and LaHusen R.G., (1997) Debris flow mobilization from landslides, *Annual review Earth Planet Sci.*, vol. 25, p. 85-138

Iverson R.M., (2000) Landslides triggered by rain infiltration, *Water Resources Research*, vol. 36, p. 1897-1910

Iverson R.M. and Delinger R.P., (2001) Mechanics of debris flows and debris-laden flash floods. *In Proceedings of the seventh federal interagency sedimentation conference*, Reno, Nevada, p. IV-1 – IV-8

Jakob M., Anderson D., Fuller T., Hungr O. and Ayotte D., (2000) An unusually large debris flow at Hummingbird Creek, Mara Lake, British Columbia, *Canadian Geotechnical Journal*, vol. 37, p. 1109-1125

Jakob M., (2005) A size classification for debris flows, *Engineering Geology*, vol. 79, p 151-161

Jakob M. and O. Hungr, (2005) *Debris flow hazards and related phenomena*, Chichester (England), 739 p.

King J.P., (2001) The Tsing Shan Debris Flow and Debris Flood, *Landslide study report No. LSR 2/2001*, Geotechnical Engineering Office, Hong Kong, 216 p

King J.P., (2001) The 2000 Tsing Shan Debris Flow and Debris Flood, *Landslide study report No. LSR 3/2001*, Geotechnical Engineering Office, Hong Kong, 54 p.

Koçyigit Ö. And Gürer I., (2007) Effect of the Voellmy Coefficients on Determining Run-out Distance: A Case Study at Uzungöl, Turkey, *Journal of Science*, vol. 20, n° 3, p79-85

Liu G.R. and Liu M.B., (2003) *Smoothed Particle Hydrodynamics – a meshfree particle method*, World Scientific Publishing Co. Pte. Ltd., Singapore

Major J.J. and Iverson R.M., (1999) Debris-flow deposition: Effects of pore-fluid pressure and friction concentrated at flow margins, *Geological Society of America Bulletin*, vol. 111, p.1424-1434

Major J.J., (2000) Gravity-driven consolidation of granular slurries – implication for debris flows deposition and deposit characteristics, *Journal of sedimentary research*, vol. 70, n° 1, p. 64-83

- Maunsell F., Wilson S. and Venture J., (2005) Report on the Debris Flow at Sham Tseng San Tsuen of 23 August 1999, *Geo Report*, Geotechnical Engineering Office, Hong Kong , n° 169, 92 p.
- McDougall S., (1998) *A new continuum dynamic model for the analysis of extremely rapid landslide motion across complex 3D terrain*, University of British Columbia, 253 pages (PhD thesis)
- McDougall S. and Hungr O., (2004) A model for the analysis of rapid landslide motion across three-dimensional terrain, *Canadian Geotechnical Journal*, vol. 41, p. 1084-1097
- McDougall S. and Hungr O., (2005) Dynamic modeling of entrainment in rapid landslide *Canadian Geotechnical Journal*, vol. 42, p. 1437-1448
- McNeil J., Taylor C. and Lick W., (1996), Measurements of erosion of undisturbed bottom sediments with depth, *Journal of Hydraulic Engineering*, vol. 122, n° 6, p. 316-324
- Pirulli M. and Mangeney A., (2008) Results of Back-Analysis of the Propagation of Rock Avalanches as a Function of the Assumed Rheology, *Rocks Mechanics and Rock Engineering*, vol. 41, n° 1, p. 59-84
- Pitman E.B., Nichita C.C., Patra A.K., Bauer A.C., Bursik M. and Webb A. (2003) A model of granular flows over an erodible surface, *Discrete and Continuous Dynamical Systems, Series B*, vol. 3, n°4, p. 589-599
- Rickenmann D. and Zimmermann M., (1993) The 1987 debris flows in Switzerland: documentation and analysis, *Geomorphology*, vol. 8, p. 175 – 189
- Rickenmann D. and Koch T., (1997) Comparison of debris flow modelling approaches. *In Proceedings of the 1st International Conference on Debris-flow Hazards Mitigation: Mechanics, Prediction and Assessment*. Edited by C.L. Chen. ASCE, New York. p. 576-585
- Rickenmann D., (1999) Empirical relationship for debris flows, *Natural Hazards*, vol. n° 19, p. 47-77
- Rickenmann D. and Chen C.L., (2003) *Debris-flow hazards mitigation: mechanics, prediction, and assessment: proceedings of the third international conference: Davos, Switzerland, September 10-12, 2003*, Rotterdam, Millpress
- Stock J.D. and Dietrich E.W., (2006) Erosion of steepland valleys by debris flow, *Geological Society of America*, vol. 118, n° 9/10, p. 1125 – 1148
- Takahashi T., (1991) *Debris flow*, IAHR Monograph, Rotterdam, The Netherlands, 165 pages
- Takahashi T., Nakagawa H., Harada T. and Yamashiki, Y., (1992) Routing debris flows with particle segregation, *Journal of Hydraulic Engineering*, vol. 118, n° 11, p. 1490-1507
- Takahashi T., (2007) *Debris flow: Mechanics, Prediction and Counter Measures*, Taylor&Francis, 448 pages
- Van Gassen W. and Cruden D.M., (1989) Momentum transfer and friction in the debris of rock avalanches, *Canadian Geotechnical Journal*, vol. 26, p. 623-628
- Wen B.P. and Aydin A., (2005) Mechanism of rainfall induced slide-debris flow: Constraints from its microstructure of its slip zone, *Engineering geology*, vol. 78, p. 69-88

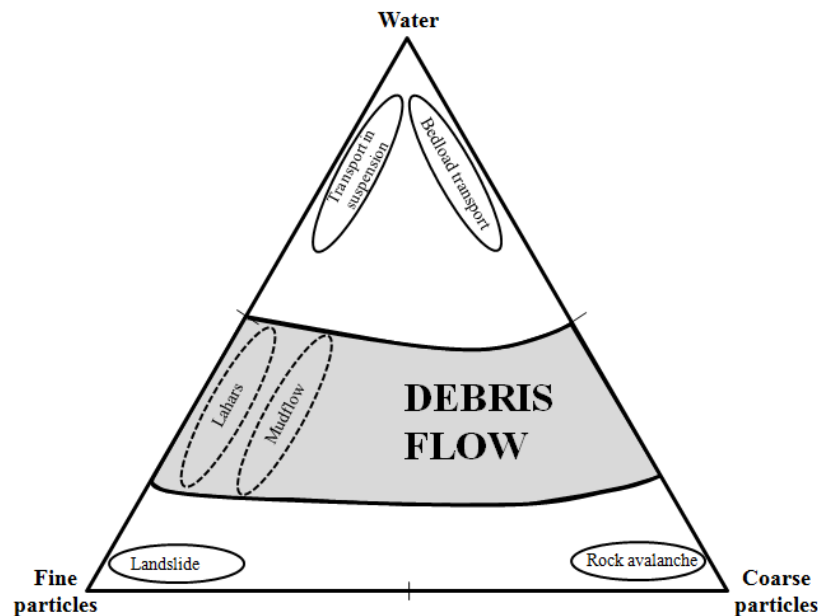
CONTACTS

- Manuel Pastor
manuel.pastor@cedex.es
CEDEX (Centro de Estudios y de Experimentacions de Obras Publicas)
Madrid (SPAIN)
- Roland Kaitna
Roland.Kaitna@boku.ac.at
Universität für Bodenkultur
Vienna (AUSTRIA)
- Dieter Rickenmann
Dieter.rickenmann@wsl.ch
Swiss Federal Institute for Forest, Snow and Landscape Research (WSL)
Birmensdorf (SWITZERLAND)
- Johannes Hübl
Johannes.huebl@boku.ac.at
Universität für Bodenkultur
Vienna (AUSTRIA)
- Pierre-Yves Colin
pierre-yves.colin@engref.agroparistech.fr
AgroParisTech-ENGREF
Nancy (France)

APPENDIXES

Appendix 1. Composition of a debris flow (ternary phase diagram)	ii
Appendix 2. Slope angles measures at sites of debris flow initiation from landslides in localities where numerous debris flows resulted from one or more hydrologic event .iii	.iii
Appendix 3. Critical rainfall to initiate a debris flow	iv
Appendix 4. Schematic longitudinal profile of a debris flow	v
Appendix 5. Landslide velocity scale after Cruden and Varnes (1996)	vi
Appendix 6. Details on the “propagation – consolidation” approximations done in the 2D SPH depth integrated model	vii
Appendix 7. Details on the depth integration estimations done in the 2D SPH depth integrated model	x
Appendix 8. Details on the integral approximation of functions and derivatives in the SPH method	xiv
Appendix 9. Details on the SPH discretization of integral approximation of functions and derivatives	xix
Appendix 10. Description of the Runge Kutta 4th (RK4).....	xxviii

Appendix 1. Composition of a debris flow (ternary phase diagram)



Compositions can be represented in an equilateral triangle. Each corner represents an element (water, fine particles, coarse particles), and each side a binary system. Ternary compositions (like debris flow) are represented by points within the triangle, the relative proportions of the elements being given by the lengths of the perpendiculars from the given point to the side of the triangle opposite the appropriate element.

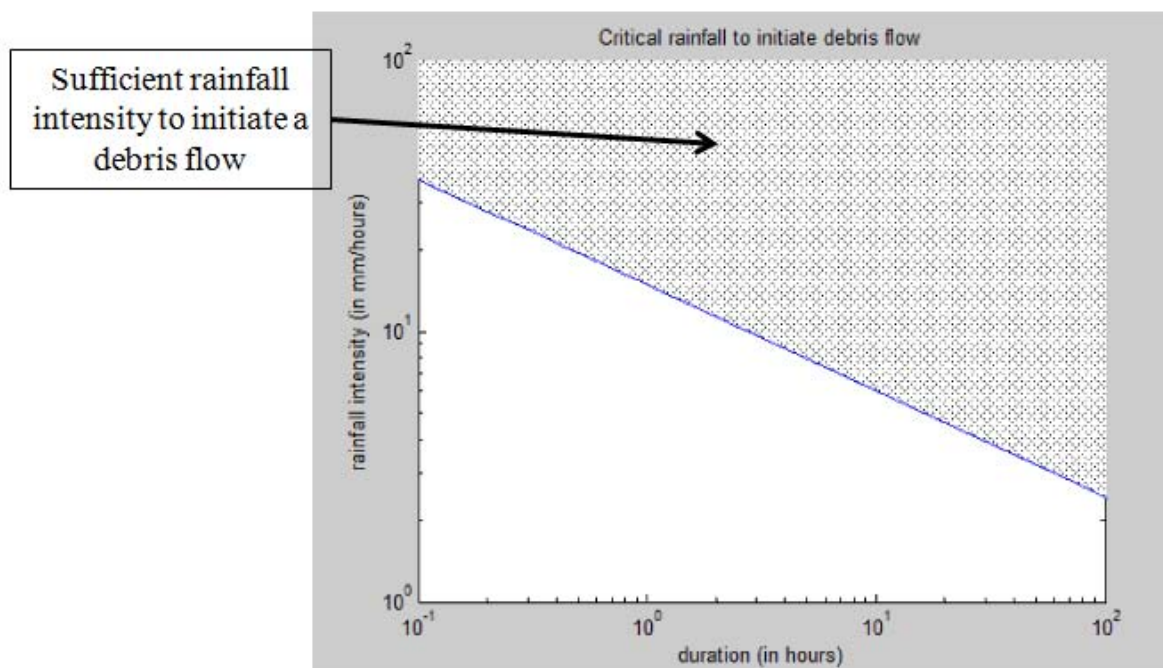
This diagram shows that the proportion of solid particle, in a debris flow, is bigger than 50 %. The difference between lahars, mudflow and debris flow is well represented: Solid particles of a debris flow are coarser than the one of mudflow or lahars. Finally, composition of debris flow can be compared to others natural hazards composition (as landslide, bedload transport...).

Appendix 2. Slope angles measures at sites of debris flow initiation from landslides in localities where numerous debris flows resulted from one or more hydrologic event

Reference	Location	Slope angles (degrees)
Temple & Rapp 1972	Tanzania	28–44
O’Loughlin 1972	Southwestern British Columbia, Canada	24–48
Lumb 1975	Hong Kong	25–45
Campbell 1975	Southern California, USA	27–56
Selby 1976	New Zealand	32–34
Statham 1976	Wales	27–37
Pomeroy 1980	Pennsylvania, USA	20–40
Heller 1981	Northwestern Washington, USA	20–40
Ellen et al 1988	Northern California, USA	20–50
Pierson et al 1992	Hawaii, USA	30–60
Rickenmann & Zimmermann 1993	Switzerland	27–39

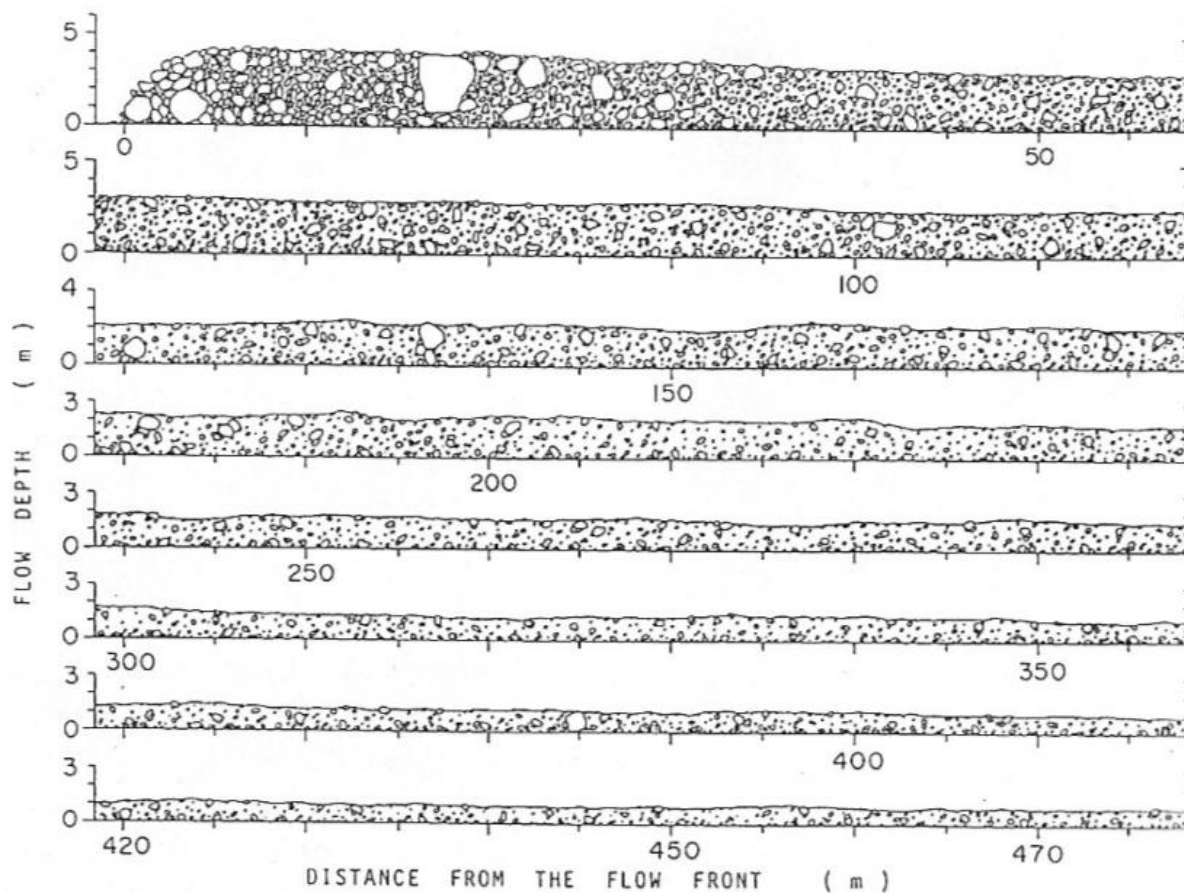
Source: Iverson et al., *Debris flow mobilization from landslide* (1997)

Appendix 3. Critical rainfall to initiate a debris flow



Appendix 4. Schematic longitudinal profile of a debris flow

Flow depth and boulder size at each location are depicted depending on the observed data.



Source: Takahashi, *Debris Flow* (1991)

Appendix 5. Landslide velocity scale after Cruden and Varnes (1996)

Velocity class	Description	Velocity (mm/sec)	Typical velocity	Typical human response
7	Extremely rapid			Nil
	↓	5×10^3	5 m/sec	
6	Very rapid			Nil
	↓	5×10^1	3 m/min	
5	Rapid			Evacuation
	↓	5×10^{-1}	1.8 m/hr	
4	Moderate			Evacuation
	↓	5×10^{-3}	13 m/month	
3	Slow			Maintenance
	↓	5×10^{-5}	1.6 m/year	
2	Very slow			Maintenance
	↓	5×10^{-7}	16 mm/year	
1	Extremely slow			Nil

Source: Jakob M. and Hungr O., *Debris flow and related phenomena*

Appendix 6. Details on the “propagation – consolidation” approximations done in the 2D SPH depth integrated model

The starting point is the balance equations for saturated soils, equations (2.29) and (2.30) of the V- p_w model. (c.f. chapter 2).

The V- p_w model consists to the following equations:

$$- \operatorname{div} (-k_w \operatorname{grad} p_w) + \operatorname{div} v^s = 0 \quad (2.29)$$

$$- \rho \frac{D^{(s)} v^s}{Dt} = \rho b + \operatorname{div} \sigma \quad (2.30)$$

- The constitutive (c.f. subsection 2.3) and kinetic equations (equation 2.28) are the same as the ones of the general model.

An important aspect is that fast flows involve two physical phenomena which appear in equations above:

- Consolidation and dissipation of pore pressure
- Propagation.

In order to gain insight on the relative importance of all terms, the above equation are expressed in non-dimensional form as proposed by Hutter and Koch (1991), introducing a characteristic length of the landslide L and H a characteristic depth of the sliding mass, and the ratio $\varepsilon = H / L$. In typical cases, L will be of the order of 10²m and H of the order of 5 m. Therefore ε will be small. Next some characteristic magnitudes of the slide are introduced:

- L as a characteristic length
- H as a characteristic depth of the flow
- $T = \sqrt{L / g}$ as a time scale
- $v = \sqrt{gL}$ as a typical velocity
- The stresses and pressures will be compared to the reference pressure $\rho_0 g H$, where ρ_0 is a reference density.

The x_1 and x_2 axes will be chosen on a plane close to that of the slope, or a horizontal one and the x_3 axis will be normal to this plane. The V- p_w model can be cast in a dimensionless form by introducing

$$\begin{aligned} \hat{x}_1 &= x_1 / L & \hat{x}_2 &= x_2 / L & \hat{x}_3 &= x_3 / H \\ \hat{v}_1 &= v_1 / \sqrt{gL} & \hat{v}_2 &= v_2 / \sqrt{gL} & \hat{v}_3 &= v_3 / \varepsilon \sqrt{gL} \\ \hat{\sigma} &= \sigma / \rho_0 g H & \hat{p}_w &= p_w / \rho_0 g H \end{aligned} \quad (6.1)$$

The non dimensional form of the balance of mass and momentum can be written as:

$$\operatorname{div} \hat{v}^s = \theta \left[\varepsilon^2 \frac{d^2 \hat{p}_w}{d\hat{x}_1^2} + \varepsilon^2 \frac{d^2 \hat{p}_w}{d\hat{x}_2^2} + \frac{d^2 \hat{p}_w}{d\hat{x}_3^2} \right] \quad (6.2)$$

Where the dimensionless magnitude θ is given by:

$$\theta = \left(\frac{\sqrt{L/g}}{H / (k_w \rho_0 g)} \right) \quad (6.3)$$

Assuming the same typical values for L and H , and a permeability such that $k_w \rho_0 g$ is of the order of 10^{-n} ms^{-1} , it can be seen that θ will be close to 10^{-n} . Typical values are 10^{-9} for clays, 10^{-7} for silts, 10^{-5} for fine sands and 10^{-1} for gravels.

For debris flows, ε^2 can be neglected in this equation and therefore (6.2) can be reduced to:

$$\text{div } \hat{v}^S = \theta \frac{d^2 \hat{p}_w}{d\hat{x}_3^2} \quad (6.4)$$

Where appear only derivatives with regard to the normal to the terrain surface, which is the principal direction of the dissipation of pore pressure.

On another hand, the component along x_3 of the balance momentum equation for the mixture (2.30) is:

$$\varepsilon \frac{\partial \hat{v}_3}{\partial \hat{t}} = -1 + \left[\varepsilon \frac{d\hat{\sigma}_{13}}{d\hat{x}_1} + \varepsilon \frac{d\hat{\sigma}_{23}}{d\hat{x}_2} + \frac{d\hat{\sigma}_{33}}{d\hat{x}_3} \right] \quad (6.5)$$

The last equation comes from the assumptions that the gravity acts only along the axis x_3 and $b_3 = -g = -1$.

Assuming that ε is small, the equation (6.5) can be reduced to:

$$-1 + \frac{\partial \hat{\sigma}_{33}}{\partial \hat{x}_3} = 0 \quad (6.6)$$

Or in terms of effective stresses:

$$-1 + \frac{\partial \hat{\sigma}'_{33}}{\partial \hat{x}_3} - \frac{\partial \hat{p}_w}{\partial \hat{x}_3} = 0 \quad (6.7)$$

From the equations (6.4), (6.6) and (6.7), the dimensional equations are:

$$\begin{aligned} \text{div } v &= \frac{\partial}{\partial x_3} \left(-k_w \frac{\partial p_w}{\partial x_3} \right) \\ -\rho g + \frac{\partial \sigma_{33}}{\partial x_3} &= 0 \\ -\rho g + \frac{\partial \sigma'_{33}}{\partial x_3} - \frac{\partial p_w}{\partial x_3} &= 0 \end{aligned} \quad (6.8)$$

Assuming that the velocity field can be decomposed as

$$\hat{v} = \hat{v}_0 + \hat{v}_1 \quad (6.9)$$

And the pore pressure field decomposed as:

$$\hat{p}_w = \hat{p}_{w_0} + \hat{p}_{w_1} \quad (6.10)$$

Where \hat{p}_{w_0} is a hydrostatic field varying linearly from zero at the surface to $\rho g h$ at the bottom of the flow.

From these assumptions, the following equations are obtained:

$$\begin{aligned} \operatorname{div} \hat{v}_0 + \operatorname{div} \hat{v}_1 &= \theta \left(\frac{\partial^2 \hat{p}_{w_0}}{\partial \hat{x}_3^2} + \frac{\partial^2 \hat{p}_{w_1}}{\partial \hat{x}_3^2} \right) \\ \operatorname{div} \hat{v}_0 + \operatorname{div} \hat{v}_1 &= \theta \frac{\partial^2 \hat{p}_{w_1}}{\partial \hat{x}_3^2} \end{aligned} \quad (6.11)$$

In that the density of the mixture is constant, $\operatorname{div} \hat{v}_0 = 0$ (equation (2.31), c.f. chapter 2.). From here, the following equation is deduced:

$$\operatorname{div} \hat{v}_1 = \theta \frac{\partial^2 \hat{p}_{w_1}}{\partial \hat{x}_3^2} \quad (6.12)$$

In this way, the perturbed field v_1 can be identified as the velocity field corresponding to the unidimensional consolidation and v_0 as the velocity field corresponding to propagation. This result is of paramount importance, and clarifies the assumptions which should be made when modeling these phenomena.

First of all, incompressibility is not a feature of rheological soil behaviour, but a consequence of the coupled behaviour between the pore fluid and the soil skeleton. Indeed, this will explain the "undrained" behaviour in simple shear devices, where pressures depend on shear strain rate.

The variations of p_{w_1} due to the consolidation cause the changes of the hydrostatic tensor σ'_{33_1} and a volumetric deformation of the solid skeleton given by:

$$\operatorname{div} v_1 = \frac{1}{K_T} \frac{Dp_w}{Dt} \quad (6.13)$$

Where K_T is the oedometric modulus of soil skeleton. From here the next equation is obtained:

$$\frac{1}{K_T} \frac{Dp_w}{Dt} = \frac{\partial}{\partial x_3} \left(-k_w \frac{\partial p_w}{\partial x_3} \right) \quad (6.14)$$

Where p_w depends on x_1 , x_2 and x_3 .

In summary the "propagation – consolidation" model consists in the following set of partial derivative equations:

$$\rho \frac{Dv_0}{Dt} = \rho b + \operatorname{div} \sigma \quad (6.15)$$

$$\operatorname{div} v_0^{(s)} = 0 \quad (6.16)$$

$$\frac{1}{K_T} \frac{Dp_w}{Dt} = \frac{\partial}{\partial x_3} \left(k_w \frac{\partial p_w}{\partial x_3} \right) \quad (6.17)$$

Appendix 7. Details on the depth integration estimations done in the 2D SPH depth integrated model

• Introduction

The following model derives from the equation presented in the appendix 6:

$$\rho \frac{Dv_0}{Dt} = \rho b + \text{div } \sigma \quad (6.17)$$

$$\text{div } v_0^{(s)} = 0 \quad (6.18)$$

$$\frac{1}{K_T} \frac{Dp_w}{Dt} = \frac{\partial}{\partial x_3} \left(k_w \frac{\partial p_w}{\partial x_3} \right) \quad (6.19)$$

Next, the sub indexes “0” in the velocity field and “1” in the pressure field will be dropped.

Taking into account the incompressibility condition (equation 6.18), the equation (6.17) can be written in a conservative form as:

$$\rho \frac{\partial v_i}{\partial t} + \frac{\partial}{\partial x_j} (\rho v_i v_j) = \frac{\partial}{\partial x_j} (\sigma_{ij}) + \rho b_i \quad (7.1)$$

These equations will be integrated along the direction normal to the terrain surface using the Leibnitz and Reynolds theorem. The Leibnitz theorem to integrate the equations in depth establishes that:

$$\int_a^b \frac{\partial}{\partial s} F(r, s) dr = \frac{\partial}{\partial s} \int_a^b F(r, s) dr - F(b, s) \frac{\partial b}{\partial s} + F(a, s) \frac{\partial a}{\partial s} \quad (7.2)$$

Where a and b are functions differentiable of s , and $F(r, s)$ and $\frac{\partial F(r, s)}{\partial s}$ are continuous in r and in s .

After the Reynolds decomposition theorem, a variable can be decomposed in its averaged value and the fluctuation over this value:

$$a = \bar{a} + a' \quad (7.3)$$

Where the averaged value is:

$$\bar{a} = \frac{1}{h} \int_z^{z+h} a(x_3) dx_3 \quad (7.4)$$

In certain cases, turbulent fluctuations exist over averaged states. The equations are then averaged over a representative time length T , and an extra term, σ_{ij}^R , equivalent to the Reynolds stresses given as:

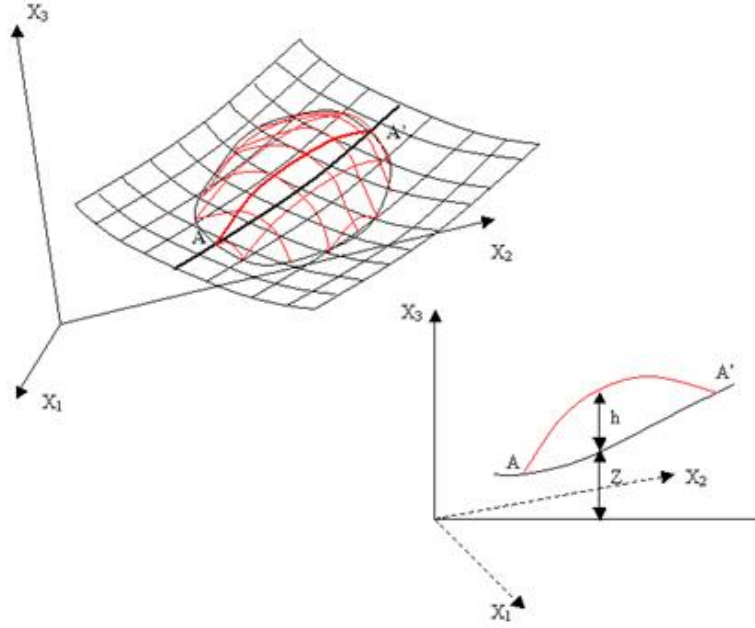
$$\sigma_{ij}^R = -\frac{1}{T} \int_t^{t+T} (\rho v_i' v_j') dt \quad (7.5)$$

In above v_i' represent the fluctuation of the velocity v_i over the average \bar{v}_i .

$$v_i(x_1, x_2, x_3) = \bar{v}_i(x_1, x_2) + v_i'(x_1, x_2, x_3) \quad (7.6)$$

From here the stress tensor $\bar{\sigma}_{ij}$ will include Reynolds stresses.

The reference system given in the following figure will be used.



Reference system and notation used in the analysis – **Source:** Thesis of B.Hadad

- **Integration along depth of the propagation equations**

- **Balance of mass:**

The first step is to integrate along depth the balance of mass equation (6.18):

$$\frac{\partial}{\partial x_i} v_j = 0 \quad (7.7)$$

$$\int_z^{z+h} \frac{\partial}{\partial x_j} v_j dx_3 = \frac{\partial}{\partial x_j} \int_z^{z+h} v_j dx_3 - \left[v_j \frac{\partial(z+h)}{\partial x_j} - v_3 \Big|_{z+h} \right] + \left[v_j \frac{\partial z}{\partial x_j} - v_3 \Big|_z \right] = 0 \quad (7.8)$$

Developing this equation and taking into account the value of the averaged velocity, which is $v_3 \Big|_z = 0$ at the bottom and $\frac{D}{Dt}(h+z) = v_3$ at the surface, the next equation is obtained:

$$\frac{\partial}{\partial x_j} (h \bar{v}_j) + \frac{\partial}{\partial t} (h+z) - \frac{\partial}{\partial t} (z) = 0 \quad (7.9)$$

And therefore the equation of mass balance integrated along depth is:

$$\frac{\partial h}{\partial t} + \frac{\partial}{\partial x_j} (h \bar{v}_j) = 0 \quad \text{con } j=1,2 \quad (7.10)$$

Where \bar{v}_j is the component of the averaged velocity along the axis X_j .

In general, the basal surface do not change and $\frac{\partial}{\partial t} (h+z) = \frac{\partial h}{\partial t}$ but in some occasions, erosion occurs and this phenomena has to be taken into account by introducing an erosion rate, e_r , defined as:

$$e_r = -\frac{\partial z}{\partial t} \quad (7.11)$$

Thus, $\frac{\partial}{\partial t} (z+h) = \frac{\partial h}{\partial t} - e_r$ is obtained and has to be integrated to the equation of mass balance.

Therefore the depth integrated equation of the balance of mass is:

$$\frac{\partial h}{\partial t} + \frac{\partial}{\partial x_j} (h \bar{v}_j) = e_r \quad \text{con } j=1,2 \quad (7.12)$$

○ **Balance of linear momentum:**

Assuming that the stresses on the surface are null and the stresses at the bottom are given by:

$$t^B = -\rho gh \text{ grad } Z - \tau_b \quad (7.13)$$

The equation (7.1) of linear momentum balance is integrated along the depth and gives:

$$\rho \frac{D(h\bar{v})}{Dt} + \text{grad} \left(\frac{1}{2} \rho gh^2 \right) = -\frac{1}{\rho} e_r \bar{v} + \rho bh + \text{div}(h\bar{s}) - \rho gh \text{ grad } Z - \tau_b - \rho h \bar{v} \text{ div}(\bar{v}) \quad (7.14)$$

In summary, the submodel of propagation integrated along x_3 can be expressed as:

$$\frac{\partial h}{\partial t} + \frac{\partial}{\partial x_j} (h \bar{v}_j) = e_r \quad \text{con } j=1,2 \quad (7.15)$$

$$\rho \frac{D(h\bar{v})}{Dt} + \text{grad} \left(\frac{1}{2} \rho gh^2 \right) = -\frac{1}{\rho} e_r \bar{v} + \rho bh + \text{div}(h\bar{s}) - \rho gh \text{ grad } Z - \tau_b - \rho h \bar{v} \text{ div}(\bar{v})$$

● **Integration along depth of the consolidation equation:**

The existence of a saturated layer with a height, h_s , at the bottom of the flow has been considered (Hung, 1995). Therefore, the decrease of the pore pressure is caused by the vertical consolidation of this layer.

The equation with partial derivative of the consolidation is the equation numbered (6.19):

$$\frac{1}{K_T} \frac{Dp_w}{Dt} = \frac{\partial}{\partial x_3} \left(k_w \frac{\partial p_w}{\partial x_3} \right) \quad (7.16)$$

The consolidation coefficient, C_v , can be introduced:

$$C_v = \frac{k_w}{\gamma_w c} = K_T k_w \quad (7.17)$$

Where:

- C_v is the consolidation coefficient,
- k_w is the permeability,
- γ_w is the specific weight of the fluid,
- c the compressibility of the material, and
- K_T is the volumetric rigidity of the solid skeleton.

After introduction of this coefficient, the following equation is obtained:

$$\frac{\partial p_w}{\partial t} + v_i \frac{\partial p_w}{\partial x_i} = \frac{\partial}{\partial x_3} \left(C_v \frac{\partial p_w}{\partial x_3} \right) \quad (7.18)$$

This equation can be integrated along depth to give:

$$\frac{\partial}{\partial t}(\bar{p}_w h) + \frac{\partial}{\partial x_i}(\bar{v}_i \bar{p}_w h) = c_v \frac{\partial p_w}{\partial x_3} \Big|_{z+h} - c_v \frac{\partial p_w}{\partial x_3} \Big|_z \quad (7.19)$$

As the same time, the pore pressure can be approximated as:

$$p_w(x_1, x_2, x_3, t) = \sum_{j=1}^{nf} N_j^{(3)}(x_3) p_{wj}(x_1, x_2, t) \quad (7.20)$$

Where $N_j^{(3)}(x_3)$ are functions, which are employed in order to approximate the pressure variation along x_3 . In this model, functions of harmonic type, which satisfy the boundary conditions, have been used. In case that the pressure is null at the surface, the approximation is the following:

$$N_j^{(3)}(x_3) = \cos\left(\frac{2j-1}{2h}\pi(x_3 - z)\right) \quad j=1\dots nf \quad (7.21)$$

And therefore, the depth integrated consolidation equation is:

$$\frac{\partial}{\partial t}(P_{w_1} h) + \frac{\partial}{\partial x_k}(\bar{v}_k P_{w_1} h) = -\frac{\pi^2}{4h^2} c_v P_{w_1} \quad (7.22)$$

• Equations of the 2D depth integrated model

The model can be expressed in the following manner:

$$\begin{aligned} \frac{\partial h}{\partial t} + \text{div}(h\bar{v}) &= 0 \\ \rho \frac{\partial(h\bar{v})}{\partial t} + \rho \text{div}(h\bar{v} \otimes \bar{v}) + \text{grad}\left(\frac{1}{2}\rho gh^2\right) &= \rho bh + \text{div}(h\bar{s}) - \rho gh \text{grad} Z - \tau_b \quad (7.23) \\ \frac{\partial}{\partial t}(P_{w_1} h) + \frac{\partial}{\partial x_k}(\bar{v}_k P_{w_1} h) &= -\frac{\pi^2}{4h^2} c_v P_{w_1} \end{aligned}$$

This system of equation with partial derivatives represents after depth integrating the equation of mass balance, the equation of linear momentum balance and also the unidimensional equation of consolidation.

Assuming a fixed volume, which corresponds to a column integrated along depth and moving with a averaged velocity, the last equations can be written as:

$$\begin{aligned} \frac{Dh}{Dt} + h \text{div}(\bar{v}) &= e_r \\ \rho \frac{D(h\bar{v})}{Dt} + \text{grad}\left(\frac{1}{2}\rho gh^2\right) &= \rho bh + \text{div}(h\bar{s}) - \rho gh \text{grad} Z - \tau_b - \rho h \bar{v} \text{div}(\bar{v}) \quad (7.24) \\ \frac{\partial}{\partial t}(P_{w_1} h) + \frac{\partial}{\partial x_k}(\bar{v}_k P_{w_1} h) &= -\frac{\pi^2}{4h^2} c_v P_{w_1} \end{aligned}$$

Appendix 8. Details on the integral approximation of functions and derivatives in the SPH method

- **Integral approximation of functions**

We will start by considering a scalar value function $\phi(x)$ of $x \in \Omega \subset \mathbb{R}$ where Ω is a open bounded domain, and the equality

$$\phi(x) = \int_{\Omega} \phi(x') \delta(x'-x) dx' \quad (8.1)$$

Where $\delta(x)$ is the Dirac delta. Traditionally, Dirac delta “function” is defined as:

$$\delta(x) = \begin{cases} \infty & x=0 \\ 0 & |x|>0 \end{cases} \quad (8.2)$$

With the additional of “unity”:

$$\int_{\Omega} \delta(x) dx = 1 \quad (8.3)$$

This mathematical entity, the “Dirac delta” is a generalized function or a distribution. Distributions are a class of linear functions, applications which transform functions into real numbers.

The Dirac delta is defined in the distribution theory from a succession of functions or kernels $W_k(x, h)$ as for example:

$$W_k(x, h) = \frac{1}{\sqrt{2\pi h}} \exp\left(-\frac{x^2}{h}\right) \quad \text{with} \quad h = 1/k \quad (8.4)$$

It can be demonstrated that:

$$\lim_{h \rightarrow 0} \int_{\Omega} W_k(x'-x, h) \phi(x') dx' = \int_{\Omega} \phi(x') \delta(x'-x) dx' = \phi(x) \quad (8.5)$$

The Kernel is parameterized by introducing a length scale h , or an integer k .

Theses equations are called integral representation of $\phi(x)$ with a kernel $W(x)$. In order to simplify the notation, here after, (x) will be omitted when it is about a distribution.

Theses equations represent the first point for the construction of a SPH approximation where the value of the function is approximated by regular distributions.

The classic notation used in SPH is different to the one used until now and is:

$$\langle \phi(x) \rangle = \int_{\Omega} \phi(x') W(x'-x, h) dx' \quad (8.6)$$

- **Kernels: some basic properties and examples**

The accuracy of SPH approximations depends on the properties of the kernel $W(x, h)$. A special class of kernel is that of functions having radial symmetry, i.e., depending only on r :

$$r = |x' - x| \quad (8.7)$$

It is convenient to introduce the notation:

$$\xi = \frac{|x' - x|}{h} = \frac{r}{h} \quad (8.8)$$

This notation allows to write $W(x'-x, h)$ as $W(\xi)$. Here after, these notations will be used.

In order to be used in SPH approximation, the functions $W_k(x, h)$ are required to fulfill the following conditions:

(i)

$$\lim_{h \rightarrow 0} W(x' - x, h) = \delta(x) \quad (8.9)$$

(ii)

$$\int_{\Omega} W(x' - x, h) dx' = 1 \quad (8.10)$$

This condition, which can be deduced from the first one (i), can be interpreted as well as the ability of the approximation to reproduce a constant, namely polynomial of degree zero. It is spoken about zero order consistency.

(iii) The kernel $W(x - x', h)$ is positive and has a compact support:

$$W(x' - x, h) = 0 \text{ si } |x' - x| \geq kh \quad (8.11)$$

Where k is a positive integer which is usually taken as 2.

(iv) The kernel $W(x - x', h)$ is a monotonically decreasing function of ξ .

(v) The kernel $W(x - x', h)$ is a symmetric function of $(x' - x)$

It is possible to show that, under these conditions specified above, the approximation is second order accurate, i.e.:

$$\langle \phi(x) \rangle = \phi(x) + O(h^2) \quad (8.12)$$

In the framework of SPH formulations, several kernels have been proposed in the past. Among them, it is worth mentioning the following:

- The Gaussian kernel proposed by Gingold and Monaghan (1977) defined as:

$$W(x' - x, h) = W(\xi) = \frac{1}{h^{\text{ndim}} \pi^{(\text{ndim}/2)}} \exp(-\xi^2) \quad \xi \leq 3 \quad (8.13)$$

$$= 0 \text{ si no}$$

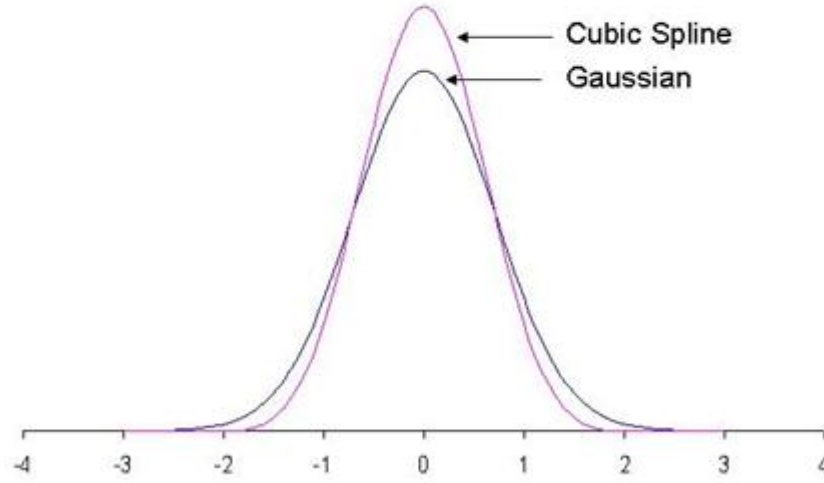
- The cubic spline introduced by Monaghan (Monaghan and Gingold 1983; Monaghan and Lattanzio 1985):

$$W(x' - x, h) = W(\xi) = \frac{C}{h^{\text{ndim}}} \begin{cases} \left(1 - \frac{3}{2}\xi^2 + \frac{3}{4}\xi^3\right) & \xi < 1 \\ \frac{1}{4}(2 - \xi)^3 & 1 \leq \xi \leq 2 \\ 0 & 2 \leq \xi \end{cases} \quad (8.14)$$

Where C is a constant which depends on the dimension of the domain:

$$C = \begin{cases} \frac{2}{3} & \text{for one dimension} \\ \frac{10}{7\pi} & \text{for two dimensions} \\ \frac{1}{\pi} & \text{for three dimensions} \end{cases} \quad (8.15)$$

The scaling factor is chosen for the kernel to satisfy conditions (2.111) and (2.112). The following figure depicts both kernels for the one dimensional case.



Kernels in 1D: Gaussian and cubic spline

- **Integral approximation of derivatives and differential operators**

The integral representation of the derivatives in SPH is written as:

$$\langle \phi'(x) \rangle = \int_{\Omega} \phi'(x') W(x'-x, h) dx' \quad (8.16)$$

The idea is that as h decreases and the kernel approaches the Dirac delta “function”, the proposed representation will also approach the value of the derivative. This expression is integrated by parts – in one dimensional problem –, and, taking into account that the kernel has compact support, it results:

$$\langle \phi'(x) \rangle = - \int_{\Omega} \phi(x') W'(x'-x, h) dx' \quad (8.17)$$

Next, integral approximations of some operators used in the mechanics of continuous medium

- *Gradient of scalar function:*

The SPH approximation of the gradient scalar function can be written as:

$$\langle \text{grad } \phi(x) \rangle = - \int_{\Omega} \phi(x') \text{grad}(W(x'-x, h)) d\Omega \quad (8.18)$$

It is important to note that the derivatives involved in the gradient have been obtained with respect to x' .

The gradient of the kernel is calculated taking into account that the kernel depends on $\xi = r/h$:

$$\text{grad } W = \frac{1}{h} \frac{dW}{d\xi} \left(\frac{x'-x}{r} \right) = \frac{1}{h} W' \frac{x'-x}{r} \quad (8.19)$$

Where W' is the derivative of the kernel respect to ξ .

From here, the following equation can be obtained:

$$\langle \nabla \phi(x) \rangle = - \int_{\Omega} \phi(x') \frac{1}{h} W' \frac{x'-x}{r} d\Omega \quad (8.20)$$

○ *Gradient of a vector function:*

For a vector function, $u_i(x)$, above results can be applied with a little change. The result is a second order tensor, with components given by:

$$\langle \text{grad } u(x) \rangle_{ij} = - \int_{\Omega} u_i(x') \frac{1}{h} W' \frac{x'_j - x_j}{r} d\Omega \quad (8.21)$$

Or, in a more compact manner:

$$\langle \text{grad } u(x) \rangle = - \int_{\Omega} \frac{1}{h} W' \frac{u(x') \otimes (x' - x)}{r} d\Omega \quad (8.22)$$

○ *Divergence of a vector valued function:*

In a similar manner, the divergence of a vector valued function, $u_i(x)$, is:

$$\begin{aligned} \langle \text{div } u(x) \rangle &= - \int_{\Omega} u(x') \text{grad } W d\Omega \\ \langle \text{div } u(x) \rangle &= - \int_{\Omega} \frac{1}{h} W' \frac{u(x') \cdot (x' - x)}{r} d\Omega \end{aligned} \quad (8.23)$$

○ *Divergence of a tensor valued function:*

The divergence of a tensor valued function, $\sigma(x)$, is approximated as:

$$\begin{aligned} \langle \text{div } \sigma(x) \rangle &= - \int_{\Omega} \sigma \cdot \text{grad } W d\Omega \\ \langle \text{div } \sigma(x) \rangle &= - \int_{\Omega} \frac{1}{h} W' \frac{\sigma \cdot (x' - x)}{r} d\Omega \end{aligned} \quad (8.24)$$

• **Properties of the integral approximations**

Some properties of the integral approximation are fundamental to get the integral approximation of the balance equation (mass, linear momentum...)

(P1)
$$\langle \alpha \phi \rangle = \alpha \langle \phi \rangle \quad \alpha \in \mathbb{R} \quad (8.25)$$

(P2)
$$\langle \phi + \psi \rangle = \langle \phi \rangle + \langle \psi \rangle \quad (8.26)$$

(P3)
$$\langle \phi \psi \rangle = \langle \phi \rangle \cdot \langle \psi \rangle \quad (8.27)$$

(P4)
$$\left\langle \frac{d\phi(x,t)}{dt} \right\rangle = \frac{d}{dt} \langle \phi \rangle \quad (8.28)$$

It is important to note that the properties (2.128) and (2.129) are true in the limit $h \rightarrow 0$ or $k \rightarrow \infty$.

- **Integral approximation of the balance of mass and linear momentum equation**

The equations of balance of mass and linear momentum can be discretized using the properties of integral approximations from (8.27) to (8.28).

- *The Lagrangian form of the mass balance equation is:*

$$\frac{D\rho}{Dt} + \rho \operatorname{div} v = 0 \quad (8.29)$$

From (8.29), the integral form is obtained:

$$\left\langle \frac{D\rho}{Dt} + \rho \operatorname{div} v \right\rangle = 0 \quad (8.30)$$

Namely,

$$\int_{\Omega} W \left(\frac{D\rho}{Dt} + \rho \operatorname{div} v \right) = 0 \quad (8.31)$$

Therefore, using the properties of integral approximations, the integral approximation of the equation of mass balance is:

$$\frac{D}{Dt} \langle \rho \rangle + \langle \rho \rangle \langle \operatorname{div} v \rangle = 0 \quad (8.32)$$

- *The equation of balance of linear momentum is given by:*

$$\rho \frac{Dv}{Dt} = \rho b + \operatorname{div} \sigma \quad (8.33)$$

In the fluid mechanics, the stress tensor can be decomposed in a hydrostatic and in a deviatoric component:

$$\sigma = -pI + s \quad (8.34)$$

Where:

$$p = -\frac{1}{3} \operatorname{tr}(\sigma) \quad (8.35)$$

Therefore the equation of balance can be written as:

$$\rho \frac{Dv}{Dt} = \rho b + \operatorname{div} s - \operatorname{grad} p \quad (8.36)$$

And the integral approximation of this equation is:

$$\langle \rho \rangle \frac{D}{Dt} \langle v \rangle = -\langle \operatorname{grad} p \rangle + \langle \operatorname{div} s \rangle + \langle \rho \rangle \cdot \langle b \rangle \quad (8.37)$$

Appendix 9. Details on the SPH discretization of integral approximation of functions and derivatives

All operations are to be referred to nodes. A set of particles or nodes $\{x_k\}$ with $K=1\dots N$ will be introduced.

As it has already been mentioned, the integral approximation or continuum approximation of a function is given by:

$$\langle \phi(x) \rangle = \int_{\Omega} \phi(x') W(x'-x, h) dx' \quad (9.1)$$

As the information concerning the function is only available at a set of nodes, the integral could be evaluated using a numerical integration formula:

$$\langle \phi(x_i) \rangle_h = \sum_{J=1}^N \phi(x_J) W(x_J - x_i, h) \omega_J \quad (9.2)$$

Where the sub index h is used to denote the discrete approximation and ω_J the weights of the integration formula.

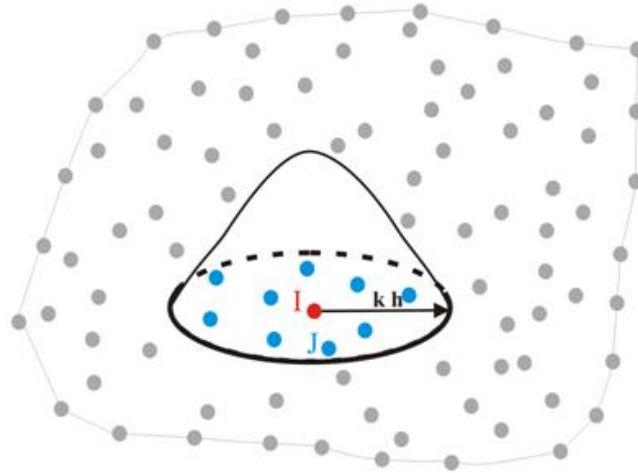
In order to simplify, the notation, ϕ_i , is introduced and defined as:

$$\phi_i = \langle \phi(x_i) \rangle_h = \sum_{J=1}^N \phi(x_J) W(x_J - x_i, h) \omega_J \quad (9.3)$$

As the kernel function has a local support, i.e., it is zero when $|x_J - x_i| > 2h$, the summation extends only to the set of Nh points, which fulfill this condition:

$$\phi_i = \langle \phi(x_i) \rangle_h = \sum_{J=1}^{Nh} \phi(x_J) W(x_J - x_i, h) \omega_J \quad (9.4)$$

The next figure illustrates the numerical integration procedure performed:



Nodes and numerical integration in a SPH mesh

In above, it is worth noticing that $\phi(x_j)$ is not ϕ_j . The value of the kernel $W(x_j - x_I, h)$ is often denoted as W_{IJ} . It is important to remember that it is the value of the kernel centered at node I at position J . The kernels used in SPH are symmetric (c.f. properties), as they depend on $\xi = \frac{|x' - x|}{h}$.

Therefore the following result is obtained:

$$W_{IJ} = W(x_j - x_I, h) = W(x_I - x_j, h) = W_{JI} \quad (9.5)$$

And

$$\phi_I = \sum_{J=1}^{N_h} \phi(x_j) W_{IJ} \omega_J \quad (9.6)$$

Moreover, the kernel can be written as $W_{IJ} = W(\xi_{IJ})$, where

$$\xi_{IJ} = \frac{|x_I - x_J|}{h} \quad (9.7)$$

It can be observed that h is not included explicitly when it used the more compact notation W_{IJ} . In the case where h depends on the node, W_{IJ} corresponds to the value at the node I , as its origin is an approximation to the Dirac distribution centered on x_I . In this case, the discrete kernel loses its symmetry. One possible solution, commonly used by SPH community is to define, for every couple of nodes I and J an averaged h :

$$\xi_{IJ} = \frac{|x_I - x_J|}{h_{IJ}} \quad \text{where } h_{IJ} = \frac{1}{2}(h_I + h_J) \quad (9.8)$$

Next, for the sake of simplicity, the sub indexes of h will be dropped.

The situation here is different than that found in finite elements, where Gaussian integration rules are commonly used. There, the position and the weights of the integration points are determined in order to obtain the maximum degree of precision. For instance, a Gauss integration rule in one dimension with n integration points has a degree of precision $m = 2n - 1$ if the position and weights of all points are free. If the positions are fixed for all the points (for instance, when the integration points have to be equally spaced), the degree of precision is $n - 1$.

In SPH, the nodes surrounding the node, where the integral has to be evaluated, can have any position, and, therefore, there will not be any general integration rule embracing all infinite possible cases.

If the approximation of a constant by the integration rule (9.2) is considered, the following equation can be obtained:

$$\langle 1 \rangle_h = \sum_{J=1}^{N_h} 1 \cdot W_{IJ} \omega_J \quad (9.9)$$

If this result is compared to the unity condition of W , the weight corresponding to the particle J has to be the volume, area or length Ω_J associated to it. Therefore the approximation is written as:

$$\phi_I = \sum_{J=1}^{N_h} \phi(x_j) W_{IJ} \Omega_J \quad (9.10)$$

In the framework of continuum mechanics (solid and fluids); it is convenient to introduce the density ρ_J associate to the node J as:

$$\rho_J = m_J / \Omega_J \quad (9.11)$$

Where m_J is the mass associated to the node J .

Thus the equation (9.8) is written, in a common form of SPH, as:

$$\phi_I = \sum_{J=1}^{N_h} \phi(x_J) W_{IJ} \frac{m_J}{\rho_J} \quad (9.12)$$

In the case that the function ϕ represents the density, the last equation is written as:

$$\begin{aligned} \rho_I &= \sum_{J=1}^{N_h} \rho_J W_{IJ} \frac{m_J}{\rho_J} \\ \rho_I &= \sum_{J=1}^n W_{IJ} m_J \end{aligned} \quad (9.13)$$

- **Discrete approximation of derivatives and differential operators**

The discretized forms of SPH integral approximations come from the expressions got in the appendix 8.

Here after, the following notation will be used:

$$\begin{aligned} x_{IJ} &= x_I - x_J \\ r_{IJ} &= |x_I - x_J| \\ W_{IJ} &= \frac{W'}{h} \frac{x_{IJ}}{r_{IJ}} \end{aligned} \quad (9.14)$$

And

$$\begin{aligned} \text{grad } \phi_I &= \langle \text{grad } \phi(x_I) \rangle_h \\ \text{div } u_I &= \langle \text{div } u(x_I) \rangle_h \\ \text{grad } v_I &= \langle \text{grad } v(x_I) \rangle_h \\ \text{div } \sigma_I &= \langle \text{div } \sigma(x_I) \rangle_h \end{aligned} \quad (9.15)$$

The discretized forms are:

- *Gradient of a scalar function:*

$$\begin{aligned} \text{grad } \phi_I &= \sum_{J=1}^{N_h} \phi(x_J) \nabla W_{IJ} \Omega_J \\ \text{or} \\ \text{grad } \phi_I &= \sum_{J=1}^{N_h} \frac{m_J}{\rho_J} \phi(x_J) \nabla W_{IJ} \end{aligned} \quad (9.16)$$

In the practice, the approximation $\phi_J \approx \phi(x_J)$ is often used, which results on:

$$\text{grad } \phi_I = \sum_{J=1}^{N_h} \frac{m_J}{\rho_J} \phi_J \nabla W_{IJ} \quad (9.17)$$

In addition to (2.155), there are some alternatives which are preferred by SPH practitioners as they present some symmetries which improve the accuracy of computations. These alternatives are called “symmetrized forms” and are for the equation (2.155):

$$\text{grad } \phi_I = \frac{1}{\rho_I} \sum_J m_J (\phi_J - \phi_I) \text{grad } W_{IJ} \quad (9.18)$$

$$\text{grad } \phi_I = \rho_I \sum_J m_J \left\{ \frac{\phi_J}{\rho_J^2} + \frac{\phi_I}{\rho_I^2} \right\} \text{grad } W_{IJ} \quad (9.19)$$

$$\text{grad } \phi_I = \sum_{J=1}^{N_h} \frac{m_J}{\rho_J} (\phi_I + \phi_J) \text{grad } W_{IJ} \quad (9.20)$$

Sometimes the variant of the third symmetrized form (2.158) is used:

$$\text{grad } \phi_I = \sum_{J=1}^{N_h} \frac{m_J}{\rho_J} (\phi_I + \phi_J) \text{grad } W_{IJ} \quad (9.21)$$

○ *Gradient of a vector function:*

The discretized form in SPH is:

$$\text{grad } v_I = \sum_{J=1}^{N_h} \frac{m_J}{\rho_J} v_J \otimes \text{grad } W_{IJ} \quad (9.22)$$

And the symmetrized forms are:

$$\text{grad } v_I = \frac{1}{\rho_I} \sum_J m_J (v_J - v_I) \otimes \text{grad } W_{IJ} \quad (9.23)$$

$$\text{grad } v_I = \rho_I \sum_J m_J \left\{ \frac{v_J}{\rho_J^2} + \frac{v_I}{\rho_I^2} \right\} \otimes \text{grad } W_{IJ} \quad (9.24)$$

$$\text{grad } v_I = \rho_I \sum_J m_J \left\{ \frac{v_J}{\rho_J^2} + \frac{v_I}{\rho_I^2} \right\} \otimes \text{grad } W_{IJ} \quad (9.25)$$

○ *Divergence of vector valued function:*

The discretized form of a vector valued function is:

$$\text{div } v_I = \sum_J \frac{m_J}{\rho_J} u_J \cdot \text{grad } W_{IJ} \quad (9.26)$$

And the symmetrized forms are:

$$\text{div } v_I = -\frac{1}{\rho_I} \sum_J v_{IJ} \text{grad } W_{IJ} m_J \quad (9.27)$$

Where the following notation has been introduced:

$$v_{IJ} = v_I - v_J \quad (9.28)$$

$$\text{div } v_I = \rho_I \sum_J m_J \left(\frac{v_J}{\rho_J^2} + \frac{v_I}{\rho_I^2} \right) \cdot \text{grad } W_{IJ} \quad (9.29)$$

$$\text{div } v_I = -\sum_J \frac{m_J}{\rho_J} v_{IJ} \cdot \text{grad } W_{IJ} \quad (9.30)$$

○ *Divergence of a tensor valued function:*

The discretized form in SPH of the divergence of a tensor valued function is:

$$\text{div } \sigma_I = -\sum_J \frac{m_J}{\rho_J} \sigma_J \cdot \text{grad } W_{IJ} \quad (9.31)$$

And the symmetrized forms are:

$$\text{div } \sigma_I = -\sum_J \sigma_{IJ} \text{grad } W_{IJ} m_J \quad (9.32)$$

$$\text{div } \sigma_I = -\rho_I \sum_J m_J \left(\frac{\sigma_J}{\rho_J^2} + \frac{\sigma_I}{\rho_I^2} \right) \cdot \text{grad } W_{IJ} \quad (9.33)$$

$$\text{div } \sigma_I = -\sum_J \frac{m_J}{\rho_J} \sigma_{IJ} \cdot \text{grad } W_{IJ} \quad (9.34)$$

And its variant form:

$$\operatorname{div} \sigma_I = - \sum_J \frac{m_J}{\rho_J} (\sigma_I + \sigma_J) \cdot \operatorname{grad} W_{IJ} \quad (9.35)$$

- **Some properties of SPH approximations**

Next some properties of SPH approximations are presented. They come from the properties of integral approximations. These approximations are important to get the discretized approximations of SPH.

The discretized version of the properties (8.25) to (8.28) is given by:

(P1)
$$\langle \alpha \phi \rangle = \alpha \langle \phi \rangle \quad \alpha \in \mathbb{R} \quad (9.36)$$

(P2)
$$\langle \phi + \psi \rangle = \langle \phi \rangle + \langle \psi \rangle \quad (9.37)$$

(P3)
$$\langle \phi \psi \rangle = \langle \phi \rangle \cdot \langle \psi \rangle \quad (9.38)$$

(P4)
$$\left\langle \frac{d\phi(x,t)}{dt} \right\rangle_h = \frac{d}{dt} \langle \phi \rangle_h \quad (9.39)$$

It is important to note that the properties (9.38) and (9.39) are true in the limit $h \rightarrow 0$ or $k \rightarrow \infty$.

- **Discretization of the balance equation (mass and linear momentum)**

- *Mass balance:*

After (8.31), the integral approximation of the mass balance equation is:

$$\frac{D}{Dt} \langle \rho \rangle + \langle \rho \rangle \langle \operatorname{div} v \rangle = 0 \quad (9.40)$$

As there are various alternatives to discretize $\langle \operatorname{div} v \rangle$, the following discretized forms of the mass balance equation can be obtained:

➤ Basic forms:

$$\frac{D\rho_I}{Dt} = -\rho_I \sum_J \frac{m_J}{\rho_J} v_J \operatorname{grad} W_{IJ} \quad (9.41)$$

➤ First symmetrized form:

$$\frac{D\rho_I}{Dt} = \sum_J m_J v_{IJ} \operatorname{grad} W_{IJ} \quad (9.42)$$

➤ Second symmetrized form:

$$\frac{D\rho_I}{Dt} = -\rho_I^2 \sum_J m_J \left(\frac{v_I}{\rho_I^2} + \frac{v_J}{\rho_J^2} \right) \operatorname{grad} W_{IJ} \quad (9.43)$$

➤ Third symmetrized form:

$$\frac{D\rho_I}{Dt} = \rho_I \sum_J \frac{m_J}{\rho_J} v_{IJ} \operatorname{grad} W_{IJ} \quad (9.44)$$

○ *Linear momentum balance:*

After (8.37), the integral approximation of the linear momentum balance equation is:

$$\langle \rho \rangle \frac{D}{Dt} \langle v \rangle = -\langle \text{grad } p \rangle + \langle \text{div } s \rangle + \langle \rho \rangle \cdot \langle b \rangle \quad (9.45)$$

As there are various alternatives to discretize, the gradient and divergence operators, the following discretized forms of the linear moment balance equation can be obtained:

➤ Basic forms:

$$\rho_i \frac{Dv_i}{Dt} = -\sum_J \frac{m_J}{\rho_J} p_J \text{grad } W_{IJ} + \sum_J \frac{m_J}{\rho_J} s_J \text{grad } W_{IJ} + b_i \quad (9.46)$$

➤ First symmetrized form:

$$\frac{Dv_i}{Dt} = -\frac{1}{\rho_i} \sum_J m_J (p_J - p_i) \text{grad } W_{IJ} + \frac{1}{\rho_i} \sum_J m_J (s_J - s_i) \text{grad } W_{IJ} + b_i \quad (9.47)$$

➤ Second symmetrized form:

$$\frac{Dv_i}{Dt} = -\sum_J m_J \left(\frac{p_i}{\rho_i^2} + \frac{p_J}{\rho_J^2} \right) \text{grad } W_{IJ} + \sum_J m_J \left(\frac{s_i}{\rho_i^2} + \frac{s_J}{\rho_J^2} \right) \text{grad } W_{IJ} + b_i \quad (9.48)$$

➤ Third symmetrized form:

$$\frac{Dv_i}{Dt} = -\sum_J m_J \left(\frac{p_i + p_J}{\rho_i \rho_J} \right) \text{grad } W_{IJ} + \sum_J m_J \left(\frac{s_i + s_J}{\rho_i \rho_J} \right) \text{grad } W_{IJ} + b_i \quad (9.49)$$

● **SPH discretization of the 2D depth integrated equation**

○ *Equations to discretize:*

The purpose of this section is to present the SPH discretization procedure of the depth integrated model which takes into account pore pressure dissipation during the propagation phase. The depth integrated equations expressed in eulerian form are:

– Balance of mass:

$$\frac{\partial h}{\partial t} + \frac{\partial}{\partial x_j} (h \bar{v}_j) = e_r \quad \text{con } j=1,2 \quad (9.50)$$

– Balance of linear momentum:

$$\frac{\partial}{\partial t} (h \bar{v}_i) + (1 + \alpha) \frac{\partial}{\partial x_j} (h \bar{v}_i \bar{v}_j) = -e_r \bar{v}_i + b_i h + \frac{\partial}{\partial x_j} (h \bar{\sigma}_{ij}) + |N^A| t_i^A + |N^B| t_i^B \quad (9.51)$$

The following decomposition can be introduced:

$$\sigma_{ij} = -\bar{p} \delta_{ij} + \sigma_{ij}^* \quad (9.52)$$

With:

$$\bar{p} = \frac{1}{2} \rho b_3 h \quad \bar{\sigma}_{ij}^* = \bar{\sigma}_{ij} + \bar{p} \delta_{ij} \quad (9.53)$$

The equation (9.51) can be written as:

$$\begin{aligned} \frac{\partial}{\partial t}(h\bar{v}_i) + \frac{\partial}{\partial x_j} \left(h\bar{v}_i\bar{v}_j - \frac{1}{2}\rho b_3 h^2 \delta_{ij} \right) &= -e_r \bar{v}_i + \\ \alpha \frac{\partial}{\partial x_j} (h\bar{v}_i\bar{v}_j) + \frac{\partial}{\partial x_j} (h\bar{\sigma}_{ij}^*) + b_i h + |N^A| t_i^A + |N^B| t_i^B \end{aligned} \quad (9.54)$$

– The vertical consolidation is given by:

$$\frac{\partial}{\partial t}(P_1 h) + \frac{\partial}{\partial x_j} (\bar{v}_j P_1 h) + \frac{\pi}{2} C.T. = -\frac{\pi^2}{4h} c_v P_1 \quad (9.55)$$

The quasi Lagrangian forms of the depth integrated model come from:

– Balance of mass:

$$\frac{d\bar{h}}{dt} + h \frac{\partial \bar{v}_j}{\partial x_j} = e_R \quad (9.56)$$

– Balance of linear momentum:

$$h \frac{d\bar{v}_i}{dt} - \frac{\partial}{\partial x_i} \left(\frac{1}{2} \rho b_3 h^2 \right) = -e_R \bar{v}_i - \alpha \frac{\partial}{\partial x_j} (h\bar{v}_i\bar{v}_j) + \frac{\partial}{\partial x_j} (h\bar{\sigma}_{ij}^*) + b_i h + |N^A| t_i^A + |N^B| t_i^B \quad (9.57)$$

– Vertical consolidation:

$$\frac{d\bar{P}_1}{dt} + \frac{1}{h} P_1 e_R + \frac{\pi}{2h} C.T. = \frac{\pi^2}{4h^2} c_v P_1 \quad (9.58)$$

It is possible to use either the Eulerian or the quasi Lagrangian approximations with SPH model, but the Lagrangian forms presents clear advantages over the Eulerian.

○ SPH discretization

A set of nodes $\{x_K\}$ with $K=1\dots N$ and the nodal variables:

- h_I the height of the flow at the node I
- \bar{v}_I the depth averaged 2D velocity
- t_I^b the surface force vector at the bottom
- $\bar{\sigma}_I^*$ the depth averaged modified stress tensor
- P_I the pore pressure at the basal surface

If the 2D area associated to node I is Ω_I , the following magnitude are introduced:

- A fiction mass, m_I , moving with this node:

$$m_I = \Omega_I h_I \quad (9.59)$$

- \bar{p}_I , an averaged pressure term given by:

$$\bar{p}_I = \frac{1}{2} \rho b_3 h_I^2 \quad (9.60)$$

It is important to note that m_I has not played a physical meaning, as when node I moves, the material contained in the column of base Ω_I , has entered it or will leave it as the column moves with an averaged velocity which is not the same for all particles in it.

The SPH approximation of the balance of mass equation (2.197) is built from:

$$\left\langle \frac{d\bar{h}}{dt} + h \frac{\partial \bar{v}_j}{\partial x_j} \right\rangle = e_r \quad (9.61)$$

From which:

$$\frac{\bar{d}}{dt} \langle h \rangle + \langle h \rangle \left\langle \frac{\partial \bar{v}_j}{\partial x_j} \right\rangle = e_r \quad j=1,2 \quad (9.62)$$

The equation is written as node I as:

$$\frac{\bar{d}}{dt} h_I + h_I \left\langle \frac{\partial \bar{v}_j}{\partial x_j} \right\rangle_I = e_r \quad j=1,2 \quad (9.63)$$

Where the divergence term is given by:

$$\text{div } v_I = - \sum_J \Omega_J v_J \text{ grad } W_{IJ} \quad (9.64)$$

or

$$\text{div } v_I = - \sum_J \frac{m_J}{h_J} v_J \text{ grad } W_{IJ} \quad (9.65)$$

Of course, any alternatives symmetrized form can be used. Thus the discretized balance of mass equation is written as:

$$\frac{\bar{d}h_I}{dt} = -h_I \sum_J \frac{m_J}{h_J} v_J \text{ grad } W_{IJ} \quad (\text{Basic form})$$

$$\frac{\bar{d}h_I}{dt} = \sum_J m_J v_{IJ} \text{ grad } W_{IJ} \quad (\text{First form}) \quad (9.66)$$

$$\frac{\bar{d}h_I}{dt} = h_I \sum_J \frac{m_J}{h_J} v_{IJ} \text{ grad } W_{IJ} \quad (\text{Second form})$$

Where v_{IJ} has been introduced:

$$v_{IJ} = v_I - v_J \quad (9.67)$$

Alternatively, the height can be obtained once the position of the nodes is known as:

$$\begin{aligned} h_I &= \langle h(x_I) \rangle \\ &= \sum_J h_J \Omega_J W_{IJ} \\ &= \sum_J m_J W_{IJ} \end{aligned} \quad (9.68)$$

The height can be normalized, which allows the approximation close to the boundary nodes:

$$h_I = \frac{\sum_J m_J W_{IJ}}{\sum_J \left(\frac{m_J}{h_J} \right) W_{IJ}} \quad (9.69)$$

Next the simplified form of the balance of linear momentum equation (9.57) is discretized:

$$h \frac{\bar{d}}{dt} \bar{v} = -e_R \bar{v} + \text{grad} \left(\frac{1}{2} \rho b_3 h^2 \right) + \text{div} (h \bar{\sigma}_{ij}^*) + bh + |N^B| t^B \quad (9.70)$$

Or introducing the averaged pressure defined above:

$$h \frac{\bar{d}}{dt} \bar{v} = -e_R \bar{v} + \text{grad } p + \text{div} (h \bar{\sigma}_{ij}^*) + bh + |N^B| t^B \quad (9.71)$$

Where the terms corresponding to surface forces at the surface of the flow, erosion and the correction factor α have been neglected.

The left hand side results on:

$$h_i \frac{\bar{d}}{dt} \bar{v}_i \quad (9.72)$$

Depending on the symmetrized form chosen to discretize the gradient of pressure and the divergence of stress tensor, the following discretized forms of balance of momentum equation is obtained:

$$\frac{\bar{d}}{dt} \bar{v}_i = - \sum_J m_J \frac{p_i + p_J}{h_i h_J} \text{grad} W_{ij} + \sum_J m_J \frac{\sigma_i + \sigma_J}{h_i h_J} \text{grad} W_{ij} + b + \frac{1}{h_i} |N^B| t_i^B \quad (9.73)$$

$$\frac{\bar{d}}{dt} \bar{v}_i = - \sum_J m_J \left(\frac{p_i}{h_i^2} + \frac{p_J}{h_J^2} \right) \text{grad} W_{ij} + \sum_J m_J \left(\frac{\sigma_i}{h_i^2} + \frac{\sigma_J}{h_J^2} \right) \text{grad} W_{ij} + b + \frac{1}{h_i} |N^B| t_i^B \quad (9.74)$$

Finally the SPH discretized form of the basal pore pressure dissipation is:

$$\frac{\bar{d}}{dt} P_{1i} = - \frac{\pi^2 c_v}{4h_i} P_{1i} \quad (9.75)$$

Appendix 10. Description of the Runge Kutta 4th (RK4)

The Runge Kutta 4th (RK4) method is used by the SPH depth integrated model to solve the ordinary differential equation. This section describes this method.

So be it the differential equation of first order:

$$\frac{\partial y}{\partial x} = f(x, y) \quad (10.1)$$

The RK4 method uses some intermediates point to carry out the value of y_{i+1} from y_i .

Considering the intermediate point A with x-coordinate $x_i + \frac{h}{2}$ and with the following y-coordinate:

$$y_{iA} = y_i + \left(\frac{dy}{dx}\right)_i \times \frac{h}{2} \quad (10.2)$$

Thus

$$y_{iA} - y_i = + \left(\frac{dy}{dx}\right)_i \times \frac{h}{2} = k_1 \quad (10.3)$$

Next a point B with the following y-coordinate is considered:

$$y_{iB} = y_i + \left(\frac{dy}{dx}\right)_{iA} \times \frac{h}{2} \quad (10.4)$$

Thus

$$y_{iB} - y_i = + \left(\frac{dy}{dx}\right)_{iA} \times \frac{h}{2} = \frac{k_2}{2} \quad (10.5)$$

Next a point C with the following y-coordinate is defined:

$$y_{iC} = y_i + \left(\frac{dy}{dx}\right)_{iB} \times h \quad (10.6)$$

Thus

$$y_{iC} - y_i = + \left(\frac{dy}{dx}\right)_{iB} \times h = k_3 \quad (10.7)$$

And finally introducing $\left(\frac{dy}{dx}\right)_{iC}$ the value of $\left(\frac{dy}{dx}\right)$ at C, the following equality is established:

$$\left(\frac{dy}{dx}\right)_{iC} \times h = k_4 \quad (10.8)$$

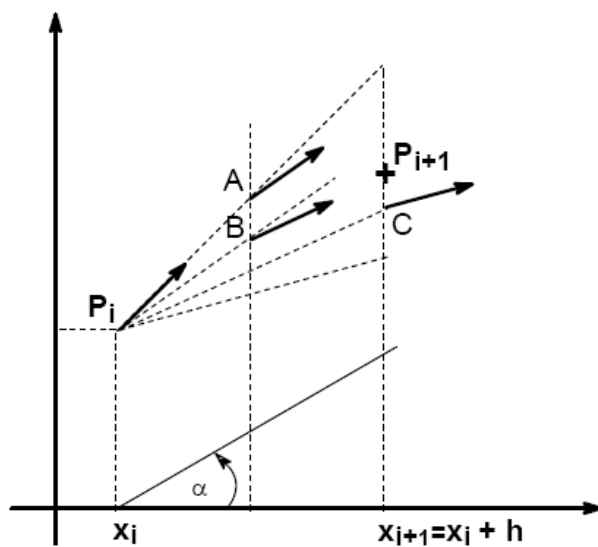
The RKA method gives the y-coordinate y_{i+1} from y_i using the following expression:

$$y_{i+1} = y_i + \frac{1}{6} \left[\left(\frac{dy}{dx}\right)_i + 2 \times \left(\frac{dy}{dx}\right)_{iA} + 2 \times \left(\frac{dy}{dx}\right)_{iB} + \left(\frac{dy}{dx}\right)_{iC} \right] \times h \quad (10.9)$$

Or

$$y_{i+1} = y_i + \frac{1}{6} [k_1 + 2 \times k_2 + 2 \times k_3 + k_4] \quad (10.10)$$

The following figure is a geometric representation of the RK4



Geometric representation of the RK4 method – SOURCE: M. Schwing – IUFM de Lorraine